Fall 2007

Generation and measurement of surface plasmon coupled emission

Kathleen E. Hamilton
University of New Hampshire, Durham

Generation and Measurement of Surface Plasmon Coupled Emission

BY

Kathleen E. Hamilton

B.S., Mary Washington College (2004)

THESIS

Submitted to the University of New Hampshire
in partial fulfillment of
the requirements for the degree of

Master of Science

in

Physics

September 2007

This thesis has been examined and approved.

James M. E. Harper

Thesis Director, James M. E. Harper, Professor of Physics

Thomas Laue, Professor of Biochemistry and Molecular Biology

Olof Echt, Professor of Physics

7/30/07

Date

ACKNOWLEDGMENTS

- Thanks to the current and former members of Jim Harper's group: Amanda Brown, Don Carlson, Derya Deniz, Dana Filoti for their help with film deposition, and Ann-Marie Shover for her early studies of materials for SPCE applications

- Thanks to the current and former members of Tom Laue's group: Brett Austin, Sue Chase, and Kari Hartman for their help in early design of the apparatus and fluorescent dye preparation

- Thanks to Rudolf Seitz of the Chemistry Department for access to the spin coater

- Thanks to Rob Cinq-Mars of the UNH Instrumentation Center for help in LabVIEW programming and stepper motor operation

- Thanks to Ignacy and Zygmunt Gryczynski of the University of North Texas for their guidance and advice in the early development of SPCE testing at the University of New Hampshire

- Thanks to the thesis committee members: Professors Tom Laue, Olof Echt and James Harper

- This thesis was financially supported in part by NIH Grant 1-R33CA14460-01

Table of Contents

List of Tables

List of Figures

ABSTRACT

GENERATION AND MEASUREMENT OF SURFACE PLASMON COUPLED EMISSION

by

Kathleen E. Hamilton
University of New Hampshire, September, 2007

Surface plasmon coupled emission (SPCE) is a process by which isotropic fluorescent emission, from a fluorescent dye or biological agent labeled with a fluorescent dye, is channeled into highly directional emission. This process relies on the interaction between fluorescent dye molecules and thin silver films in close proximity to each other. Recent studies have shown that SPCE greatly increases the sensitivity of spectroscopic methods by increasing the amount of light that can be collected from a fluorescent molecule. The work described in this thesis encompasses the study of new materials for SPCE sample manufacture as well as the design and construction of a compact, automated apparatus for SPCE measurement. Novel material sets have been explored to improve the adhesion of silver films to glass slides and to protect them against corrosion from the fluorescent dye coating. These sets are made with reactive gas sputtering of materials. Examples of the SPCE signals from these materials will be shown. The apparatus built to measure the angular distribution of SPCE signals measures 18"X12"X12". Measurements of SPCE with angular resolutions as low as 0.5° are demonstrated with accurate, repeatable scans. With a 1.0° step size, a full angular scan through 180° can be completed in less than 5 minutes.

CHAPTER 1

INTRODUCTION

Recent studies have shown that the ability of thin metal films to modify the fluorescent signal of a dye can create a powerful biodetection method. The work described in this thesis was carried out with the goal of developing and building a self-contained apparatus for a fluorescence detector which greatly streamlines and simplifies the generation and measurement of this modified fluorescent signal. The fluorescence signal measured is highly localized, created in conjunction with charge oscillations in a thin metal film. The resulting apparatus precisely measures this signal. There still exist areas of improvement regarding the reproducibility and consistency of scans. However, the apparatus does have the ability to generate and measure this signal. This first chapter will outline the scope of this thesis.

1.1 Background of the Study

Fluorescence is emitted from organic molecules called fluorophores. These molecules can selectively bind to other organic species, creating a detectable label. This labeling is used in spectroscopic methods to study the hybridization of DNA, live cells, and also to detect contaminants in solution. However, the isotropic nature of fluorescence emission limits the sensitivity of these methods, since only a small fraction of the light emitted may be collected. In the past decade, numerous papers have proposed a new method of fluorescence spectroscopy[1],[2]. These studies use thin metal films to enhance and alter the nature of

fluorescence emission. By placing fluorescent dyes in close proximity to metal films, the emission is channeled from isotropic to highly localized emission. The process of enhancing the fluorescent signal from a dye molecule through interactions with a thin metal film is known as "Surface Plasmon Coupled Emission" and will be referred to throughout this thesis as SPCE.

SPCE is closely related to another process called "Surface Plasmon Resonance" or SPR. SPR is angular dependent absorption by a thin metal film of incident light, whereas SPCE is the angular dependent emission of light by a thin metal film. SPR is well established as a means of sensitive detection of biological systems in close proximity to metal layers.

SPCE and SPR are dependent on the oscillations of electrons in metal films of a finite thickness. Depending on the metal used, the resulting SPCE emission can be in the UV[3], near-IR[4] or visible light range[1]. The use of silver as the metal film layer, used in this thesis, results in visible light emission. The films used in the above studies have relied on commercially deposited slides. The slides used were stacks of three separate film layers: a chromium under-layer, a 50 nm-thick silver film, and a glass over-layer (silicon dioxide). The chromium layer was necessary to adhere the silver film to the glass substrate. The glass over-layer was necessary to prevent silver film corrosion and also act as a spacer between the dye molecules and silver film. A collaboration between the Gryczynski research group and the Harper research group allowed for exploration of new material sets. Films were deposited in New Hampshire and sent to the Gryczynski group (formerly at the University of Maryland, currently at the University of North Texas). SPR and SPCE are sensitive to changes at the metal surfaces. This is useful in highly sensitive detection methods. However, it also means that slight changes in film surface quality (silver is prone to forming oxides on its surfaces) can dramatically affect signal quality. This motivated the development of an

SPCE measurement system that could be employed at the University of New Hampshire.

As mentioned above, the samples studied by the Gryczynskis relied on commercially deposited slides made with chromium, silver and glass. The three layer system (adhesion, silver and protection layer) was used to design film stacks at the University of New Hampshire. The configuration needed to deposit three distinct film layers was not available. Reactive sputtering techniques led to the development of film stacks using oxides and nitrides as the protection layers. These three layers will be referred to throughout this thesis as the adhesion layer, the SPCE layer and the passivation layer, respectively.

SPCE theory has been developed from studies of a radiating dipole near thin metal films and from studies of surface oscillations in thin metal films. The measurement of SPCE requires the detection of a light signal transmitted through the silver film and emitted into a hemi-cylindrical prism. It is measured by precise positioning of a photomultiplier, rotated around the prism.

1.2 Statement of the Problem

The measurement and generation of SPCE was detailed in a 2004 study[1]. It showed that SPCE emission is located at specific angles, spans a small range of values, and is highly polarized. Two methods of generation were described. These are called the Kretschmann and Reverse Kretschmann (RK) configurations (shown in Figure 1.1).

To detect SPCE, the Kretschmann configuration requires the precise angular positioning of the excitation and the detector. In contrast, the RK configuration requires the precise angular positioning of only the detector and the excitation is fixed at normal incidence. The RK configuration results in the same emission spectra as the Kretschmann configuration, but greatly simplifies the experimental design and reduces systematic error. The apparatus

in this thesis was built using the RK configuration.

The design of the apparatus addressed four central problems: the conditions for operating the detector, the alignment of the laser and prism, the alignment of the prism and detector, and the accurate positioning of the detector. Additionally, the interaction between design elements posed new challenges. For example, the rotation of the detector limited the possible positions of laser and sample. The results which will be presented in Chapter 5 will illustrate the success of the apparatus design.

The detection of the fluorescence signal is made using a photomultiplier tube (Hamamatsu 6779-04). The use of this light-sensitive detector necessitated a light tight environment. The research carried out by the group at the University of Maryland was conducted in a blacked out laboratory. However, replication of this environment was not feasible at the University of New Hampshire. A blackout environment was created by constructing a box out of light-tight materials. This enclosed the entire apparatus and prevented ambient light from interfering with SPCE measurements.

Alignments posed the largest obstacles to proper apparatus function. The laser-prism

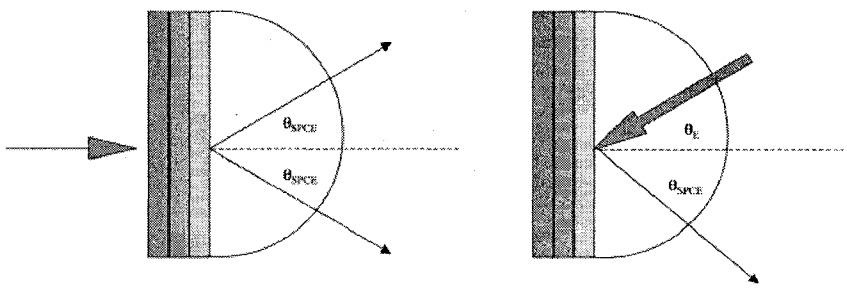

Figure 1-1: Configurations for exciting SPCE. The Kretschmann (right) and the Reverse Kretschmann (left) configurations both result in identical spectra. Fluorescence from a thin dye layer (pink) interacts with a metal film (grey) and emits light in an angular distribution

alignment was straightforward: using the RK configuration required the laser to be aligned such that its light is normally incident on the sample. The consistent angle of incidence, regardless of the materials used, meant that a fixed-angle laser arm could be employed. The solution of the alignment of the prism and the detector was slightly more involved. To record the fluorescence emitted by a sample, a detector is rotated through a semicircular arc around the prism. Extraneous excitation light was blocked from reaching the detector by a wavelength filter. However, this was most effective only if the filter was normal to the light. Therefore, to collect the fluorescence and not the excitation light, the filter needed to be aligned normal to the emitted light. The alignment of the filter and prism is shown in Figure 1.2. The normality condition on the filter and prism require that the detector sweeps out a semicircular arc, centered at the origin of the prism. The accurate load positioning necessitates the use of a precise rotary step. When the apparatus records a signal, it sweeps out an angle of 180°. Before a scan can begin, the motor must define a home position (0°). The motor must retract through an angle larger than 180°. The position of the laser arm had to be angled such that collisions between the retracting detector and the arm would be avoided.

1.3 Significance of the Study

The development of an automated measurement system for SPCE-based testing of films opens new avenues for research at the University of New Hampshire. The accessibility of fluorescent measurements and immediate feedback will lead to new research in biochemistry and material science studies. SPCE promises to offer an improved biodetection method, providing the possibility of highly sensitive detection of contaminants. Slides can be tested within hours of deposition, allowing for investigation into how the degradation of films

affects a SPCE signal.

1.4 Overview of the Methodology

The methods used in this thesis were concentrated into three sections: film deposition, fluorescent dye preparation and coating, and SPCE measurement. Samples used in the SPCE testing were stacks of three thin films, deposited using magnetron sputtering. The stacks consisted of an adhesion layer, a 50 nm thick silver film and a passivation layer. The material used for the passivation layer was deposited using reactive gas sputtering of the adhesion layer material. The fluorescent dye layer was a highly concentrated dye (Rhodamine Red) in a dilute polymer solution (Polyvinyl alcohol in an aqueous solution). A thin layer was deposited on the film stacks by spin coating. Explicit details of the SPCE testing are given in Chapter 4.

Materials sets were chosen for adhesion and protection of the silver film. Three adhe-

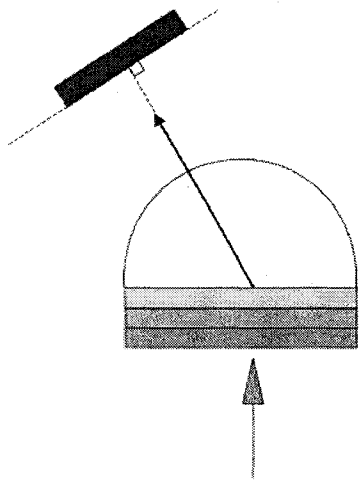

Figure 1-2: The alignment of the filter (blue) and prism (white). In order for the filter to effectively block extraneous light from the detector, it must be aligned normal to the direction of the light.

sion/passivation materials were used: Aluminum Silicon and nitrided Aluminum Silicon, Silicon and nitrided Silicon, Silicon and oxidized Silicon. During sputter deposition, the energetic atoms ejected from targets will deform the substrate surface as they collide. The bombardment of the substrate will eject atoms from the surface and create a site for reactions between incident target material and the substrate. Materials containing silicon were chosen with the assumption that they would react with the glass substrate. These materials were chosen because of their ability to form stable, and amorphous, nitrides and oxides at room temperature. Additionally, the Aluminum Silicon and nitrided Aluminum Silicon material set was used in prior SPCE testing by the Gryczynskis and at the University of New Hampshire and had demonstrated ability to generate a strong SPCE signal.

The dye layer was deposited outside of a vacuum environment. The film stacks were coated with a fluorescent dye. The dye was prepared in small (5 mL) batches from a concentrated stock solution. It was applied by spin coating, which creates a uniform layer with a thickness dependent on the spin speed. The dye Rhodamine Red was chosen for the coating because of its excitation and emission spectra. Rhodamine Red dye has an excitation peak near 532 nm, the wavelength of light used for excitation. Also, the dye has an emission peak with wavelength above 600 nm. The large difference in the excitation and emission wavelengths aided in the detection of SPCE.

To explore the ability of the detector to measure SPCE, several kinds of measurements were made of the samples. The collection time was varied and it was found that 0.75 seconds provided sufficient time to measure the fluorescence signal yet was short enough such that scans did not take an excessive amount of time. The voltage to the detector was also varied depending on the film stack used. The silicon/silver/silicon-oxide films emitted a strong SPCE signal and a voltage of less than 0.75 V was needed. The aluminum

silicon/silver/aluminum silicon-nitride films emitted a slightly weaker signal, voltages up to 0.85 V were needed. The higher voltages did not always produce better readings. It is seen that high voltages also lead to a large amount of noise. The angular resolution was tested by making scans with increasingly finer step sizes. In order to detect any angular drift, scans made in succession were fitted and the location of peaks compared. Greater detail about the methods used in this study is given in Chapter 4.

1.5 Thesis Summary

- Chapter 1, *Introduction*, motivates the need for SPCE measurements at the University of New Hampshire. The problems of designing and construction of an automated apparatus are outlined and discussed.

- Chapter 2, *Review of the Literature*, details SPCE theory from a historical perspective: detailing the theoretical work in of surface plasmons, to fluorescing molecule and conducting metal interactions to Surface Plasmon Resonance. The experimental works of Drexhage (fluorescent molecules interacting with metal films), and Gryczynski (SPCE) are also discussed.

- Chapter 3, *Theory*, presents an introduction to the process of fluorescence and the mathematical background for SPCE. This background is developed from the semi-classical work of Sommerfeld, Kuhn, Morawitz and the work of Chance, Prock and Sibley. Dispersion relations for surface plasmons on the metal/dye interface and the metal/glass interface are derived.

- Chapter 4, *Methods*, details the deposition of film stacks for SPCE samples, the preparation of samples for SPCE testing, the construction and design of the apparatus, and

also the computer programs that control it.

- Chapter 5, *Results*, presents the measurements of thin film stacks made by the apparatus built in this thesis work.

- Chapter 6, *Discussion*, is a short description of the results presented in this thesis. The results of this work will be emphasized and new directions for research will be presented.

Chapter 2

Review of the Literature

2.1 Introduction

There have been numerous theoretical and experimental studies of the interactions between fluorescent molecules and conducting surfaces in the past century. The literature reviewed in this thesis is concentrated in four areas: the study of interactions between fluorescent molecules and metal layers, the study of surface plasmons, the physics behind surface plasmon resonance (SPR) and the physics behind surface plasmon coupled emission (SPCE). The first area will show how molecules radiating above a conducting surface will generate surface waves (plasmons). The second will show how these surface waves create directional emission. The third and fourth sections build upon the previous two and describe how light can be transmitted through thin films and ultimately used to create directional fluorescence emission.

2.2 Radiating Sources Near Conducting Surfaces

The interactions between radiating systems and conducting surfaces has been studied using semi-classical and quantum mechanical methods. When posed as a semi-classical electrodynamics problem, the interactions are described by solving the differential Maxwell equations with the conducting surface imposing boundary conditions. Quantum mechanical treat-

ments focus on cavity quantum dynamics, building the electrodynamic Hamiltonians and solving for the equations of motion. The solutions from these two methods yield similar results and the experimental studies of SPCE focus on a semi-classical description. The study of this problem evolved from Sommerfeld's study of radio waves propagating near a conducting surface[5], to Chance, Prock and Sibley's study of fluorescing molecules radiating near a conducting metal[6]. Sommerfeld's work established that a dipole emitter in the prescence of a conducting surface will induce surface waves in the conductor. The work of Chance et. al. applied this work to the system of fluorescing molecules in near conducting metal surfaces. The surface waves were identified as surface plasmons in the metal film. At short separation distances, the energy transfer from the molecule to the plasmon oscillations was emphasized and established. It is this energy transfer and coupling which laid the groundwork for SPR and SPCE theory.

Sommerfeld studied the propagation of radio waves near a partially absorbing and partially reflecting surface. It was found that a radio antennae radiating close to a conducting surface (Earth) would induce surface waves in the conductor. To solve the radio problem, Sommerfeld assumed that the radiation emitted by the antenna could be described by replacing the complex geometry of an antenna with an ideal dipole emitter. This approximation is valid, given the size of the antenna in respect to the wavelength of the radiation. The system consisted of a perfect dipole radiator embedded in a homogenous medium, interacting with a homogeneous conducting medium. It was further simplified using the method of images. Boundary conditions, namely that no surface charge exists at the interface, were satisfied by placing a second emitter in the conducting medium. Maxwell's equations defined a system of differential equations. To emphasize the role of polarizations and orientations of the dipole emitters, the electric and magnetic field equations were de-

rived with the Hertz vectors of the system. In the Hertz vector formulation, the traditional electrodynamics are not described using the potentials Φ and A, but are formulated in terms of the functions Π_m and Π_e . These new functions are the Hertz vectors and are formed from the polarization (P) and magnetization (M) of a system. Sommerfeld's solution was made using the method of images solely. Transfer of energy to the surface waves was not considered. In this, and all subsequent theories reviewed, the observer was assumed to be far from the radiating system. Therefore, the far-zone radiation was studied. This resulted in fields which have a simple dependence on the observer location, with the fields falling off as r^{-1}[7].

Sommerfeld's method of solution showed the existence of surface waves propagating along the Earth-air interface. The lack of consideration for energy transfer between the dipole emitter and the conducting surface led to a failure of theory at short separation distances. This failure of the theory at short distances was studied by Kuhn[8] and by Chance, Prock and Sibley [6], who applied Sommerfeld's analysis to radiating fluorescent molecules near metal films. Drexhage's studies of fluorescent molecules near metal films described systems of short separation distances. The failure of a strict image methods solution at these distances led to approximations to Sommerfeld's theory, resulting in descriptions of how energy is transferred from the radiating molecules to the surface waves.

The review article by Drexhage in 1974[9] summarized his work on how fluorescent molecules interact with metal films. Two main results were how the separation distance between molecules and the metal surface affected fluorescence and how a metal film creates angular patterns of fluorescence. The results from these studies have formed the central data set against which theoretical models are measured.

The Drexhage studies of fluorescent molecules and metal films relied on the molecules

being an exact distance from the metal surface. This was achieved using the Langmuir-Blodgett technique: fatty-acid layers were deposited over the metal film and the fluorophores were attached to the top layer. With this process, fluorescent molecules could be placed very close (within a few nanometers) of a metal surface. This short separation distance probed the near-field interactions of fluorescing molecules and metal surfaces.

The description of a fluorescing molecule as an oscillating dipole was motivated by Morawitz in 1969[10]. A quantum system that is transitioning between excited states was treated as a harmonic oscillator. The transition current between states became analogous to the oscillating current of a dipole. Morawitz derived both classical and quantum mechanical descriptions of the interaction between a radiating molecule and a close, mirrored surface. He emphasized the applicability of the method of images, and the limitations of this method for small separation distances.

The inclusion of the field radiated by the surface waves in the equation of motion of the fluorescent molecule was described by Kuhn[8]. Treating the fluorescent molecule as a damped, harmonic oscillator, he was able to derive classical and quantum mechanical descriptions of the molecule/surface oscillation interactions. This resulted in a description of how non-radiative energy transfer could occur between the molecule and surface. The classical and quantum derivations were shown to give the same results.

In 1975, the methods of Sommerfeld were modified by Chance to studies of fluorescent molecules and the surface of conducting metal films. Similar to the work of Kuhn, they studied the effect of the fields radiated by the surface oscillations on the fluorescent molecule. Their solution relied on the Hertz vector derivation of Sommerfeld, but incorporated the reflected fields as an external force on the oscillating dipole. Instead of the harmonic oscillator model of Kuhn, they derived the Poynting vectors of the system. The

Poynting vectors describe the energy flux through a given surface, and with this method, the energy radiated away by the molecule could be described. It showed a clear delineation into energy dissipated by radiative processes (fluorescence) and non-radiative processes (energy transferred to surface oscillations). A third, more powerful method was developed by Tai[11]; the Dyadic Green's function method. This method is easily generalized to stratified media.

The work of Chance et. al., and Tai have built strong models which describe the interactions between fluorescent molecules and nearby mirrors. These models were used by Lakowicz to describe how thin metal films can be used to affect fluorescence in methods known as "radiative decay engineering"[12, 13, 2]. Radiative decay engineering has formed the basis for SPCE.

2.3 Surface Plasmons

Surface plasmons are collective oscillations of the electron density of a metal, localized within a finite distance from the surface. They are excited by incident energy in the form of light or electrons. In certain energy ranges, these oscillations can couple to photons and create a radiant signal (radiative plasmons). For other ranges, this is not possible and the plasmon energy is dissipated as heat (non-radiative plasmons). The collective plasmonic oscillation travels across the surface of a metal as a longitudinal wave, and these oscillations are known as "surface plasmon polaritons". However, for simplicity, these will be referred to simply as "surface plasmons".

The theory of surface plasmons has been extensively developed by Raether[14, 15, 16], and Ritchie[17] and Pines[18]. The oscillations are described using classical and quantum mechanical pictures. In classical terms, surface plasmons are derived as oscillations of

the surface charge density [14]. Quantum mechanically, plasmons are derived from the interaction between incident energy and the electron density of a metal.

2.4 Surface Plasmon Resonance (SPR)

SPR measurements study the effect of adsorbing thin dielectric films on metals layers[19]. SPR is observed by measuring the reflectivity of a metal film. A sharp minimum in the reflectivity is characteristic of SPR, the absorption of incident energy into surface oscillations, rather than reflection. The addition of thin organic films will create a shift in the position of this minimum, or alter the amount of energy which is absorbed into surface oscillations. SPR measurements are sensitive to the wavelength of excitation, the thickness and optical constants of the dielectric film, as well as the thickness of the metal film[20].

The work of Raether and Kretschmann [15] predicted the phenomenon of SPR, where energy incident on a surface can be absorbed into the oscillations of surface plasmons. Two configurations for the excitation of surface plasmons are described in papers by Kretschmann and Otto[15].

The development of SPR into a method to probe changes at the surface of a metal was developed with the use of Fresnel equations. Four-phase Fresnel equations provided a theoretical model for predicting the effects of optical constants and layer thickness on the shape of reflectivity curves[21].

2.5 Surface Plasmon Coupled Emission (SPCE)

The theories of SPR and SPCE are described as inverse processes. In his 2004 article[2], Lakowicz claims that fluorescence near a metal film should be able to induce plasmonic

oscillations in the metal. This is corroborated by the theory of a radiating dipole and surface waves.

In 2004, the Gryczynski research group at the University of Maryland published results on the generation of SPCE [1, 3, 4]. The work described in these papers describe two methods of SPCE generation, detailed in Figure 1-1. Detection of SPCE was made with bundles of fiber optic detectors. The works by the group studied SPCE generation from silver, aluminum and gold films. The trials with silver films (50 nm thick), created SPCE which was observable in the visible light spectrum. Aluminum (15 nm thick) and gold films (50 nm thick) exhibit SPCE in the UV and near IR spectrum, respectively.

The 2004 study of SPCE focused on the demonstration of directional emission. A highly concentrated dye dissolved in a binding solution was coated on a thin metal film. There have been several studies which use SPCE in biosensing applications [23, 22, 12, 13, 24]. These studies have explored the effects of silver particles on fluorescence [13, 12], and also continuous silver mirrors [23, 24]. SPCE has been used in the study of live muscle[23], DNA hybridization [24] and detection [22].

CHAPTER 3

THEORY

3.1 Introduction

The objective of this thesis work was to design and build an apparatus to measure the fluorescence patterns generated by surface plasmon coupled emission (SPCE). The coupling of surface plasmons to fluorescence creates a signal with distinct characteristics: high angular localization, strong polarization and a marked intensification of the signal, when compared to free space emission of fluorescence. The theory of SPCE describes how the plasmon oscillations are generated and coupled to the fluorescent signal and how this is used to create a signal. The interactions of fluorescent dye, a metal surface and electromagnetic radiation in the form of green light are described in this section.

As discussed in Chapter 1, this study focused on SPCE generated with the Reverse Kretschmann configuration (shown in Figure 3.1). Light is incident on a thin fluorescent dye layer, which is coated on a 50 nm thick silver film. The emitted fluorescence will couple to surface plasmons created in the silver film. The silver film is deposited on a glass microscope slide which is attached to a glass hemicylindrical prism. The glass interface will cause the plasmons in the silver film to couple to photons and emit a visible signal at a specific angle, referred to as θ_{SPCE}. The emission is symmetric with respect to the normal direction.

This theory section will cover four topics. The first is a brief introduction to the chemistry of fluorescence: the cycle of electronic excitation and de-excitation, and characteristics of the light emitted. The characteristics of fluorescence important to understanding SPCE will be stressed: how an excited fluorescent molecule returns to its ground state, the wavelength of emitted light, and the isotropic nature of emission. This will serve to define key terms and processes needed to compare the effects of SPCE to free-space fluorescence. The theory of SPCE will be built in the remaining sections. First, the electromagnetic description of a radiating dipole near a conducting plane will be discussed and applied to a dye molecule interacting with a metal layer. Then, the processes of Surface Plasmon Resonance (SPR) and SPCE will be discussed. SPR is a process similar to SPCE, it is related to the interaction of light with electrons in a surface via plasmonic oscillations. Whereas SPCE is determined by angular-dependent emission, SPR is determined by angular-dependent absorption.

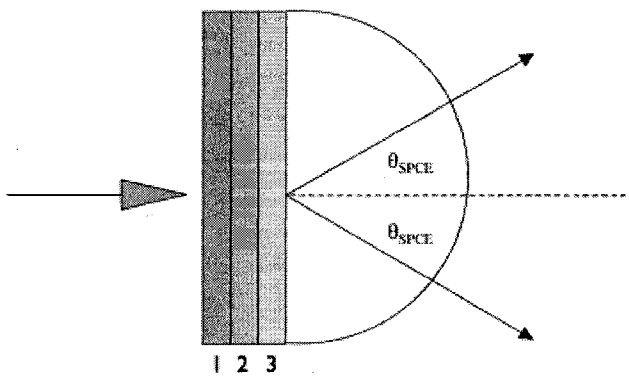

Figure 3-1: The Reverse Kretschmann configuration for SPCE generation. Fluorescence from a thin dye layer (1) interacts with a metal film (2) and emits light through a glass prism (3) in a distinct angular pattern. The emission pattern is symmetric with respect to the normal direction (broken line).

3.2 Introduction to Fluorescence

Fluorescence is the product of a photochemical reaction, it is generated by an external light source adding energy to a fluorescent molecule. It is a process which results in the emission of a photon from an excited molecule as it returns to the ground state. If an external energy source is present, the molecule may be re-excited and fluorescence emitted again. The photon emitted in fluorescence is of a characteristic wavelength, which is a longer wavelength than the exciting photon. The emission of a photon by a fluorescent molecule is not the only available pathway for a molecule to return to its ground state. The photon emission is known as 'radiative' decay. There are means of 'non-radiative' decay. These include thermal and collisional losses of energy. The process of SPCE does not mediate these non-radiative decay modes and they will not be discussed further.

A fluorescent molecule can absorb photons in a range of energies and will emit fluorescence in a range of energies. However, there is a narrow range of energies in which the molecule will absorb with a maximum cross section. Likewise there is a narrow wavelength range in which the molecule will emit the most photons.

As the fluorescent molecule transitions to the lowest energy excited state, it rapidly loses energy through nonradiative processes. When a photon is emitted, as the molecule transitions back to the electronic ground state, the light will have a longer wavelength than the exciting light. The difference in wavelength between the excitation light and the emitted light is known as the Stokes' shift. Large Stokes' shifts are ideal for SPCE since the marked difference between the laser light and the emitted light make distinguishing SPCE easier. Rhodamine Red dye, used in this study, excites in the green light range and emits in the red light range of the visible light spectrum.

The process of fluorescence is shown schematically with a Jablonski diagram (Figure

3-2). This is a diagram of the energy levels and shows the molecular transitions. It is also useful to show the different decay paths to the ground state which are available to the molecule. (It will be shown in future sections that fluorescence near a metal film will create an additional non-radiative decay path due to energy transfer to surface plasmon modes).

Fluorescence can be quantified by the efficiency with which incident photons are used in radiative decay. This is described using the quantum yield, the intensity of light emitted, and lifetime. The quantum yield of a fluorophore compares the processes which return the molecule to its ground state by radiative processes to all processes (radiative and non-radiative). In a fluorescent process, the radiative process is given by the rate constant Γ. The non-radiative processes are given by the rate constant k_{nr}. The quantum yield is thus given by,

$$Q = \frac{\Gamma}{\Gamma + k_{nr}} \tag{3.1}$$

The lifetime of a fluorescent molecule is the average time which the molecule spends in

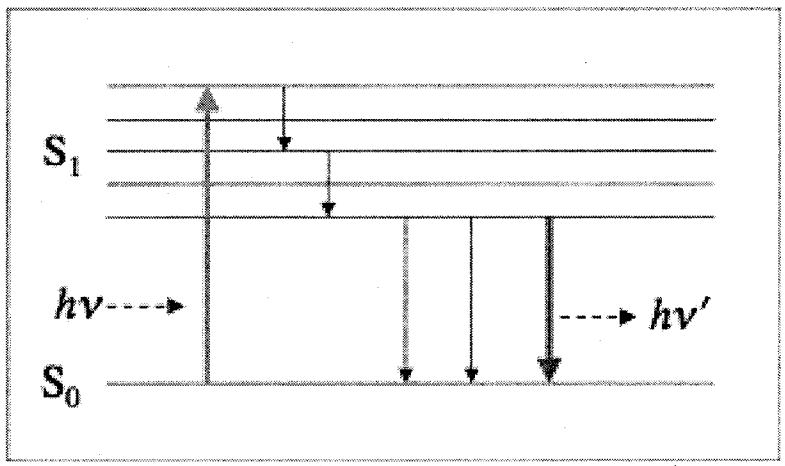

Figure 3-2: A Jablonski diagram. A fluorescent molecule is excited to a higher electronic state (green), decays to the lowest vibrational state of the excited level through non-radiative decays (black) and from that lowest level through fluorescence (red) or other non-radiative decays (black). The emitted photon has lower energy than the excitation photon

its excited state. It is given by,

$$\tau = (\Gamma + k_{nr})^{-1} \tag{3.2}$$

The creation of additional non-radiative paths will decrease the amount of time a fluorescent molecule is in its excited state.

3.3 Radiating Systems Near Reflecting Surfaces

The theory of SPCE is a semi-classical theory built upon the description of a radiating dipole antenna above a conducting surface. The validity of a classical theory for a fluorescent system, which has characteristic sizes on the order of Å, and the neglecting of quantum effects was previously discussed in Chapter 2. Treating the fluorescent molecule as a dipole antenna, the addition of a conducting surface will impose boundary conditions on the free-space radiation. Fulfilling these conditions will lead to the identification of surface waves propagating along the metal surface. These waves will be ascribed to surface plasmon modes.

The size of a fluorescent molecule, compared to its emission wavelength, is extremely small. The size of organic molecules (d) is typically on the order of tens of Å, whereas the light emitted by the molecule has a wavelength (λ) on the order of thousands of Å. Since the size of the emitter is much smaller than the wavelength of the emitted radiation ($d << \lambda$), the radiation of fluorescence can be described by approximating the system as a perfect dipole[7].

The Sommerfeld solution of a radiating dipole near a conducting medium will be discussed. It was derived to describe the effects of the Earth's surface on radio waves and shows the existence of surface waves propagating along the interface between the two media. The Hertz vectors are calculated and used to interpret the effects of the metal surface.

Using the Hertz vectors instead of the electric and magnetic potentials results in the same physics, but emphasizes the roles of polarizations.

The derivation considers a dipole, placed in a medium with dielectric constant ϵ_1, oscillating over a conducting half-space with dielectric constant ϵ_2. The geometry of the system is given in Figure 3.3. Solutions are found for three regions: (z > d) the region above the dipole in the first region, (d > z > 0) the region below the dipole and above the conducting surface boundary, (0 > z) the region inside the conducting medium.

To begin, Sommerfeld presupposes that the electric (E) and magnetic (H) fields may be derived from the Hertz vector through the expressions,

$$E = k^2\Pi + \nabla \cdot \nabla\Pi \tag{3.3}$$

and

$$H = \frac{k^2}{i\mu_o\omega}(\nabla \times \Pi) \tag{3.4}$$

That the field expression derived from equations 3.3 and 3.4 are valid is verified by showing they satisfy the vacuum Maxwell's equations. The Hertz vector is assumed to take the form

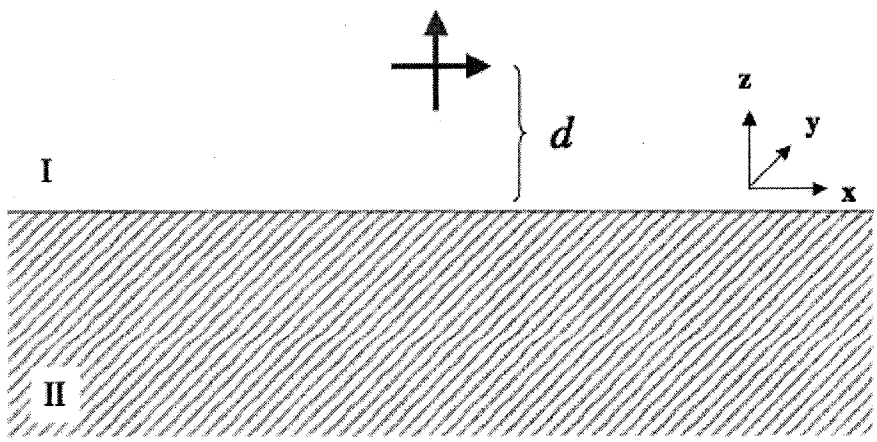

Figure 3-3: Geometry of a radiating dipole over a semi-infinite mirror. Shown are orientations for perpendicular (red) and parallel (blue) dipoles. The y-direction points into the page.

of a spherical wave[5],

$$\Pi = \frac{e^{i(kr-\omega t)}}{r} \tag{3.5}$$

The propagation constant, k, describes how a wave moves through a medium and is given by $\frac{\omega n_1}{c}$, where ω is the oscillation frequency of the radiation in the absence of damping. The vector is assumed to have harmonic time dependence, given by the exponential term $e^{-i\omega t}$. In a vacuum, the expression for k reduces to $\frac{\omega}{c}$. For a conductor, the value of n becomes complex. The complex propagation constant is given by,

$$k^2 = \epsilon\mu\omega^2 + i\mu\sigma\omega \tag{3.6}$$

The solution for the field equations is done using images of the dipole sources, located in the conducting medium. The presence of the interface at z=0 imposes boundary conditions on the Maxwell equations. The tangential components of the electric and magnetic field (E_ϕ and H_ϕ) must be continuous across the boundary.

The integral expressions for the Hertz vectors are found in cylindrical coordinates, to preserve the azimuthal symmetry of the system. The complete derivation of Sommerfeld

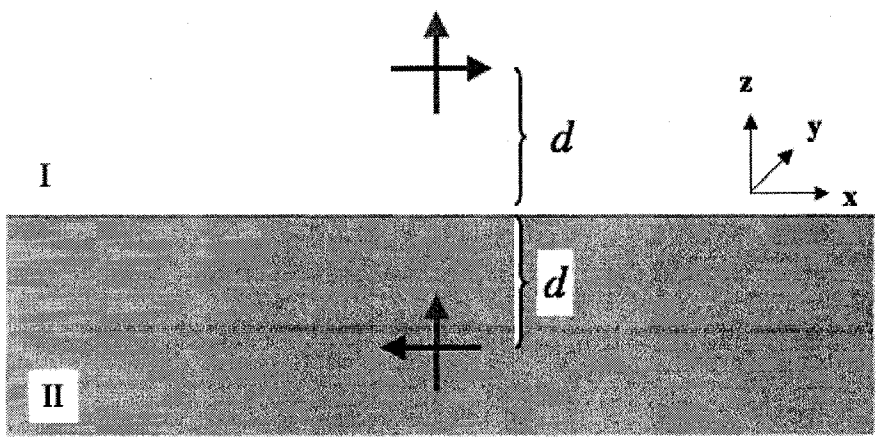

Figure 3-4: Image dipoles are located in the conducting medium and oriented as shown.

will not be replicated here, only the solution for Π in the two regions will be presented[5]:

$$\Pi = 2\sqrt{\frac{2\pi i}{pr}}\frac{k_E^2}{K}e^{ipr-\sqrt{p^2-k^2}z} \quad z \geq 0 \tag{3.7}$$

$$\Pi_E = 2\sqrt{\frac{2\pi i}{pr}}\frac{k^2}{K}e^{ipr+\sqrt{p^2-k_E^2}z} \quad z \leq 0 \tag{3.8}$$

The quantities k and k_E are the propagation constants in air and the conductor, respectively. The expression for k_E is given in equation (3.6) and k is given by $\frac{\omega}{c}$. The constants p and K relate these two propagation constants and are used to simplify the expressions. The explicit forms for p and K are given by:

$$\frac{1}{p^2} = \frac{1}{k^2} + \frac{1}{k_E^2} \tag{3.9}$$

$$K = \frac{k_E^2}{\sqrt{p^2-k^2}} + \frac{k^2}{\sqrt{p^2-k_E^2}} \tag{3.10}$$

The important results of the Sommerfeld solution are the forms of equations (3.7) and (3.8). Surface waves are identified by: the localization of the solution in the normal direction (z direction), and the oscillatory behavior along the tangential surface (r direction)[5].

3.4 Surface Plasmons

Consider a wave of electromagnetic radiation incident on a metal surface. If the energy of the radiation exceeds the metal's workfunction, an electron may be emitted from the surface. However, if the energy is below the workfunction value, a less destructive process may occur. The interaction of an electromagnetic wave and electrons at the metal surface will manifest in the form of surface charge oscillations. Just as photons represent quanta of light energy, surface plasmons represent quanta of these charge oscillations. They take the form of a surface wave propagating along the metal surface. The wave vector will dictate

whether the plasmons are radiative or non-radiative. The distinction between these two groups will be explained later.

The wave vector of a plasmon is derived from the reflection of light on a conducting surface. Assuming the geometry shown in Figure 3.3, a light wave is incident on region 2 from region 1. The wave will be partially reflected at the interface and partially transmitted. There will be oscillating electric and magnetic fields present in both regions. Following the notation of Raether[16], and assuming the radiation is a p-polarized wave,the electric and magnetic fields are written as, for region I:

$$\mathbf{E} = (E_{xI}, 0, E_{zI})e^{i((k_{xI})x+(k_{zI})z-\omega t)} \tag{3.11}$$

$$\mathbf{H} = (0, H_{yI}, 0)e^{i((k_{xI})x+(k_{zI})z-\omega t)} \tag{3.12}$$

for region II:

$$\mathbf{E} = (E_{xII}, 0, E_{zII})e^{i((k_{xII})x+(k_{zII})z-\omega t)} \tag{3.13}$$

$$\mathbf{H} = (0, H_{yI}, 0)e^{i((k_{xI})x+(k_{zI})z-\omega t)} \tag{3.14}$$

The boundary conditions used in the previous section apply here; tangential electric and magnetic fields are continuous. Additionally, the continuity of the normal components of the electric displacement vector is used to calculate the relations[16];

$$k_{xI} = k_{xII} = k_x \tag{3.15}$$

$$k_x = \frac{\omega}{c}\sqrt{\frac{\epsilon_I \epsilon_{II}}{\epsilon_I + \epsilon_{II}}} \tag{3.16}$$

$$k_{zi} = \sqrt{\epsilon_i(\frac{\omega}{c})^2 - k_x^2} \tag{3.17}$$

The tangential component of the wave vector is continuous across the boundary and it is dependent on properties of both media. The dielectric constant of the conducting region is complex, $\epsilon = \epsilon_r + i\epsilon_m$, and thus k_x is complex. Additionally, dependent on the size of

k_x, the normal component k_{zi} may be complex. If k_{zi} is complex, then the plasmon modes are defined as 'non-radiative' and cannot couple to a photon to create a light beam. The process of SPCE relies on the generation of two plasmon modes, radiative plasmons in the dye/metal interface, and non-radiative plasmons in the metal/glass interface.

3.5 Surface Plasmon Resonance

Surface Plasmon Resonance (SPR) is a process closely related to SPCE. SPR is a process by which light is absorbed into a metal film using surface plasmons. It is identified by measuring the reflectivity of a metal film, as a function of incident angle. At a specific angle, there will be a sharp minimum in the reflectivity, this corresponds to the creation of surface plasmons. To describe the reflectivity theoretically, one uses the Fresnel Equations. These are a set of relations derived from the Maxwell Equations and the boundary conditions imposed on them.

The reflectivity of a metal film is derived from the Fresnel equations[21]. These are equations describing the reflectance and transmittance of an electromagnetic wave at a surface. They are calculated with the form of the waves above and below the interface and using the continuity conditions on the normal and tangential modes of the electric and magnetic fields. The results of the Fresnel equations are constants of the reflectance and transmittance of a wave, given in terms of the amplitude of the original wave. The components of the incident wave can be decomposed into two elements: those parallel to the interface and those perpendicular to it. The continuity conditions are separated into those applied to the tangential field elements and those applied to the normal field elements. The separation of continuity conditions and wave components results in the separations of reflection constants into parallel and perpendicular components. These two parts are

independent of each other[36].

The four-phase reflectivity curves are derived in SPR literature, the systems in question consist of a prism layer (layer 1), a thin metal layer (layer 2), a thin dielectric layer (layer 3), then a bulk medium ,typically air or water (layer 4). The papers by de Bruijn illuminate how these curves can be used in determining the thickness and optical constants of the dielectric overlayer [37], [38]. The use of these curves in the theory of SPCE is outlined in the work of Gryczynski [1]. The boundary conditions outlined above and the continuity of the electrodynamic waves are calculated at each interface.

$$\begin{aligned} R &= |r_{1234}|^2 \\ r_{1234} &= \frac{n_{234} + z_{234} r_{12}^{-1} \exp(2ik_{z2}d_2)}{n_{234} + z_{234} r_{12} \exp(2ik_{z2}d_2)} r_{12} \end{aligned} \tag{3.18}$$

The expression for R relies on the functions z_{234} and n_{234}, which are defined in the three–phase reflectance at the metal, dielectric and air interfaces r_{234}. These functions and R also has a dependence on the functions r_{ij}, the two phase reflectance at each interface. They are given by,

$$r_{234} = \frac{z_{23}n_{34} + z_{34}n_{23}\exp(2ik_{z3}d_3)}{n_{23}n_{34} + z_{23}z_{34}\exp(2ik_{z3}d_3)} \equiv \frac{z_{234}}{n_{234}} \tag{3.19}$$

$$r_{ij} = \frac{\epsilon_j k_{zi} - \epsilon_i k_{zj}}{\epsilon_j k_{zi} + \epsilon_i k_{zj}} \equiv \frac{z_{ij}}{n_{ij}} \tag{3.20}$$

Also, R depends on wavevector matching between the fields above and below interfaces. The wavevector component parallel to the interface is k, and k_z is the component perpendicular:

$$k = \frac{2\pi}{\lambda}\sqrt{\epsilon_2}\sin\Theta \tag{3.21}$$

$$k_{zj} = \sqrt{(\frac{2\pi}{\lambda})^2\epsilon_j - k^2} \tag{3.22}$$

$$k_{z3} = \frac{k_4 k_2}{k_3} \tag{3.23}$$

$$\epsilon_3 = \frac{\epsilon_4 \epsilon_2}{\epsilon_3} \tag{3.24}$$

Θ is the angle of incidence and d_2, d_3 are the thicknesses of the metal and dielectric layer.

The general form of Snell's Law is also applicable here,

$$\sin\theta_t = n\sin\theta_i \tag{3.25}$$

where $n = \frac{n_i}{n_t}$ is the ratio of the indices of refraction for the metal and incident media. The complex dielectric constant of the metal layer leads to a complex index of refraction for this layer.

For surface plasmon generation, there needs to be a matching between the tangential propagation constant of the wave inside the metal, and the surface plasmon propagation constant. The propagation constant is given in terms of the index of refraction and the angular frequency of the wave, defined previously as $k = \frac{n_i\omega_i}{c}$. The tangential component of k for the wave inside the metal is found from the projection of this vector on the x-axis,

$$k_x = \frac{\omega}{c}n_m\sin\theta_m \tag{3.26}$$

The propagation constant for a surface plasmon was defined previously in equation 3.16. The subscripts I and II are replaced by 0 for the dielectric medium, and 1 for the metal layer. Thus, for surface plasmon generation, there is a matching condition on the propagation constants,

$$n_m\sin\theta_m = \sqrt{\frac{\epsilon_0\epsilon_1}{\epsilon_0+\epsilon_1}} \tag{3.27}$$

The power of the transmitted wave depends on the thickness of the film. It was shown that there is a maximum transmittance through a silver film with a thickness of 50nm[25].

SPR is identified as a sharp minimum in the reflectivity curve of a metal film. The reflectivity is calculated from the four-phase Fresnel equations, which is facilitated with the use of online applications[40]. To emphasize the effects of metal thickness, excitation

wavelength and dielectric layer thickness, three sets of curves were generated. The angles plotted are measured with respect to the normal direction.

The five curves in Figure 3-5 were made with the same excitation wavelength (532 nm) as well as the same dielectric layer thickness (10 nm). The curve corresponding to a film of 0 nm thickness (no silver film) shows a sharp increase in reflectivity at a specific angle. The reflectivity goes to unity and remains there for all angles above this specific angle. This corresponds to total internal reflection, in which light is no longer transmitted through a boundary and is wholly reflected. As the silver layer increases, a minimum in the curve at an angle above the total internal reflection angle, begins to develop. At 50 nm this minimum is at its most dramatic. This minimum becomes less dramatic as the silver film thickens, and the metal film becomes less of a semi-transparent/ absorbing layer and more of a thick mirror.

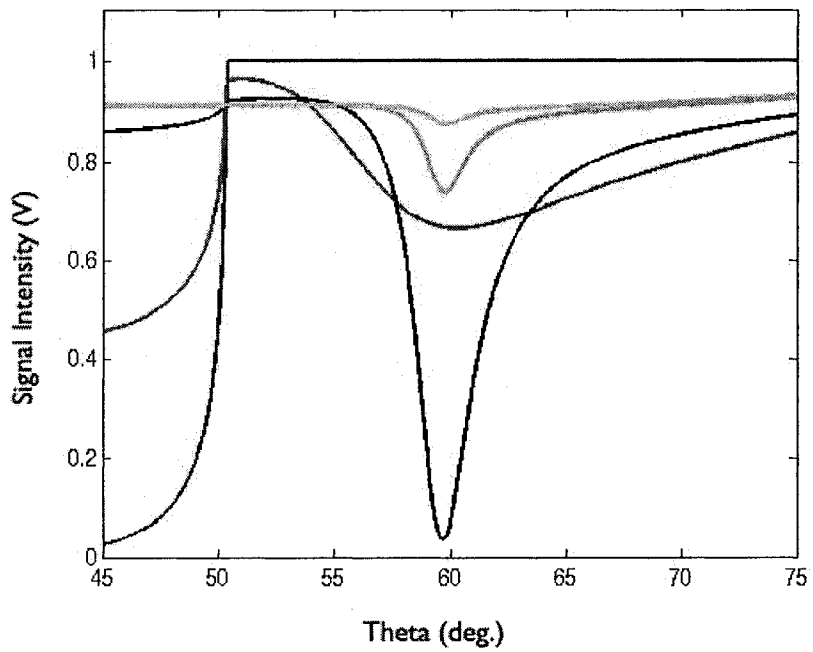

Figure 3-5: Films of thicknesses: 0 nm (blue), 50 nm (black), 20 nm (red), 80 nm (green), 100 nm (lt. blue)

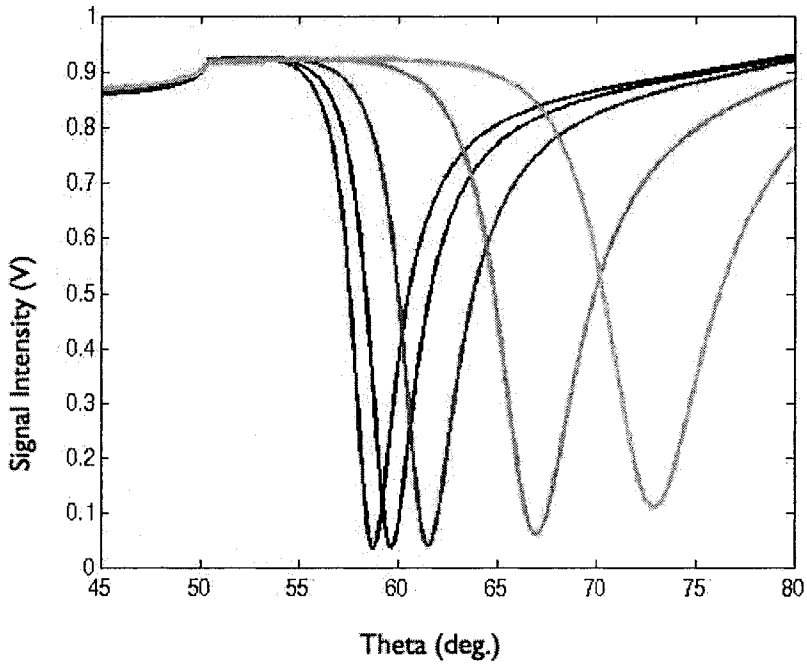

Figure 3-6: SPR curves with dielectric overlayer thicknesses of: 5 nm (blue), 10 nm (black), 20 nm (red), 50 nm (green), 100 nm (lt. blue)

The five curves of Figure 3-6 were generated with the same silver film thickness (50 nm) and the same excitation wavelength (532 nm). The increase of dielectric layer thickness predominantly shifts the location of the reflectivity minimum. As seen with the 100 nm thick layer, very thick layers will begin to diminish the ability of the silver film to absorb the incident light.

The five curves of Figure 3-7 were generated with the same silver film thickness (50 nm) and dielectric layer thickness (10 nm). Longer excitation wavelengths will shift the minimum of the reflectivity curve closer to the normal direction.

Changes in the optical constants of the dielectric layer will also shift the reflectivity minimum. As the dielectric constant of the overlayer increases, the minimum of the curve will shift away from the normal[20]. The four-phase Fresnel equation can be used to fit curves to data, with the dielectric constant, metal and dielectric film thicknesses and excitation

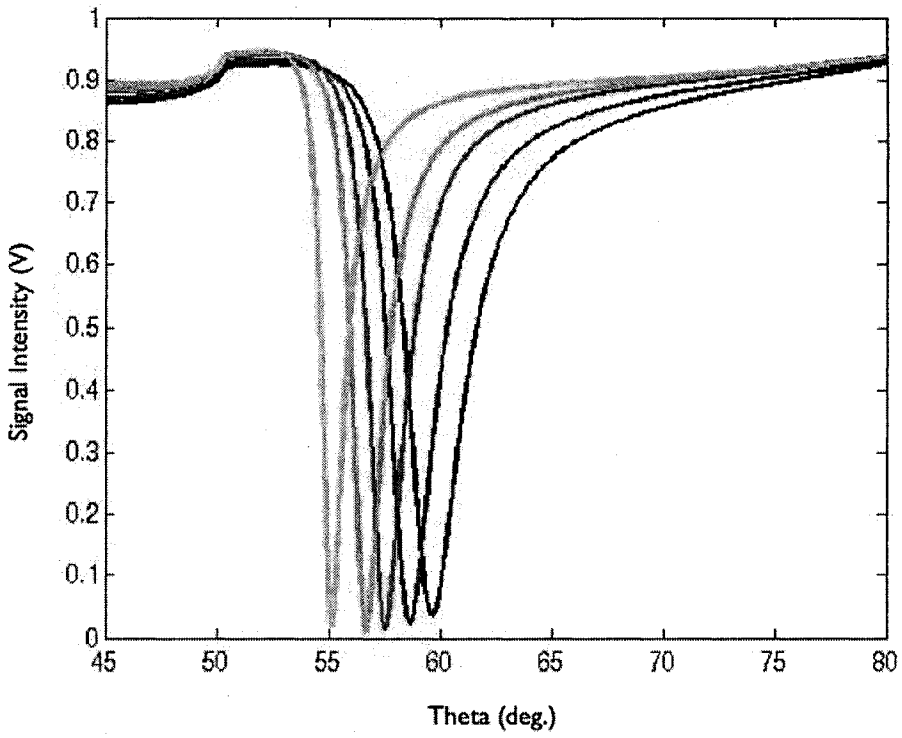

Figure 3-7: Calculated SPR curves for wavelengths: 532 nm (black), 550 nm (blue), 575 nm (red), 600 nm (green), 660 nm (lt. blue)

wavelength as variable parameters.

3.6 Surface Plasmon Coupled Emission

As mentioned before, the theory of SPCE can be interpreted as an inverse process to SPR. The process of SPCE can be summarized as follows:

- Fluorescing molecules above a silver film will induce plasmons along the silver surface.
- These plasmons will transmit the fluorescence through the film.
- There, the coupling of plasmons and photons will be mediated through a glass prism. The resulting signal is emitted in a narrow range of angles.

The fluorescing molecules can be excited by two methods. The first (Kretchmann) uses surface plasmons to excite the molecules, the second (Reverse Kretchmann) does not. These two methods are shown in Figure 1-1. The process of SPCE uses multiple plasmon modes. The surface plasmons which propagate along the dielectric/metal interface are radiative plasmons, and can couple to photons. The plasmons which propagate along the metal/glass interface are non-radiative plasmons, and cannot couple to photons[33].

CHAPTER 4

METHODS

4.1 Film Deposition and Composition

The films studied were deposited by magnetron sputtering, using ionized argon gas to bombard targets of silicon (99.999 % purity) and silver (99.99 % purity). Magnetron sputtering is a physical deposition process. Argon gas (an inert gas that won't react with the target materials) is introduced into the chamber, ionized, and accelerated towards the target. Figure 4-1 is a schematic showing the orientation of the substrate and the magnetron targets.The silver films were deposited with DC sputtering; the silicon films with RF sputtering. In DC sputtering, the acceleration of the positive ions is caused by applying a negative voltage to the target. In RF sputtering, the acceleration is caused by applying an AC voltage (13.5 MHz) to the target. The depositions in this study were carried out with constant power applied to the target. The RF sputtering was done at 125W. The DC sputtering was done with a range of powers, from 5 –100W. A magnetic field is present which traps the electrons close to the surface of the target. The initial dimensions of the targets were 3" diameter and 0.250" thick. From the magnetic field trapping and the circular paths of the ions along the surface of the target, the thickness of the targets was gradually reduced as the target was sputtered. This target erosion did not affect the quality of the deposited film.

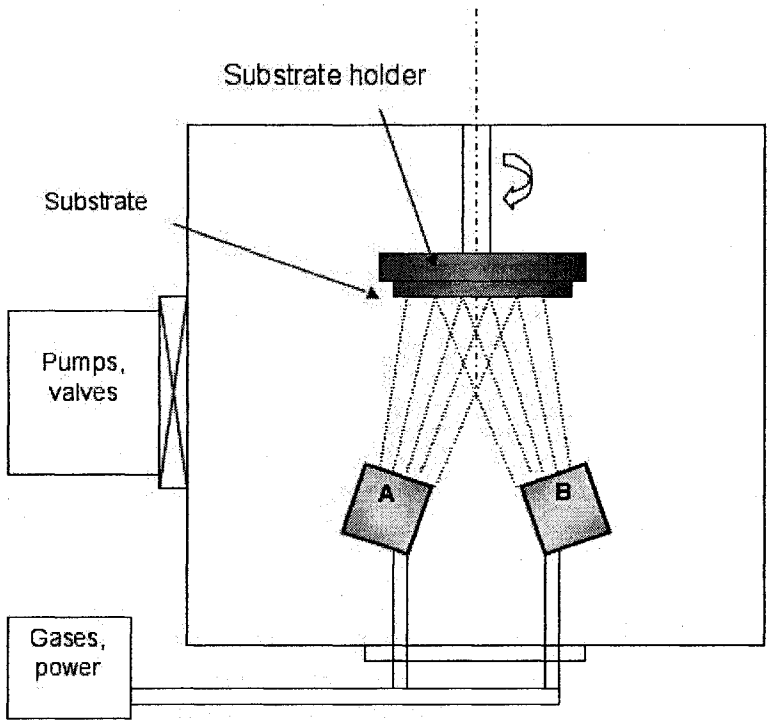

Figure 4-1: Configuration of the vacuum deposition chamber. Films are created on substrates from sputtered material ejected from magnetron targets (labeled A,B) using ionized Ar gas. (Image courtesy of James M. E. Harper)

Reactive sputtering with research grade (99.999 %) oxygen gas was used to create the passivation layer of partially oxidized silicon. In reactive sputtering, a mixture of argon and oxygen is introduced into the chamber. The oxygen reacts with the surface of the target, creating a layer of partially oxidized silicon. This oxide layer is then sputtered away by the argon ions and reforms on the substrate. The constant supply of the reactive oxygen gas assures that the oxide layer is always present on the target surface. The percentage of the reactive gas in the resulting film is controlled by the percentage of reactive gas that is introduced into the chamber. For the samples studied in this work, the passivation layer was created with an argon-oxygen mixture with 5 % or 10%, by flow rate, oxygen content.

Depositions were carried out in a low-pressure environment to prevent contamination of

the films and to prevent scattering of ions. The base pressure of the vacuum chamber, prior to deposition, remained in the mid to low 10^{-7} Torr range. Mass spectrometric analysis of the gases present in the chamber prior to deposition, showed low levels of water vapor or air. During depositions, the pressure in the vacuum chamber was kept constant at a value between 1.3 to 1.5 mTorr. Additionally, the temperature of the chamber was held at a constant temperature of 20°C. The total flow rate of process gases (argon, or argon and oxygen) into the chamber was 36.0 sccm. For the passivation layer, the oxygen was 5 % or 10% of the total gas flow into the system (1.8 sccm). Samples were deposited on 1"x3" pre-cleaned glass microscope slides from VWR Scientific and from Fischer Scientific.

Two compositions of films stacks were used in this study. Film stacks primarily investigated in this study consisted of silicon, silver and a silicon-oxide. The second material set was used to calibrate and test the sensor. It was a film stack made with aluminum-silicon (50 % Al/50 % Si), silver and an aluminum-silicon nitride (15 % nitrogen). The nitrided aluminum-silicon film was used as a passivation layer and was made by reactive sputtering of the aluminum-silicon target with high purity nitrogen gas. This second material set was used because it demonstrated the ability to generate a strong SPCE signal.

Samples were either rotated or held stationary during the silver deposition. The deposition of samples consisted of three separate depositions done without removing the sample. First, a 1 nm adhesion layer was deposited. Then, a 50 nm silver or silver-silicon film was deposited. Finally, a 10 nm passivation layer was deposited over the silver film. A complete review of depositions done over the course of this study is included in Appendix A.

To reduce the alteration of the deposited films through interactions with air and humidity, samples were kept under partial vacuum before being used for SPCE testing. Samples were placed in a dessicator chamber that was evacuated by an oil-free, PTFE-membrane

vacuum pump capable of producing a vacuum of <10 mbar. The reduced pressure environment could not be continuously maintained over the course of two months and the samples were sporadically exposed to standard pressure.

4.2 Rotated Runs

The majority of samples were prepared using a rotated substrate. Rotated runs were used to produce near homogeneous layers of silver films, with little variation in a layer's composition or thickness. For homogeneous silver layers, rotation ensured that the silver film was of an even thickness across the slides. For co-deposited silver-silicon films, rotation would create film layers of pre-determined silver to silicon ratio throughout the entire layer. Samples were rotated at constant angular speeds of 45 rpm. The samples were kept constantly rotating throughout the deposition process described above. Rotated runs were carried out with three slides in the chamber.

4.3 Stationary Runs

Stationary runs were used to create mixtures of materials and a gradient of film thickness. Samples were held stationary, parallel to the deposition direction. Stationary runs of co-deposited silver-silicon films would create a range of mixtures of silver and silicon across the slide. The samples were rotated while the adhesion layer (1 nm silicon) was deposited. Then, the rotation was stopped, the samples were oriented parallel to the deposition direction, and the silver-silicon layer was deposited. Finally, the sample was rotated while the passivation layer (5 nm silicon-oxide) was deposited. One slide was deposited at a time. A clean, 4" silicon wafer was used as a backing plate. It was placed on the substrate holder and glass

slides were then attached to the substrate holder over the wafer. During the deposition, the slide remained stationary and the resulting shadow on the wafer allowed for better reproducibility of the position of slides in subsequent depositions. Since reproducibility in stationary deposited samples depends strongly on the position of the slide, only one slide was in the chamber per deposition.

4.4 Determination of Deposition Rate

Deposition rates were determined by depositing a film through a step mask, and then measuring the film's thickness. The deposition rate for a given material is assumed to be constant, so the deposition rate is found by dividing the thickness of the film by the total deposition time. Values for deposition rates ranged from 2 nm/min (for silicon) to 25 nm/min (for silver). The addition of reactive oxygen gas decreases the deposition rate of silicon slightly. Silicon layers were deposited at the same power level, 125 W supplied by a RF power supply. For the co-deposited silver-silicon layers, the power level of the silver target had to be lowered significantly to compensate for the large disparity in deposition rates between silver and silicon. Deposition rates for silver were found at several low power levels: 50, 25, 10 and 5 W. These power levels and their deposition rates were plotted and the resulting data points were fit by a least squares method with a power curve of the form $f(x) = ax + bx^2 + c$. This line was used to determine the power levels needed to extrapolate necessary deposition rates for co-deposited films.

4.5 Adhesion Layer

An adhesion layer was used to prevent the silver film from peeling or flaking off of the glass substrate. In the two separate sample sets, the materials used for adhesion layers were aluminum-silicon and silicon. The quality of the adhesion provided by these thin underlayers was quantified by a tape test.

To conduct a tape test, a thin layer of the adhesion material (< 5 nm) was deposited upon a glass slide. A 50 nm thick layer of silver was then deposited over the adhesion layer. When the slide was removed from the chamber, a strip of adhesive tape was applied to the silver film using light pressure. The tape was then peeled off from the slide. The quality of the sub-silver adhesion layer was determined by how much of the deposited film is removed by the adhesive tape. The ideal adhesion layer would be the absolute minimum thickness required to keep the silver film from being removed by the adhesive tape. After initial tests were performed with a thin adhesion layer, more samples were made with progressively thinner adhesion layers. For the silicon series, the minimum thickness for an adhesion layer was found to be 1 nm. For the aluminum-silicon series, the adhesion layer was 2 nm.

All samples were deposited on slides that were "pre- cleaned" (according to the manufacturer). However, it was found that when the glass slides were additionally cleaned with 100 % ethyl alcohol, the thickness of the needed adhesion layer was reduced and the films did not corrode as quickly over prolonged exposure to air. Before the glass slides were put in the chamber for depositions, the glass surfaces were coated with ethyl alcohol, which was then removed by non-abrasive chemical tissue. Any remaining alcohol evaporated before the slides were introduced to the chamber.

4.6 Passivation Layer

The purpose of the passivation layer is to prevent the silver film from being compromised or corroded by its exposure to air or the fluorescent dye. The salinity of the fluorescent dye poses a significant source for erosion and reaction with the silver layer. For the aluminum-silicon samples, the passivation layer was a 10 nm thick film created by reactive sputtering of aluminum-silicon with 15 % nitrogen. The composition and thickness were determined from previous tests done in 2005. Partially oxidized silicon films had not been previously studied as a passivation layer in studies carried out at the University of New Hampshire. Optimal thickness and composition of the film had to be determined before SPCE tests could be done.

To test the quality of the oxidized films as a passivation layer, two series of samples were prepared. A 50 nm silver film was deposited on a glass slide, and then a passivation layer was deposited over it. Each series consisted of 5 samples with passivation layers made with different oxygen percentages, ranging from 0-20 % in 5 % increments. The samples in the first series of films were 10 nm thick, the second series were 20 nm thick.

Slides were left exposed to air and 1 mL of saline solution was deposited by pipette and spread across the film surface. The saline solution was made of 100 mM potassium chlorate (KCl) and 10 mM Tris buffer solution. The total solution had a ph of 8.0. The solution was left to react with the film and observations made over a four-hour period would determine which film provided sufficient protection of the silver film. Those films made with $>$ 5 % oxygen were dissolved by the saline solution and the silver film was corroded within the four hours of observation. Those films made with 0 % oxygen (pure silicon) did not dissolve, but the film surface did break and allowed the solution to corrode the silver film. An oxidized film of silicon and 5 % oxygen provided adequate protection of the silver film and was used

in the testing of SPCE.

4.7 Initial Characterization of Films

Immediate tests of the deposited films were thickness measurements and electrical resistivity measurements. The rotated runs were measured within one day of deposition. Stationary runs were measured two months after deposition.

Thickness measurements were made with a step profilometer. The stylus force was 12 mg and the scan length was 2000 μm. For rotated runs, a silicon fragment was used as a step on one of the slides. The silicon fragment is placed on top of the glass slide and held in place by substrate clip. During the deposition, the area under the fragment remains uncoated. The resulting thickness difference is measurable by the step profilometer. For stationary runs, a step was not used. Thickness measurements were made at the four shadows from the substrate clips.

Resistivity measurements were made with the sheet resistance of the film measured by four-point probe and the thickness of the film measured by the step profilometer. The four point probe measures the sheet resistance of a thin film. Four tungsten tips are placed in ohmic contact with the surface of the film. A constant current of 4.53 mA is driven through the outer two probes and through the film. While the current is applied, the voltage across the inner two probes is measured. These current and voltage readings are related by Ohm's Law; from these the sheet resistance can be calculated. The total resistivity of the sample was calculated using the equation,

$$R = R_S T \tag{4.1}$$

R is the resistivity in $\mu\Omega$-cm, R_S is the sheet resistance in $\frac{\Omega}{square}$ and T is the thickness of the film in 100s of Å. Resistivity measurements are dependent on the uniformity of the

film being tested. The two kinds of films studied have different compositional gradients. The rotated films have approximately uniform compositions, either homogenous silver or a constant percentage of silicon in silver. The resistivity was measured perpendicular and parallel to the deposition directions. These orientations are shown in Figure 4-2. The stationary films have a changing composition across the length of the slide, parallel to the deposition direction. However, the film composition is approximately uniform perpendicular to the deposition direction. Resistivity measurements were only made in this orientation, shown in Figure 4-3.

For the stationary runs, a total of 14 resistivity measurements were made along the length of the slide, each separated by 0.5 cm. The locations (a-d) marked show the positions of the clip shadows. The silicon and silver rich ends are specified. The thickness at the center of the slide was calculated as the spatial average of (a),(b) or (c),(d) thicknesses (marked in blue).

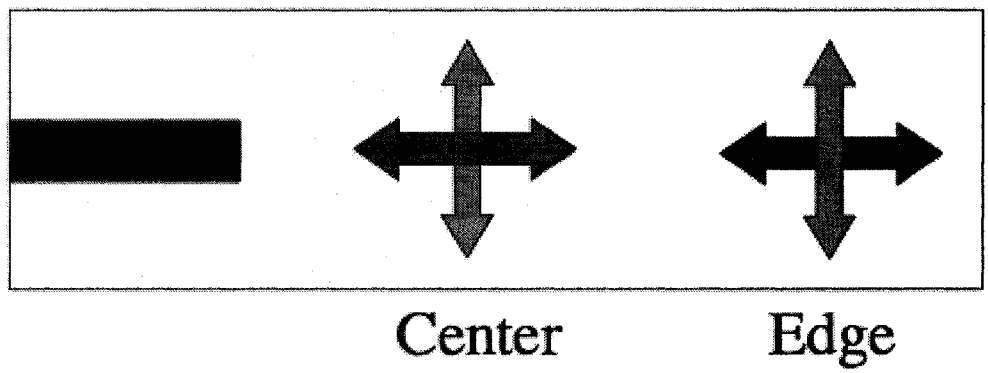

Figure 4-2: Orientations of resistivity measurements: parallel to the deposition direction (blue arrows), and perpendicular to the deposition direction (red arrows). Thickness measurements were made with the use of a silicon step on the slide (position in black)

4.8 Fluorescent Dye Preparation

For SPCE testing, slides are coated with solutions of highly concentrated fluorescent dyes. Rhodamine Red®C2 maleimide ($C_{33}H_{3}6N_4O_8S_2$, MW: 680.79) made by Invitrogen was used to test slides for SPCE signal. This dye was chosen for its photostability, excitation of fluorescence around 532 nm and relatively large Stokes' shift. The dyes were diluted in a binding solution of polyvinyl alcohol (PVA) and water.

Kari Hartman of the Biochemistry Department prepared dye concentrations in November of 2006. The dye concentrations were kept at a consistent temperature of -20°C. Two concentrations of dye solution were prepared; 0.660 μM and 1.32 μM. The concentrations were prepared by dissolving the dye in a solution of 0.01 M Tris buffer and 0.1 M KCl. The resultant dye solutions, when degassed, had pH of 8.3. A prolonged storage decreased the quality of this prepared dye. A second dye concentration was prepared in March of 2007. Like the first solution, the second dye solution was dissolved in a Tris buffer solution. However, the dye was diluted in a solvent and the concentration of the dye was not known. Although the concentration of the resulting dye mixture was not known, a sample of the

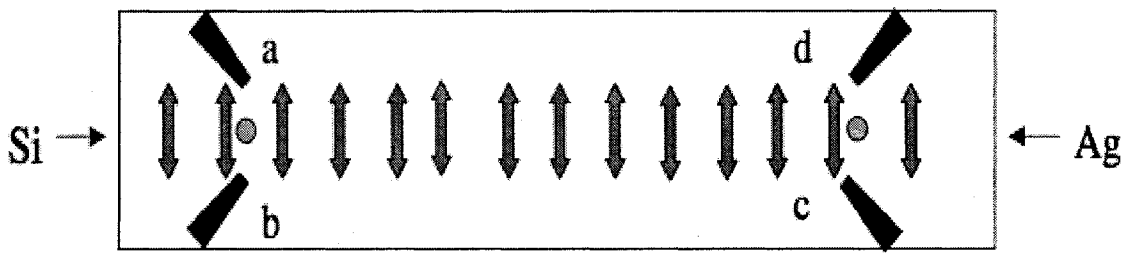

Figure 4-3: Orientations of resistivity measurements: perpendicular to the deposition direction (red arrows). Thickness measurements were made with the shadows of the substrate clips on the slide (positions in black)

fluorescent dye was illuminated in a micro-plate reader. The light emitted was measured and the resulting signal verified that the dye emitted strong fluorescence.

The binding solution is a 1% by weight PVA solution. The density of liquid PVA at 25°C is 1.08 g/mL and the density of water is assumed to be 1.00 g/mL. Prior to preparing the solution, the PVA was stored according to the manufacturer's direction, at 0°C. To prepare the 1% solution, a solution with 0.1 mL of PVA per 10 mL of water was heated to 100°C. Once this temperature was reached, the solution was heated for 1 hour with continuous stirring. The solution was allowed to cool to 25°C before adding the dye concentration. Before preparing the PVA solution, the dye concentrate was removed from the freezer, allowing the dye to warm to 25°C before it was added to the PVA. The resulting dye solutions were in a 1:10 dilution.

4.9 Spin Coating

For SPCE testing, a thin, uniform dye coating over the deposited film stacks was necessary. Based on the techniques used by Professors Ignacy and Zygmunt Gryczynski, which were observed during the summer of 2005, the dye deposition was done by spin coating. Samples were individually coated: each glass slide was fitted into a custom milled mount and was held securely in the mount during rotation by vacuum. Samples were rotated at 2200–3300 rpm for 90 seconds. The total spin coating time included the acceleration and deceleration phases. A 1 mL volume of dye was deposited onto the surface of the sample by pipette. When initially deposited, the pipette tip was used to lightly distribute the dye across the surface of the sample. The subsequent spin coating would cause minimal spreading of the dye solution, using the pipette to spread the dye ensured that the final coating would cover the microscope slide.

4.10 Electronics

The apparatus was driven by a 120 V AC power supply. This was directed into a 12 V DC power supply and a 15 V DC power supply. These were used to operate a small diode laser, a PMT and a transimpedance amplifier. Output of the PMT was a current and had a maximum of 100 μA. The amplifier was attached to the PMT output and used to convert and amplify the current output to a voltage output. The laser and the PMT both had voltages which could not be exceeded, otherwise the equipment would be damaged. The laser could not be operated at voltages above 3 V and the PMT could not be operated above voltages of 0.9 V. Circuits were built to ensure that these voltages could not be exceeded.

4.11 Construction of the Apparatus

The apparatus was constructed out of aluminum, chosen for its strength and machinability. The final apparatus measured 18" W x 9" H x 12" L. The electronics driving the laser, PMT and amplifier were housed on an aluminum platform. The laser was attached to an arm which also attached to this platform. The prism was placed at the end of the arm. This was elevated on threaded rod, which allowed for flexibility in the height of the laser and prism.

The stepper motor was mounted on a second, lower platform, 2.5" away from the first. The detector was mounted with Linos optical pieces, and attached to an arm of aluminum U-channel. The arm was connected to the lead screw of the stepper motor. For the stepper motor to define a home position, it needed to trigger a Hall sensor. A small recess was ground into the plate and the sensor was clamped there, held vertically.

4.12 Laser Mount

The laser module was covered in heat-shrink and mounted in pieces from a Linos optical system. It was possible to adjust the positioning of the laser in the x-y plane. The heat-shrink coating kept the module protected against electrical shorts.

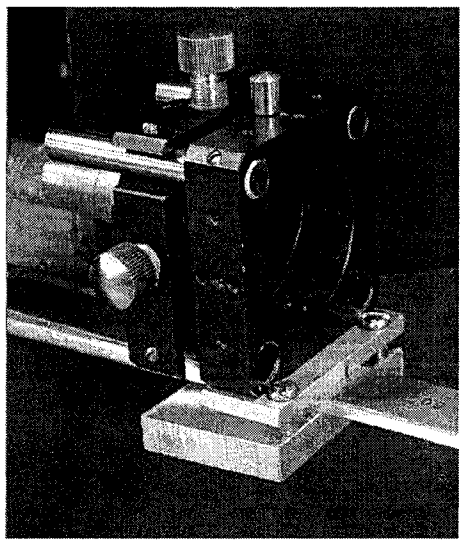

Figure 4-4: Detail of the laser mount. The laser module is mounted in an x-y adjustable Linos mount.

4.13 Detector Mount

The detector, wavelength filter and aperture were all mounted in pieces from a Linos optical system. This housing was secured to a piece of aluminum U-channel. The U-channel was attached to the leadscrew of the stepper motor with a set screw. A piece of nylon tubing was wrapped around the lead screw in order to extend its length, and also to provide a material the set screw could grip.

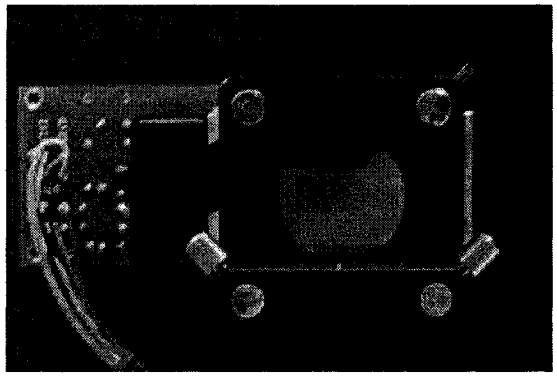

Figure 4-5: Front view of the detector housing. The filter is visible.

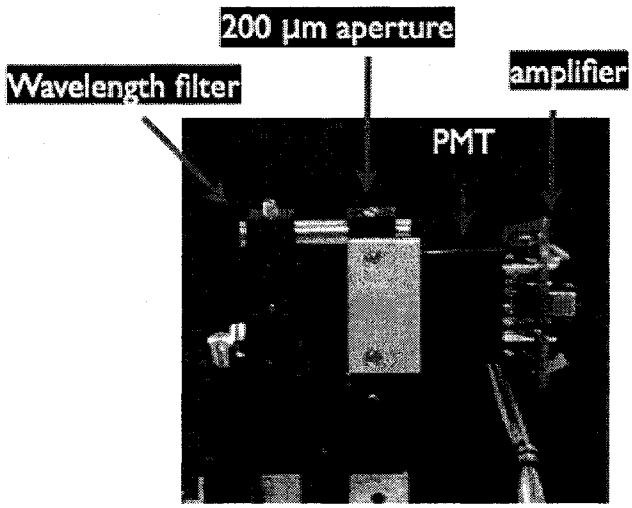

Figure 4-6: Side view of the detector housing, highlighting the filter, aperture, detector and amplifier.

4.14 Reflectance and Transmission Measurements

The film stacks were tested by an automated apparatus in a light tight environment. The functions of the apparatus can be summarized as three components: the excitation of fluorescent dye by the laser, the collection of the transmitted light and the rotation of the detector around a sample. A LabVIEW program was written to execute and synchronize these three components.

A 532 nm laser (green light) was used to excite the fluorescence dye. The wavelength of the laser is near the peak excitation wavelength for Rhodamine Red dye (570 nm). The laser had a power output of 1.5 mW and was kept at a distance of 7.5 cm from the fluorescent surface. The orientation of the laser light, film and prism are shown in Figure 4.4.

The slides were attached to a hemicylindrical glass prism (index of refraction, n=1.5) with a thin layer of glycerol, an index matching fluid. The slide was held secure with electrical tape strips wrapped around the slide at the top and bottom of the slide. Additionally, a vertical strip of electrical tape was attached to the prism, aligned with the laser light. The wavelength filter used would block most of the green laser light. However, some of the light will still transmit and reach the detector. The PMT was operated at voltages near its threshold voltage (0.9 V) and the intensity of the laser light would possibly damage the detector. During the testing, the surface of the slide was kept at a fixed distance from the laser, maintained a fixed orientation perpendicular to the laser, and was held securely by double-sided adhesive tape.

The light transmitted through the film was collected with a Hamamatsu photomultiplier module (PMT). The detector is sensitive to ambient light. To prevent damage to the detector, all measurements were conducted in a light tight environment created by an enclosing box made from blackout materials. The multialkali cathode has an effective surface area of 8 mm^2. To improve the angular resolution and to reduce the amount of scattered light that entered the detector, a 200μm aperture was used. The slit was positioned 5.5 cm from the sample. The acceptance angle for slit size and distance is 0.104°. Additionally, to detect the fluorescent dye signal, a filter to block wavelengths below 600 nm was aligned in front of the aperture. The current generated from the PMT was converted to a digital signal using a digital acquisition module (DAC).

The detector was rotated around the prism through an angle of 180°, driven by stepper motor that was capable of generating torque of 3200 g-cm. Torque generated by the motor needed to be large enough to counteract the torque created by the weight of the detector and the moment of inertia of the arm. A turntable was used to reduce the strain on the lead screw of the motor and to aid in the smoothness of the motion. Also, to minimize the arm's moment of inertia, the detector was positioned as close to the leadscrew as possible.

4.15 Control Programs

Three programs were used to control the motion parameters of the motor and the measurements of the detector. The first program was written and distributed by the stepper motor manufacturer (Zaber). This program controls parameters of the stepper motor. Through this program, the speed at which the motor would move, and the home position offset were controlled. These parameters were determined and set prior to making any measurements.

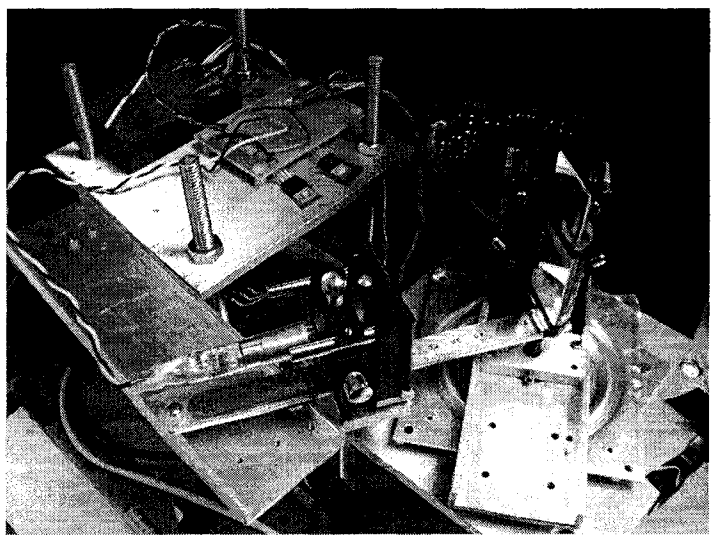

Figure 4-7: Orientation of the laser, sample and detector. The laser is shown in the foreground, with the prism positioned on the end of the arm. The detector is shown angled behind the prism.

The remaining two programs were written in LabVIEW to control step size, step direction, and length of SPCE scans.

Both LabVIEW programs were designed to synchronize and drive the detection system and share the same initial steps. The programs controlled the step size of the motor, the amount of time with which the detector would collect samples, the direction of the scan and the voltage supplied to the PMT. Every measurement began with determining the voltage supplied to the PMT. Then, the stepper motor would define a home position. After the home command was issued to the motor, it would rotate counterclockwise until a Hall sensor triggers. After this, the motor retracts a preset distance, and defines its home position. Once the motor is sent home, the user will define the step size (in degrees) and the total number of steps for the motor to take. The number of steps and step size were chosen such that the total angle traveled does not exceed 180°, otherwise the detector would collide with the laser mount. The stepping of the detector and the measuring of the light were carried out in the same loop. When the user defines the total steps, the program then doubles the value. For odd numbered iterations, the motor advances by the defined step size. For even numbered iterations, the current read by the PMT is recorded. The first program which was written would only complete a scan in one direction, with the detector rotating clockwise around the sample.

The second program added a second, counter-clockwise scan to the sequence. Once the clockwise scan was completed, the motor would then step in the reverse direction, again stepping and recording the signal on alternating iterations. The second program allowed for different step sizes and collection times to be used for the clockwise and counterclockwise scans. However, for the scans detailed in the next chapter, identical step sizes and collection times were used for both scans.

The step size of the motor affected the resolution of the measurements. The motor is capable of providing angular resolution of 0.028°. These high-resolution capabilities were not employed: one degree or half-degree steps were used. Measurements were made with a fixed collection time of 0.75 seconds. The voltage supplied to the PMT affected the gain of the detector. For SPCE measurements, voltages ranged from 0.75 to 0.85 V. Voltages never exceeded 0.9 V because voltages higher than this would severely damage the PMT.

4.16 Comment on the Co-deposited Silver-Silicon Films

The stationary runs described in previous sections were used to deposit films of mixed compositions (silver and silicon mixed in the same layer). A series of samples were made with varying percentages of silver and silicon in the SPCE layer. These samples vary across the length of the slide from areas of pure silicon, to an intermediate state of mixed silver and silicon, to areas of pure silver. These films have not yet been tested for SPCE. Descriptions of these depositions, and all depositions done during this thesis, are presented in Appendix D.

Chapter 5

Results

The results given in this section summarize the measurement of SPCE with the automated apparatus. Included are results showing the effect of PMT operation voltage, stepper motor resolution and direction of rotation on the strength of SPCE peaks and their locations. Initial testing has shown that SPCE scans made with step sizes of 1° are reproducible and show a low amount of angular drift.

5.1 Overview of the Experiments

In testing the slides, the focus was on consistency, reproducibility and quantifying different material sets. Identical scans were performed to detect angular drift. It was observed that the peaks in these repeated scans were at the same position, but had wildly different heights. Thus, the order in which repeated scans were done was changed. Additionally, it was noticed that the two peaks were of different heights. Adjustments to the prism orientation was made in attempts to even them out. Smaller step sizes were used in order to produce scans with higher resolution. The direction of scans was reversed to detect any angular shift from the stepper motor.

After these parameters were explored, new material sets were tested. In all, five film stacks were tested. They were made from two sets of materials: AlSi/Ag/AlSi-N (15% Nitrogen), Si/Ag/SiO(x) (5% Oxygen) and Si/Ag/SiO(x) (10% Oxygen). The majority of

SPCE tests focus on film sets of AlSi/Ag/AlSi-N (15% Nitrogen) (with both 34.1 nm and 50 nm silver layers) and of Si/Ag/SiO(x) (5% Oxygen). Additional tests were made with Si/Ag/SiO(x) (10% Oxygen) and Si/Ag/SiO(x) (5% Oxygen) with a thicker passivation layer. Samples of different compositions were scanned with identical settings to compare the signal generated by each.

The data generated in LabVIEW was viewed as signal intensity vs. angle plots in Matlab. Single Gaussian curves were fitted to the data using a least squares algorithm available in the Curve Fitting Toolbox. A complete set of the raw data and fits is presented in Appendices B and C. The results in this section will be presented with an emphasis on the reproducibility of measurements: the locations of peaks and the intensity of SPCE signals. Also, the results from different material sets will be presented.

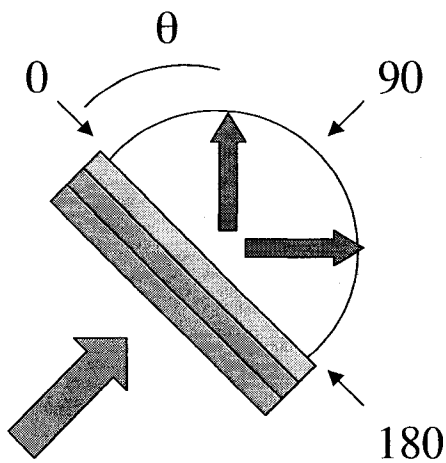

Figure 5-1: The geometry of a SPCE scan. Scans begin at 0° and proceed clockwise. The normal direction corresponds to 90°.

The geometry of an SPCE scan is shown in Figure 5-1. All scans start from 0°, which is located on one edge of the prism. A full 180° scan will end at the other edge of the prism. The normal direction, to the film surface, occurs at 90°. Two peaks can be measured. One occurs in the region of $0 < \theta < 90°$ and the other occurs in the region $90° < \theta < 180°$.

5.2 Detection and Angular Reproduction of SPCE signals

A detectable SPCE signal was first found using a sample of AlSi/Ag/AlSi-N (15% N) with a silver film that was not 50 nm thick, but only 34.1 nm. A plot of intensity vs. angle is shown in Figure 5-2. The two peaks due to SPCE were sharply defined and distinguishable from the background. SPCE peaks were detectable for PMT voltages higher than 0.75 V and plots of scans with increasing voltages showed a gradual increase in peak height (Figure 5-3). The maximum peak height was detected when the PMT voltage was 0.84 V.

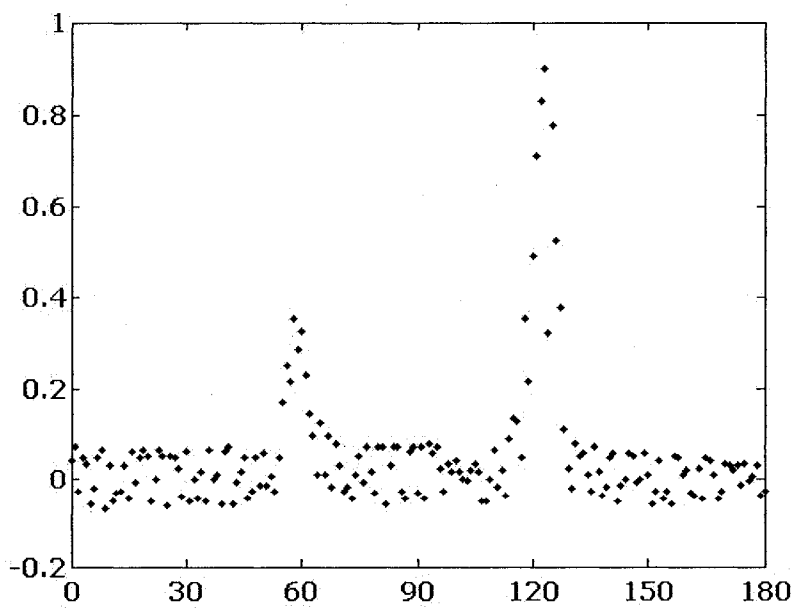

Figure 5-2: First Detected SPCE sample: SPCE scan with PMT voltage 0.84 V. The peaks corresponding to SPCE are seen near 60° and 120°.

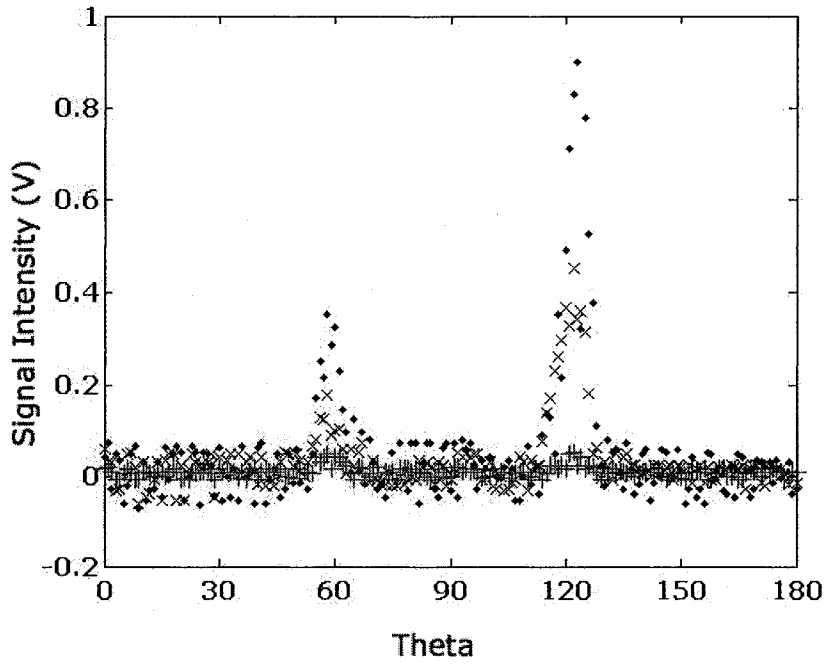

Figure 5-3: SPCE scan with varying PMT voltages. Shown are 0.84 V (blue x), 0.84 V (black dot), and 0.79 V (red cross).

After a SPCE signal could be measured, identical scans were made to ensure that it was reproducible. Five scans were made at the highest PMT voltages; 0.82 V, and 0.84 V. The repeated scans did show a SPCE signal, however the intensity of the signal varied. Shown in Figure 5-4 is the series of repeated scans at 0.84 V. In these runs the goal was reproducibility of the signals and their locations. The sample and prism were not moved or adjusted.

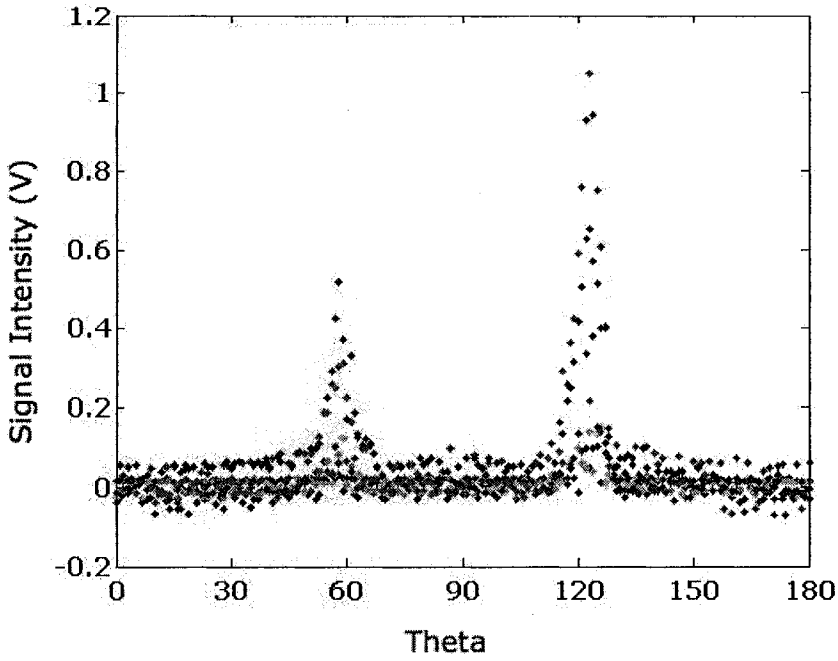

Figure 5-4: Five repeated scans done at 0.84 V.

The next set of repeated scans, (made on April 23, 2007) were done with six PMT voltages: 0.75, 0.77, 0.79, 0.82, and 0.84 V. Rather than repeat a number of runs at the same PMT voltage, the voltage was increased through the range of voltages, then repeated. A scan was conducted at 0.75 V, then 0.77 V, then 0.79 V, and after 0.84 V the series would repeat. The resulting series of scans at a given voltages were more uniform in height. Shown in Figure 5-5 is the series of scans at 0.84 V conducted in this manner.

To determine if the peaks occurred at the same location, the data from LabVIEW was fitted with Gaussian curves of the form,

$$G(x) = Ae^{-(\frac{(x-b)}{c})^2} \tag{5.1}$$

The fit parameter b corresponds to θ_{SPCE}. An example of a fitted set of SPCE peaks is shown in Figure 5-6. The five curves in Figure 5-4 and the three curves in Figure 5-5 were fitted and the resulting SPCE angles are given in Table 5.1 and Table 5.2. The uncertainties

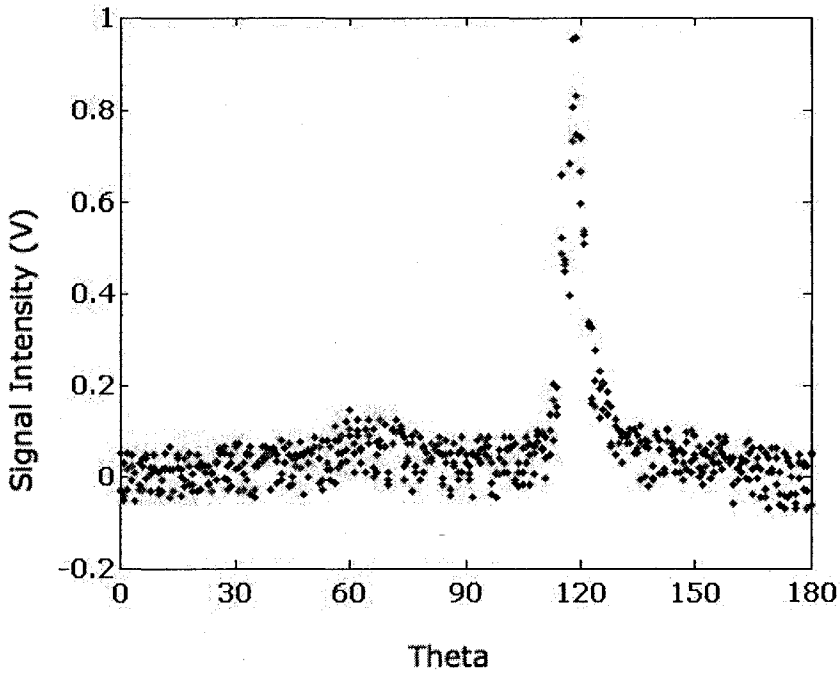

Figure 5-5: Multiple scans at 0.84 V after cycling through lower voltage values.

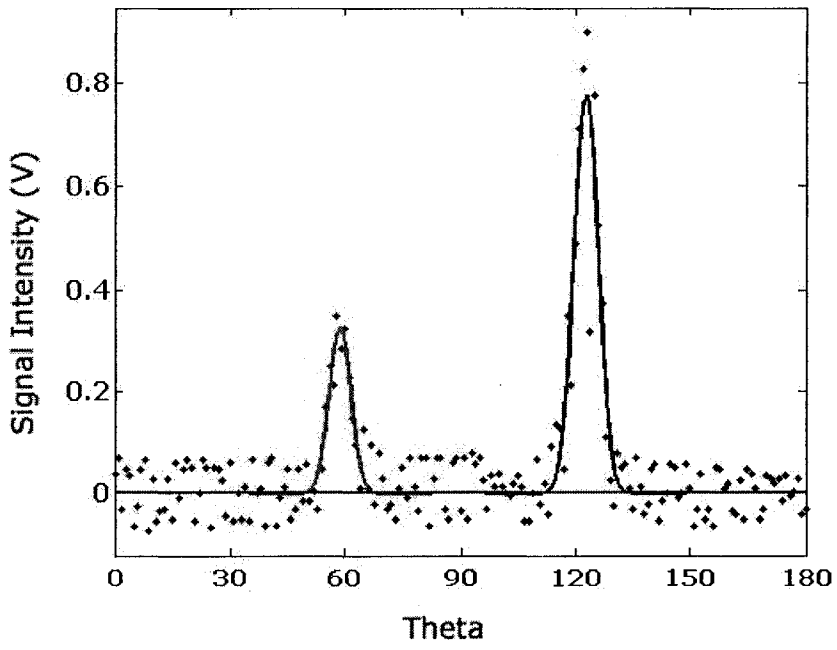

Figure 5-6: Example of fitted SPCE data (grey) with Gaussian curves (red,blue).

in the angles are generated in the curve fitting algorithm.

Table 5.1: Calculated values for θ_{SPCE} at PMT Voltage 0.84 V, constant voltage.

Run Number	θ_{SPCE}	θ_{SPCE}
Figure 5-4 01	57.8 ± 1.4	122.8 ± 0.3
Figure 5-4 02	58.3 ± 0.6	122.7 ± 0.2
Figure 5-4 03	56.6 ± 1.6	124 ± 0.9
Figure 5-4 04	58.0 ± 1.1	122.9 ± 0.8
Figure 5-4 05	57.7 ± 1.0	123.2 ± 0.3

Table 5.2: Calculated values for θ_{SPCE} at PMT Voltage 0.84 V, voltage varied.

Figure 5-5 01	67.9 ± 11.9	118.7 ± 0.4
Figure 5-5 02	64.2 ± 6.2	118.7 ± 0.3
Figure 5-5 03	63.8 ± 5.3	118.3 ± 0.2

5.3 Step Size

The step size used in a scan ranged from 1.0° to 0.1°. Most scans were done with step sizes of 0.5° or 1°. Shown in Figure 5-7 are a series of scans of a Si/Ag/SiO(x) (5% Oxygen) slide, with step size ranging from 0.1° to 0.2°. Shown in Figure 5-8 are scans of a Si/Ag/SiO(x) (5% Oxygen) slide with step sizes 0.5° and 1.0°. The smaller step sizes were used with the intention of producing scans with higher resolution, and more data points in the fluorescence

peaks. The discrepancies in the SPCE angles for smaller step sizes will be discussed in the following chapter.

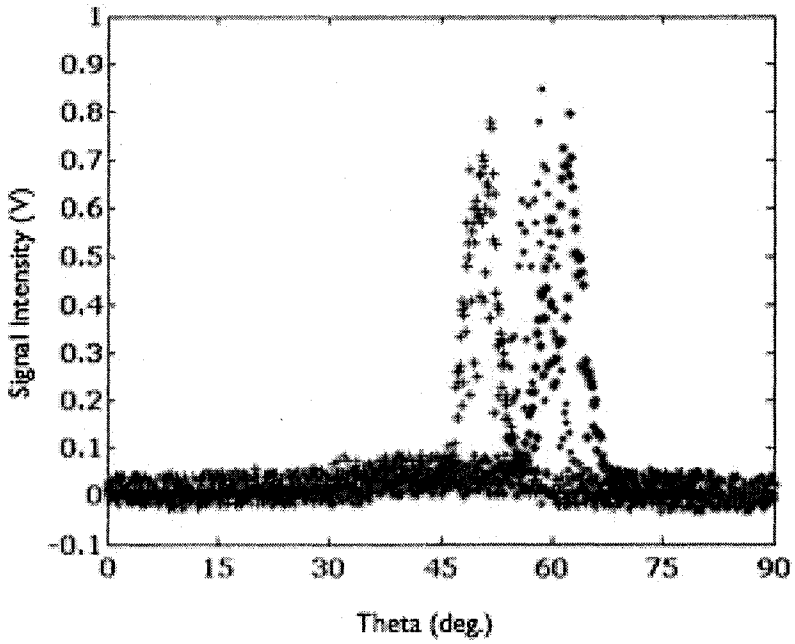

Figure 5-7: Step sizes of 0.1° (black cross), 0.15° (blue asterisk), and 0.2° (red dot).

5.4 Reverse Scans

The scans detailed above were all done with the detector moving clockwise around the sample. It was recommended by Karol Gryczynski that scans were performed in a counterclockwise direction also; to measure the angular accuracy of the stepper motor. Scans were made on AlSi/Ag/AlSi-N (15% Nitrogen) samples. These scans were made with 1.0° step sizes and also 0.5°, 0.25°, 0.2° and 0.1° step sizes. Scans with 0.5° and 1.0° step sizes were done from 0° to 180°, measuring both SPCE peaks in both directions. The scans with shorter step sizes were run from 0° to 100°, measuring only one SPCE peak in both

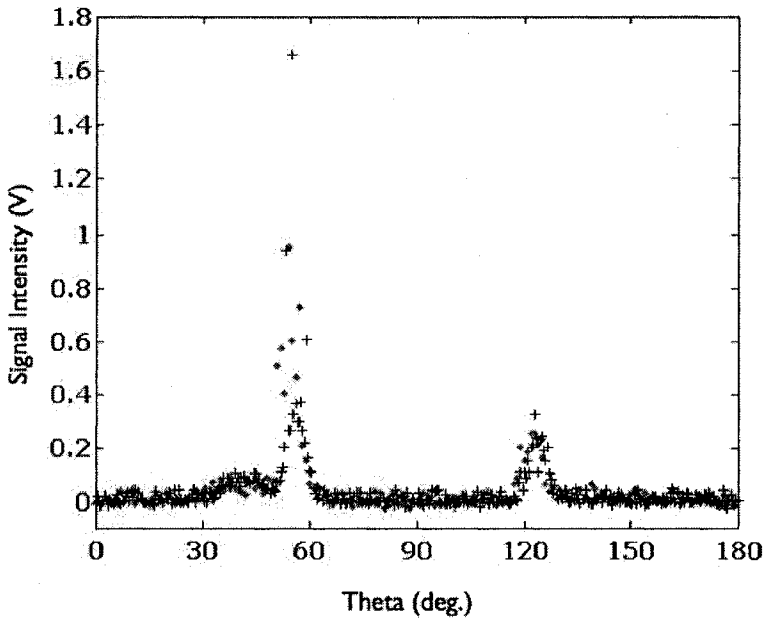

Figure 5-8: Step sizes of 0.5° (black cross), and 1.0° (red dot).

Table 5.3: SPCE angles for CW and CCW scans with 1° step size

Run Number	θ_{SPCE}	θ_{SPCE}
Figure 5.11 CW	67.3 ± 0.1	135.9 ± 0.3
Figure 5.11 CCW	68.2 ± 0.3	136 ± 0.3

directions. In Figure 5-9, a clockwise (CW) and counterclockwise (CCW) scan with 1° step size are shown. The associated fits are given in Table 5.3. Figure 5-10 shows clockwise and counterclockwise scans made with 0.2° step sizes. The associated fits are given in Table 5.4.

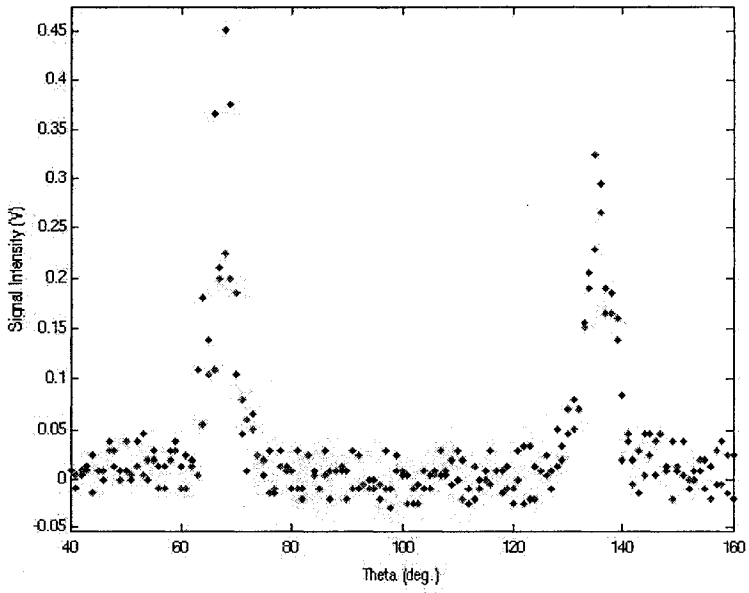

Figure 5-9: Clockwise (red) and counterclockwise (black) SPCE scans with 1° step size.

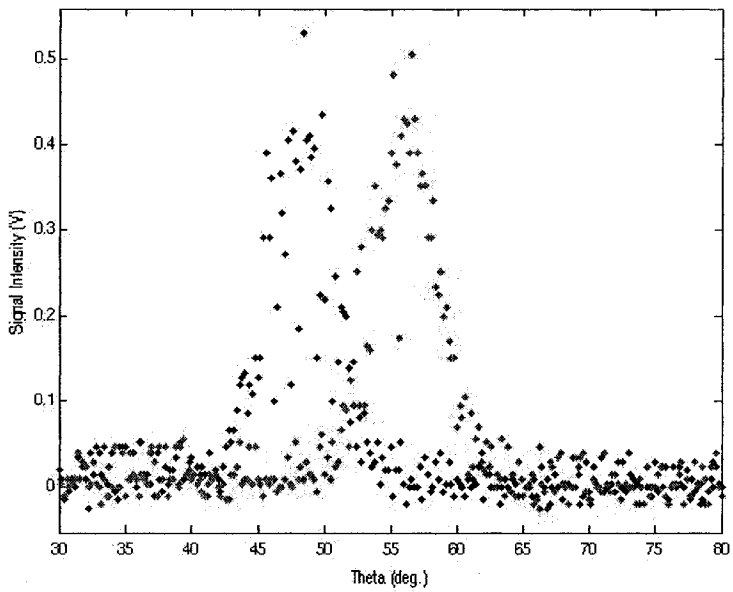

Figure 5-10: Clockwise (red) and counterclockwise (black) SPCE scans with 0.2° step size.

Table 5.4: SPCE angles for CW and CCW scans with 1° step size

Run Number	θ_{SPCE}
Figure 5.12 CW	48.2 ± 0.1
Figure 5.12 CCW	56.1 ± 0.1

5.5 Si/Ag/SiO(x) (5% Oxygen, 50 nm Ag)

The next film stacks studied were made with silicon adhesion layers and partially oxidized silicon passivation layers. The samples were tested with a range of PMT voltages (0.75 V-0.84 V) and the voltages were cycled through. Plots of the scan are given in Figure 5-11 and the associated fits are given in Table 5.5.

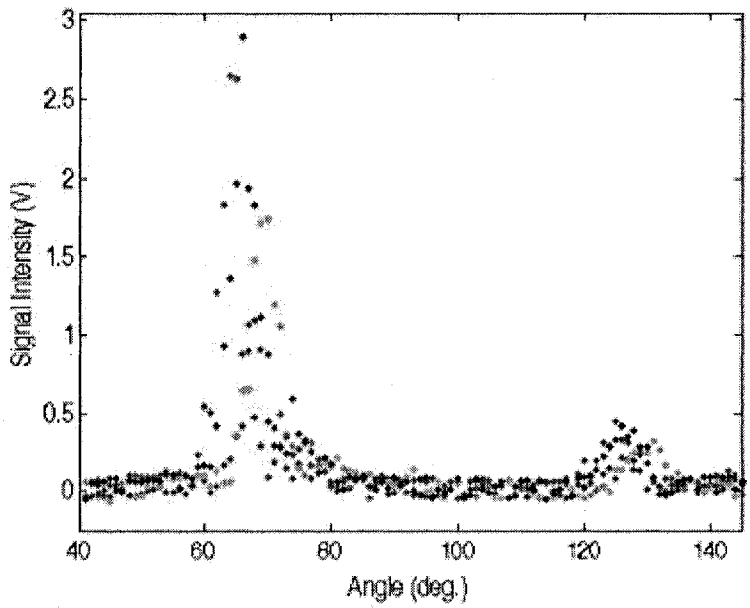

Figure 5-11: SPCE signal from Si/Ag/SiO(x). PMT voltages of 0.75 V (black), 0.79 V (blue), 0.84 V (green), 0.84 V(red)

Table 5.5: Associated fits for Si/Ag/SiO(x) SPCE scans

Run Number	θ_{SPCE}	θ_{SPCE}
Figure 5.6 0.75 V	68.4 ± 0.2	127.1 ± 0.8
Figure 5.6 0.79 V	69.5 ± 0.2	129.9 ± 0.6
Figure 5.6 0.83 V	64.2 ± 0.2	124.9 ± 0.5
Figure 5.6 0.85 V	66.2 ± 0.2	126.4 ± 0.4

5.6 AlSi/Ag/AlSi-N (15 % Nitrogen, 50 nm Ag)

Samples with 50 nm thick silver layers were deposited in May 2007, and tested to see if the thicker silver film would intensify the SPCE signal. The peaks and associated fits are given in Figure 5-12 and Table 5.6.

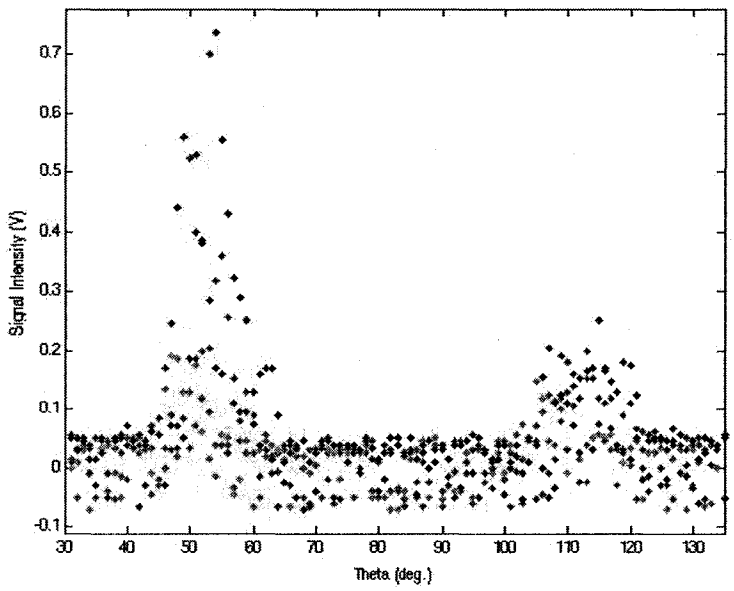

Figure 5-12: SPCE scans of a 50 nm Ag film in AlSi/Ag/AlSi-N (15% N) stack. PMT voltages of 0.75 V (red), 0.79 V (green), 0.82 V (grey), 0.84 V (blue) and 0.84 V (black) are shown.

Table 5.6: SPCE Angles for AlSi/Ag/AlSi-N (15% Nitrogen, 50 nm Ag)

Run Number	θ_{SPCE}	θ_{SPCE}
Figure 5.7 0.75 V	50.8 ± 1.0	108 ± 1.8
Figure 5.7 0.79 V	48.3 ± 0.8	106.2 ± 1.9
Figure 5.7 0.82 V	54.4 ± 0.5	114.1 ± 1.1
Figure 5.7 0.84 V	50.0 ± 0.3	111.9 ± 0.9
Figure 5.7 0.84 V	54.3 ± 0.3	117.5 ± 1.7

5.7 Si/Ag/SiO(x) (10% Oxygen, 50 nm Ag, 20 nm passivation layer)

Silicon samples with higher oxygen percentages in the passivation layer were tested. These films contained a 50 nm silver films, but were transparent. Figure 5-13 shows a representative sample of the scans at several voltages. The associated fits from MatLab are given in Table 5.7.

5.8 Si/Ag/SiO(x) (5% Oxygen, 50 nm Ag, 20 nm passivation layer)

Silicon samples with thicker passivation layers were tested for SPCE signals. Scans are shown in Figure 5.9 and associated fits are given in Table 5.5.

Table 5.7: SPCE angles for Si/Ag/SiO(x) (10% Oxygen) slides

Run Number	θ_{SPCE}	θ_{SPCE}
Figure 5.8 0.75 V	47.4 ± 2.2	105.3 ± 5.4
Figure 5.8 0.77 V	61.0 ± 6.1	111.8 ± 5.2
Figure 5.8 0.79 V	54.8 ± 2.1	115.9 ± 5.0
Figure 5.8 0.82 V	53.3 ± 0.7	112.9 ± 2.3
Figure 5.8 0.84 V	55.2 ± 1.3	115.1 ± 2.1
Figure 5.8 0.84 V	55.0 ± 0.8	112.6 ± 1.0

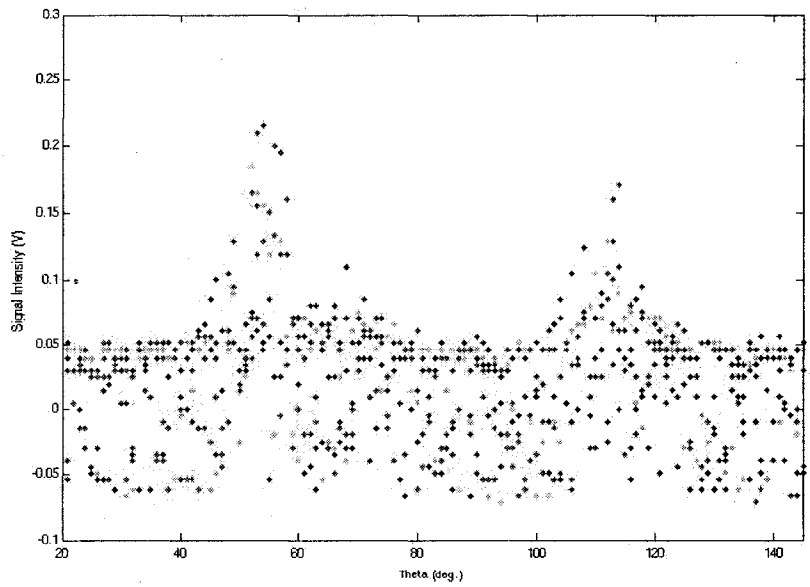

Figure 5-13: SPCE scan of Si/Ag/SiO(x) (10% Oxygen) with PMT Voltages: 0.75 V (black), 0.77 V (green), 0.79 V (magenta), 0.82 V (light blue), 0.84 V (blue), and 0.84 V (red).

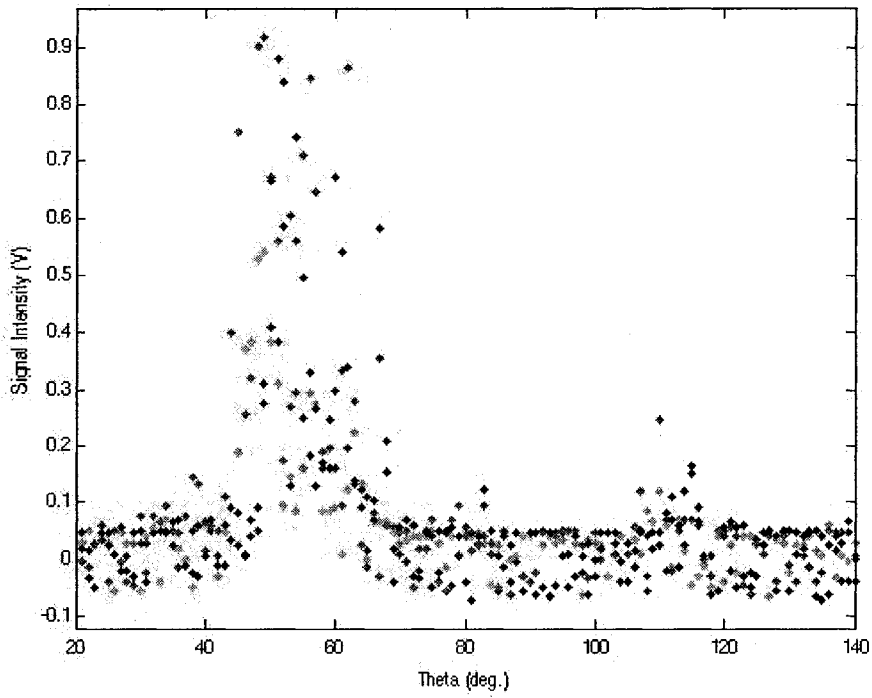

Figure 5-14: SPCE scans of thicker passivation layer Si/Ag/SiO(x) (5% Oxygen) samples with PMT voltages 0.75 V (green), 0.77 V (blue), 0.84 V (red) and 0.84 V (black).

Table 5.8: SPCE angles for Si/Ag/SiO(x) (20 nm passivation layer)

Run Number	θ_{SPCE}	θ_{SPCE}
Figure 5.9 0.75 V	48.5 ± 0.5	109.4 ± 1.0
Figure 5.9 0.77 V	52.2 ± 0.4	116.9 ± 4.7
Figure 5.9 0.84 V	51.7 ± 1.4	110.5 ± 3.5
Figure 5.9 0.84 V	54.8 ± 1.4	113.7 ± 1.0

Chapter 6

Discussion

Measurement of SPCE signal is possible using the apparatus built. However, the qualities of scans which would make these measurements useful (location and intensity) have highly variable values. Upon reviewing the several material sets, the change in peak height is obvious. Upon reviewing the curves fitted to the data, the shift in peak locations becomes apparent. Peak locations are reproducible for scans with step sizes above 0.5°, and irreproducible below 0.5°. The variance in peak location and peak intensity can be explained by considering factors from: how the stepper motor operates, the alignment of the prism and laser and the sensitivity of fluorescence to its environment.

6.1 Angular Reproducibility

The series of 20 runs done on April 16, 2007 provides the best insight of angular reproducibility for scans with step sizes of 0.5° and 1.0°. These scans were all done in quick succession and the sample was not disturbed between runs. The average first SPCE peak, measured with a 1.0° step size, was located at $58.4° \pm 3.0°$. Large deviations were due to small peaks which were poorly distinguished from the background noise and could not be accurately fit by MatLab. Omitting those fits with an relative uncertainty > 20% shifts the first peak location to $56.7° \pm 1.4°$. The average of the second SPCE peak fits was located at $122.8° \pm 0.4°$. Omitting the fit with a relative uncertainty >20% does not affect the location

or uncertainty of this fit. The average peak locations from scans made with 0.5° step sizes are 61.2° ± 4.9° for the first peak and 122.6° ± 0.5° for the second. Omission of fits with a relative uncertainty >20% shifts the location of the first peak to 59.2° ± 3.1°.

The scans made with 0.5° step size show a drift in the SPCE angle for angles below 90°. If all measurements are used, the difference between the θ_{SPCE} values measured with 1.0° step size and 0.5° step size is 2.8°. Omitting those fits with a relative uncertainty greater than 20% results in a difference of 2.5°. Both differences fall within the range of uncertainty for the calculated angle.

However, it can be seen in Figures 5-7 and 5-8 that at smaller step sizes (< 0.25°), the differences in SPCE angles become more pronounced. The scans made on May 23, 2007 were repeated scans made of a sample of AlSi/Ag/AlSI-N (15% Nitrogen) with step sizes of 1.0°, 0.75°, 0.5°, 0.25°, 0.2°, 0.15°, and 0.1°. For the smaller step sizes only one SPCE peak was measured, the length of the scan did not extend to 180°. SPCE angles for these runs varied from 50.5° to 61.5°. Small step sizes were also used in reversed directional scans. These scans were made with a sample of Si/Ag/SiO(x) (5% Oxygen). The difference between clockwise and counterclockwise scans is given in Table 6.1. The range of values cannot be due to poor curve fitting: the peaks of these runs are distinguishable from the background noise of the detector.

Sources of these angular drifts can be due to poor fitting or could have mechanical sources. Only one set of scans was done with step sizes below 0.25°. Repeated scans could show fluctuations in the SPCE angles that mediate the large range of values. A more probable source for these differences is mechanical. According to the manufacturer (Zaber), the stepper being used has a minimum step resolution of 0.0281°. This is not attainable for SPCE scans, the weight of the detector and optics creates additional load and torque

Table 6.1: Difference between SPCE angles of CW and CCW scans

Step Size	CW	CCW	Difference
0.5°	65.3 ± 0.1	46.8 ± 0.1	18.5 ± 0.5
0.25°	62.6 ± 0.1	51.9 ± 0.1	10.7 ± 0.5
0.2°	56.1 ± 0.1	48.2 ± 0.1	7.9 ± 0.5
0.1°	48.3 ± 0.1	43.8 ± 0.1	4.5 ± 0.5

which deteriorate the minimum step resolution. Additionally, the length of the detector arm and the width of the aperture limits the angular resolution to 0.1°. To improve the stepper resolution, the speed at which the motor rotates must be decreased. This can be done using the software supplied by Zaber.

Stepper motors are listed with information about 'accuracy' and 'repeatability'. These define the deviation in the position of the load when the motor is repeatedly instructed to move to a position. The manufacturer of the motor lists the accuracy of the motor as $< 1°$, and lists the repeatability of the motor as $< 0.1°$. Repeated commands to the motor to move to a target position would vary by less than 0.1°.

6.2 Intensity Variance

The most striking example of variance in the signal intensity is seen in the Si/Ag/SiO(x) (5% Oxygen) samples. The first slide showed a strong signal that was visible with the naked eye. The measured peak height was nearly 2.5 V, the strongest signal ever recorded in these trials (Figure 5-11). The verification of the signal strength by physical observation, confirms that this result is not due to a malfunction of the detector or the detection of scattered

light. However, subsequent samples have failed to replicate this result. The variability of fluorescence and the thickness of the dye layer are probable sources of variance in peak height, and thus signal intensity.

The fluorescent dye was prepared in 5mL batches and stored at -20°C while awaiting coating. One batch of dye is enough to coat 2 slides and slides are coated individually. The use of different dye batches and separate coating runs for different slides introduces variance in the qualities of the dye layer. The intensity of fluorescence can be affected by many factors, for example: pH of the buffer solution, dye concentration, oxygen in the solution and other quenchers.

The rhodamine dye was dissolved in a buffer solution of pH 8.0 to create a concentrated stock solution. This stock solution was stored at -20°C and 0.5 mL of this solution was used to make each batch of dye. The pH of the solution was not tested before each dye batch was prepared. The stock solution was kept isolated in a closed container and contamination was unlikely. The PVA solution was also prepared in small volumes (15 mL), with new solution prepared for each dye batch.

Coating the slides was done with a spin coater. The spin speed during the coating stayed close to the target velocity. However, the lack of markings on the coater meant that the same target velocity was not used in different sessions. Early slides were coated at 2500 rpm. Later slides were coated at 2200 rpm and the last slides were coated at 3000 rpm. The variance in spin speed would affect the thickness of the dye layer; lower speed would create thicker layers. In the 2004 study by Gryczynski et al., it was shown that a change in film thickness by 15nm would affect the location of the SPCE angle and also decrease the efficiency of dye/plasmon coupling.

A markedly thicker dye layer could also create an inner-filter effect, which would decrease

the fluorescence intensity. This effect occurs in samples that are highly absorbent and thick. If light at the peak wavelength of the dye is incident on one surface of the layer, it will be absorbed by the surface molecules. Fluorescence will be emitted into the dye layer at a longer wavelength. This longer wavelength light will be incident on the lower surface of the layer. However, the change in wavelength has shifted the light away from the peak wavelength of the dye. This longer wavelength will be weakly absorbed and less intense fluorescence will result.

Quenching is the most likely cause of intensity variance. Fluorescent dyes can be quenched by collisional or static quenching. Collisional quenching occurs when an excited fluorescent molecule collides with another molecule or atom. Instead of transferring energy to a photon and creating fluorescence, the energy will be lost to the collision. Oxygen dissolved in the solution will quench any fluorescent molecule. The PVA solution and dye solutions were not degassed after preparation, there is oxygen present in these solutions.

Silver is also a known quencher of fluorescence. Reviewing the different samples used for SPCE testing, and comparing their peak variances shows that the silicon based samples have a higher variance in signal intensity. The signals for these samples are as low as the background noise (< 0.1 V) and nearly as high as 3 V. For the AlSi based samples, the signal intensity ranged from tenths of volts to nearly 1 V. Previous studies by members of the Harper lab group have focused on silicon-silver mixtures. It has been observed that silver will migrate through silicon films and form small islands on the silicon surface. It has not yet been determined how the addition of oxygen to silicon will affect this silver migration.

6.3 Symmetry of Angular Emission

The theory of SPCE, and the results of Gryczynski et al show that the locations of SPCE peaks should be symmetric with respect to the normal direction (90°). Also, the emission into one peak should not be preferred over the other. However, the scans shown in the previous section and given in the Appendix are asymmetrical, both in peak height and location. The early repeated runs on April 16th verified that the angular positions of SPCE angles are reproducible. Focus then turned to the alignment of the sample surface and the laser and how this affects the symmetry of SPCE.

In Figure 5-5, the higher peak occurs at an angle above 90°. However, in Figure 5-11, the higher peak occurs at an angle below 90°. Likewise, throughout all the scans listed in the Appendix, there is a variance in which peak (above or below 90°) is most intense. This is indicative of the lack of accurate repositioning of samples on the laser arm. Normal incidence of the laser can be reproduced by observing that the laser light is reflected back to the laser. However, slight shifts in the prism position may affect how the filter is aligned with the emitted light. If the filter is slightly misaligned, not exactly normal to the emitted light, then green light may reach the detector. This would not damage the detector, but the added intensity of the green laser would skew the signal intensity.

6.4 Width of SPCE Peak

SPCE is promoted as highly localized emission. Yet the signals measured are not sharp peaks, but rather wide peaks. The broadness of the peaks is due to the fluorescence spectrum of a dye. When a molecule fluoresces, the excited molecule does not decay to the same energy state in every transition. Thus, a range of wavelengths are emitted. There is one preferred

transition above all and this is the angle that the most light will be emitted at. SPCE is wavelength dependent: the wavelength of the plasmon oscillations will determine the angle of emission. The broad range of fluorescent emission wavelengths will result in a range of angles of emission.

6.5 Detector Noise

The amount of noise generated by the detector has made peak-fitting difficult. Smaller SPCE peaks are often lost or indistinguishable from the background noise. This noise can be removed by the addition of electronics at the DAQ, to act as a filter.

6.6 Comparison to Literature Value

The SPCE emission observed by Gryczynski[1] showed sharp distributions of fluorescence at angles of $\pm 47°$ and $\pm 50°$. The angle of emission differed because of the different fluorescent dye layer thicknesses, 15 or 30 nm. The thicker film (30 nm) corresponds to the emission angle of $\pm 50°$ and the thinner (15 nm) film corresponds to the emission angle of $\pm 47°$. These angles were measured with respect to the normal direction. Translating these into the measurement system used in this thesis transforms the angle $\pm 50°$ into $\pm 40°$ and the angle $\pm 47°$ into $\pm 43°$. Comparison between the Gryczynski values and the values measured in this thesis are difficult to make. First, the SPCE angles measured in the trials described here do not show such even distributions with respect to the normal direction. This may be due to misalignment of the prism and detector. Second, the asymmetry of the SPCE peaks makes one peak much harder to fit, due to the difficulty in distinguishing it from the background noise. To determine the SPCE angle, an assumption was made. The theory of

SPCE predicts that the angular fluorescence pattern will be determined by the wavelength of light emitted by the fluorescent molecules. Any slight deviation in the incident light angle, away from normal incidence, should not affect the emission since this light is not measured by the detector. If the prism is slightly misaligned, the absolute angular position of the peaks would be misaligned, but the separation between the two peaks should remain invariant. Using this, the angle separating the two SPCE peaks was found, then halved to give the value for the SPCE angle.

$$\theta_{SPCE} = \pm\frac{|\theta_2 - \theta_1|}{2} \tag{6.1}$$

Where, θ_2 is the location of the SPCE peak above 90° and θ_1 is the location of the SPCE peak below 90°.

Working from the series of repeated runs for each material set, the SPCE angles can be roughly approximated. For the AlSi/Ag/AlSi-N (15% Nitrogen, 34.1 nm Ag) series, the SPCE angle was ±33°. For the Si/Ag/SiO(x) (5 % Oxygen) series, the SPCE angle was ±34°. For the Si/Ag/SiO(x) (10 % Oxygen) series, the SPCE angle was ±29°. For the Si/Ag/SiO(x) (5% Oxygen, 20 nm passivation layer) series, the SPCE angle was ±31°.

The SPCE angle values measured in this thesis show a much narrower angular pattern, compared to the Gryczynski studies. As discussed in Chapter 3, SPCE is closely related to SPR. It was seen that there are many factors which affect the SPR angle, and likewise can affect the SPCE angle. Working from the parameters discussed in Chapter 3; silver film thickness, dielectric layer thickness and also excitation wavelength can affect the SPCE angle.

The silver films in this study were all 50 nm thick, except for the series with 34.1 nm. It can be inferred from Figure 3-5, that a slight variation in the silver film thickness would not alter the position of the SPCE angle. It would predominately affect the amount of

energy transferred to the surface plasmons and affect the coupling of fluorescent molecules and surface plasmons.

The dye used in the Gryczynski study was Sulforhodamine 101 which has an emission peak near 600 nm. The dye used in this thesis was Rhodamine Red which has an emission peak near 600 nm and also a secondary peak near 650 nm. The secondary peak corresponds to red light, while the primary peak corresponds to yellow light. The longer wavelength emission will appear at SPCE angles closer to normal, while the shorter wavelengths will appear further from normal.

The fluorescent dye thicknesses in the Gryczynski studied were either 15 nm or 30 nm. The thickness was varied by using dye mixtures of different concentration. The thickness was determined by the optical densities of the dyes. Attempts were made to keep the thickness of the fluorescent dye layer in this thesis work consistent. However, the layers of different samples were likely different thicknesses, due to the variance in spin speeds (from 2200–3300 rpm).

6.7 Conclusions and Future Work

This thesis work has produced the elements needed to generate and measure SPCE at the University of New Hampshire. Film stacks deposited from two magnetron targets have been shown to generate SPCE and initial studies indicate that the materials used for adhesion and passivation layers may have an effect on the intensity of the signal. Collaborations with members of the Biochemistry department have resulted in methods to prepare concentrated fluorescent dyes. A compact, automated apparatus has been designed and built which can detect a SPCE signal quickly and precisely. There are some limitations to the apparatus and methods which need to be addressed, however, the are many new avenues of research

which are now accessible.

The methods described in this thesis have limitations caused by the lack of consistency in some results. The variance in fluorescence intensity is the largest obstacle facing SPCE testing at the University of New Hampshire. Samples of identical composition, and coated with the same dye, generated fluorescent signals of different intensities. Applications of SPCE in ultrasensitive immunoassays rely on detecting the change in fluorescence intensity to detect molecules[22]. Improvements must be made in the preparation of the fluorescent dye to ensure that the dye has more consistent qualities. Larger batches of dye should be prepared or multiple slides should be coated with the same dye batch. Improvements must also be made to ensure exact repositioning of the prism and sample. An independent mount must be made or methods of calibration must be developed. The angular resolution and the detector noise are remaining areas of improvement. Finer step sizes ($< 0.5°$) need to be used with more reproducible results. The level of noise from the detector must be decreased in order to study materials with weak SPCE signals.

Even with the current limitations of the apparatus, it already presents new opportunities for research in material science. Different film stack compositions can be deposited and tested for dye-plasmon coupling by studying the strength of SPCE signal. The co-deposited silver-silicon films described in Chapter 4 have not been measured yet, but present an opportunity to study how the loss of silver film uniformity affects SPCE generation. The use of two-source deposition as a viable method of SPCE sample production has been established. This can be used as a means to study new film stacks for SPCE, creating films that are more resistant to corrosion.

Biochemical applications will require modifications to the coating of film stacks. The concentrated dye used to initially detect SPCE will be replaced by solutions of labeled

antibodies or biological agents. Additionally, the method of spin-coating (while useful for creating uniform films of robust solutions) may need to be replaced by other methods of dye application.

List of References

[1] Gryczynski, I., Malicka, J., Gryczynski, Z., and Lakowicz, J. R. Radiative decay engineering 4. Experimental studies of surface plasmon-coupled emission. *Analytical Biochemistry* **324**, 170–182 (2004).

[2] Lakowicz, J. R. Radiative decay engineering 3. Surface plasmon-coupled directional emission. *Analytical Biochemistry* **324**, 153–169 (2004).

[3] Gryczynski, I., Malicka, J., Gryczynski, Z., and Lakowicz, J. R. Ultraviolet Surface Plasmon-Coupled Emission Using Thin Aluminum Films. *Analytical Chemistry* **76**, 4076–4081 (2004).

[4] Gryczynski, I., Malicka, J., Gryczynski, Z., and Lakowicz, J. R. Surface Plasmon-Coupled Emission with Gold Films. *J. Phys. Chem. B* **108**, 12568–12574 (2004).

[5] Sommerfeld, A. *Partial Differential Equations in Physics* (Academic Press, New York, 1949).

[6] Chance, R. R., Prock, A. , and Sibley, R. *Molecular Fluorescence and Energy Transfer Near Interfaces* (Advances in Chemical Physics, 37, Wiley,New York 1978).

[7] Jackson, J. D. *Classical Electrodynamics* (Wiley, New York, 1999).

[8] Kuhn, H. Classical Aspects of Energy Transfer in Molecular Systems. *Journal of Chemical Physics* 101– 108 (1969).

[9] Drexhage, K. H. *Interaction of Light with Monomolecular Dye Layers* (Progress in Optics, 12, North-Holland, New York. 1974).

[10] Morawitz, H. Self-Coupling of a Two-Level System by a Mirror. *Physical Review* 1792–1796 (1969).

[11] Tai, Chen-To *Dyadic Green's Functions in Electromagnetic Theory* (Intext Educational, London, 1971).

[12] Lakowicz, J. R. Radiative Decay Engineering: Biophysical and Biomedical Applications. *Analytical Biochemistry* **298**, 1–24 (2001).

[13] Lakowicz, J. R., Geddes, C. D., Gryczynski, I.,Malicka, J., Gryczynski, Z., Aslan, K., Lukomska, K., Matveeva, E., Zhang, J., Badugu, R. and Huang, J. Advances in Surface-Enhanced Fluorescence. *Journal of Fluorescence* **14**, 425–441 (2004).

[14] Raether, H. Surface Plasma Oscillations and Their Applications. *Physics of Thin Films* **9**, 145–261 (1977).

[15] Raether, H. *Excitation of Plasmons and Interband Transitions by Electrons* (Springer–Verlag, Berlin, 1980).

[16] Raether, H. *Surface Plasmons on Smooth and Rough Surfaces and on Gratings* (Springer–Verlag, Berlin, 1988).

[17] Ritchie, R. H, Surface Plasmons in Solids. *Surface Science* (1973).

[18] Pines, D. *Elementary Excitations in Solids* (W. A. Benjamin, New York, 1963).

[19] Nelson, B. P., Frutos, A. G., Brockman, J. M. and Corn, R. M. Near-Infrared Surface Plasmon Resonance Measurements of Ultrathin Films. 1. Angle Shift and SPR Imaging Experiments. *Anal. Chem.* **71**, 3928–3934 (1999).

[20] Hanken, D. G., Jordan, C. E., Frey, B. L. and Corn, R. M. *Surface Plasmon Resonance Measurements of Ultrathin Organic Films at Electrode Surfaces* (Electroanalytical Chemistry, 20, Dekker, New York 1998).

[21] Kurihara, K.,Suzuki, K. Theoretical Understanding of an Absorption-Based Surface Plasmon Resonance Sensor Based on Kretchmann's Theory *Analytical Chemistry* **74**, 696–701 (2002).

[22] Lakowicz, J. R., Malicka, J., Matveeva, E., Gryczynski, I., and Gryczynski, Z. Plasmonic Technology: Novel Approach to Ultrasensitive Immunoassays. *Clinical Chemistry* **51**, 1914–1922 (2005).

[23] Borejdo, J., Gryczyjski, Z., Calander, N., Muthu, P., and Gryczynski, I. Applications of Surface Plasmon Coupled Emission to Study of Muscle. *Biophysical Journal* **91**, 2626–2635 (2006).

[24] Malicka, J., Gryczyjski, I., Gryczynski, I., and Lakowicz, J. R. DNA Hybridization Using Surface Plasmon-Coupled Emission. *Analytical Chemistry* **75**, 6629–6633 (2003).

[25] Gannattasio, A., Hooper, I. R., and Barnes, W. L. Transmission of light through thin silver films via surface plasmon-polaritons. *Optics Express* **12**, 5881–5886 (2004).

[26] Barnes, J. R. Fluorescence near interfaces: the role of photonic mode density. *J. Mod. Optics* **45**, 661–699 (1998).

[27] Ford, G. W., Weber, W. H., Electromagnetic Interactions of Molecules with Metal Surfaces. *Physics Reports* **113**, 195–287 (1984).

[28] Chance, R. R., Prock, A. , and Sibley, R. Lifetime of an excited molecule near a metal mirror: Energy transfer in the Eu^{3+}/silver system. *Journal of Chemical Physics* **60**, 2184–2185 (1974).

[29] Chance, R. R., Prock, A. , and Sibley, R. Lifetime of an emitting molecule near a partially reflecting surface. *Journal of Chemical Physics* **60**, 2184–2185 (1974).

[30] Chance, R. R., Prock, A. , and Sibley, R. Frequency shifts of an electric-dipole transition near a partially reflecting surface. *Phys. Rev. A* 1448–1452 (1975).

[31] Chance, R. R., Prock, A. , and Sibley, R. Comments on the classical theory of energy transfer. *Journal of Chemical Physics* **62**, 2245–2253 (1975).

[32] Chance, R. R., Prock, A. , and Sibley, R. Comments on the classical theory of energy transfer. II. Extension to higher multipoles and anisotropic media. *Journal of Chemical Physics* **65**, 2527–2531 (1976).

[33] Winter, G. Emission of light through thin silver films via near-field coupling to surface plasmon polaritons. *Applied Physics Letters.* 1–3 (2006).

[34] Lakowicz, J. R. *Principles of Fluorescence Spectroscopy* (Kluwer Academic, Boston, MA, 1999).

[35] Zangwill, A. *Physics at Surfaces* (Cambridge University Press, Cambridge, MA, 1988).

[36] Born, Max, and Wolf, Emil *Principles of Optics* (Pergamon, New York, 1980).

[37] de Bruijn, H. E.,Altenburg, B.,Kooyman, R., and Greve, J. Determination of thickness and dielectric constant of thin transparent dielectric layers using Surface Plasmon Resonance. *Optics Communications.* 425–432 (1991).

[38] de Bruijn, H. E.,Minor, M.,Kooyman, R., and Greve, J. Thickness and dielectric constant determination of thin dielectric layers. *Optics Communications.* 183–188 (1993).

[39] Banos, A. *Dipole Radiation in the Presence of a Conducting Half-Space* (Pergamon Press, New York. 1966).

[40] Corn, R., http://unicorn.ps.uci.edu/calculations/fresnel/fcform.html accessed: May, 2007

Appendices

Appendix A

LabVIEW

The operation of the apparatus was dependent on three areas: the control of the stepper motor, the operation of the laser and the operation of the PMT. These components were synchronized and controlled by LabVIEW programs. Two separate programs were used, one to conduct a singe scan in the clockwise direction, and one to conduct a pair of scans in the clockwise then counter-clockwise direction. These two programs relied on the same basic structure, which consisted of four sequences. These sequences will be shown and discussed.

A LabVIEW program has two main windows: the Front Panel (Figure A-1), and the Block Diagram. The Front Panel is the user interface, the Block Diagram contains all the programming. It is important to remember that LabVIEW is a graphical programming language, and relies on horizontal programming structure. Programs and routines are called in the order they appear, moving from left to right.

The first sequence (Figure A-2) defines the operating voltage of the PMT. It utilizes the library of sequences (A_Out.vi) from Measurement Computing, the manufacturer of the DAQ. The user specifies the voltage to be outputted by the DAQ. Taking into account the electronic circuit The sequence is nested in a While-loop, it exits the loop when the condition 'go home' is set to True. This occurs when the 'go home' button is activated on the front panel (Figure A-1).

After the user sends the command 'go home' to the LabVIEW program, the program

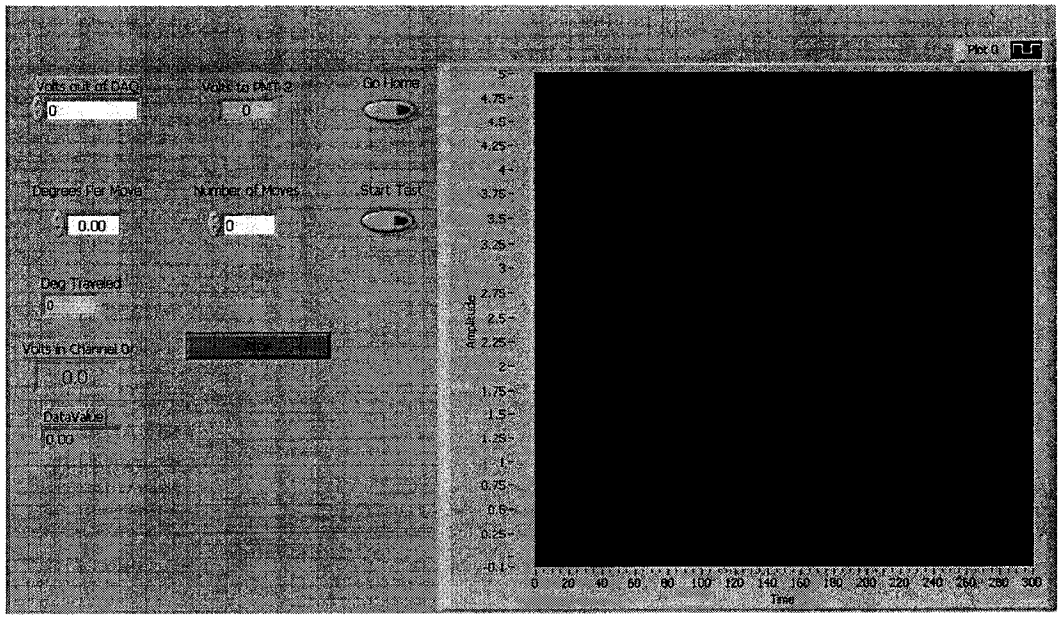

Figure A-1: The Front Panel, the user interface of a LabVIEW program

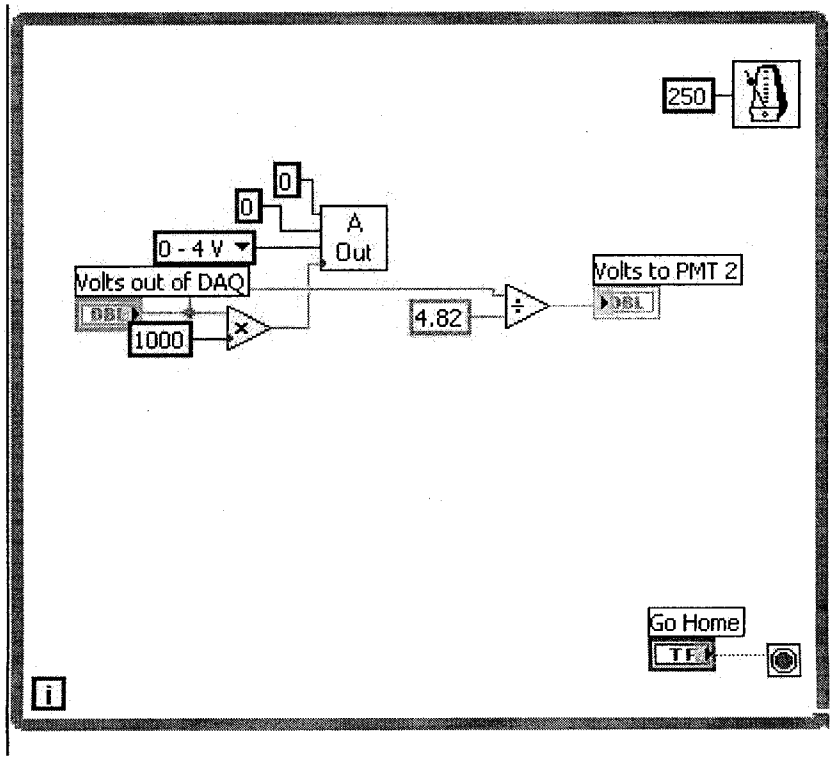

Figure A-2: First sequence in the basic LabVIEW program

exits the first sequence and proceeds to the second (Figure A-3). This is a single iteration loop which sends the command 'go home' to the stepper motor. This is Zaber command #1 and is sent using 'Zaber write'. The .vi 'Zaber write' has four connections: a data value, the command number, the unit number and a VISA reference. VISA is an input/output programming language used to communicate with instruments. Here, it is used to send commands to the stepper motor. It references a COM number which is assigned to the stepper motor when it is first connected to the computer. The command number is command #1 and the unit number is #1. The data value is ignored when calling command #1, however, leaving this connection unwired results in a programming error. A dummy data value is sent to this connection.

Before the program can begin a scan, stepping and reading the light signal, the motor must be in its home position. This is vital to ensure that all scans begin at the same position, 0°. The third sequence of the program (Figure A-4) will continuously measure the position of the motor. The home position of the motor is programmed with a data value '1'.

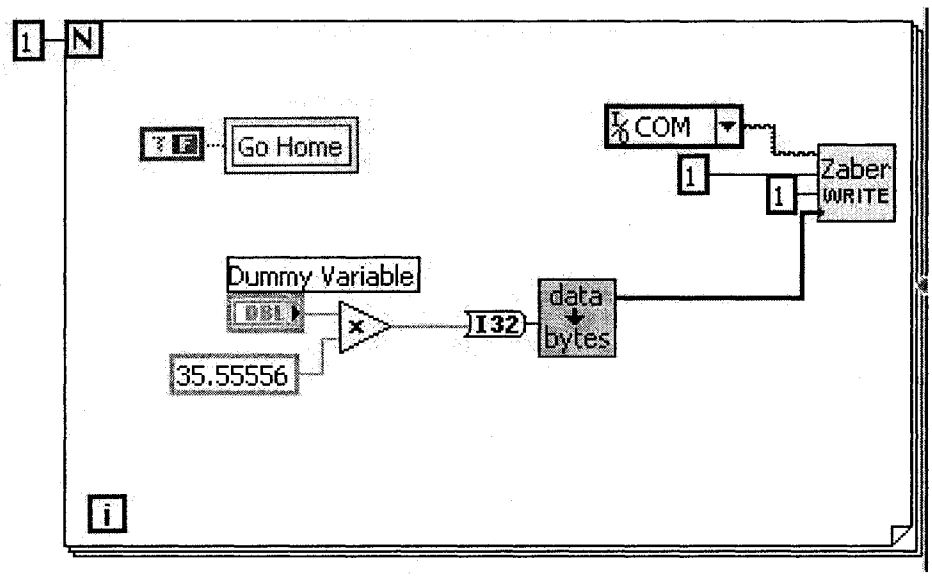

Figure A-3: Second sequence in the basic LabVIEW program

The third sequence, nested in a While-loop, will input the data value of the motor position. When the value is equal to 1, then the loop is exited.

The final sequence of the program is a pair of loops which will advance the motor and read the signal from the PMT. On the Front Panel, the user specifies a step size and a total number of steps. The value entered for the number of steps is read by the program and then doubled. This new value is used as the maximum number of iterations for a For-loop. Nested inside this For-loop is a pair of loops, one to advance the motor and one to read the PMT signal. On even-numbered iterations, the signal from the PMT is read. On odd-numbered iterations, the stepper motor advances. A timer in the main For-loop determines how long the program waits between iterations. This determines the collection time for the PMT.

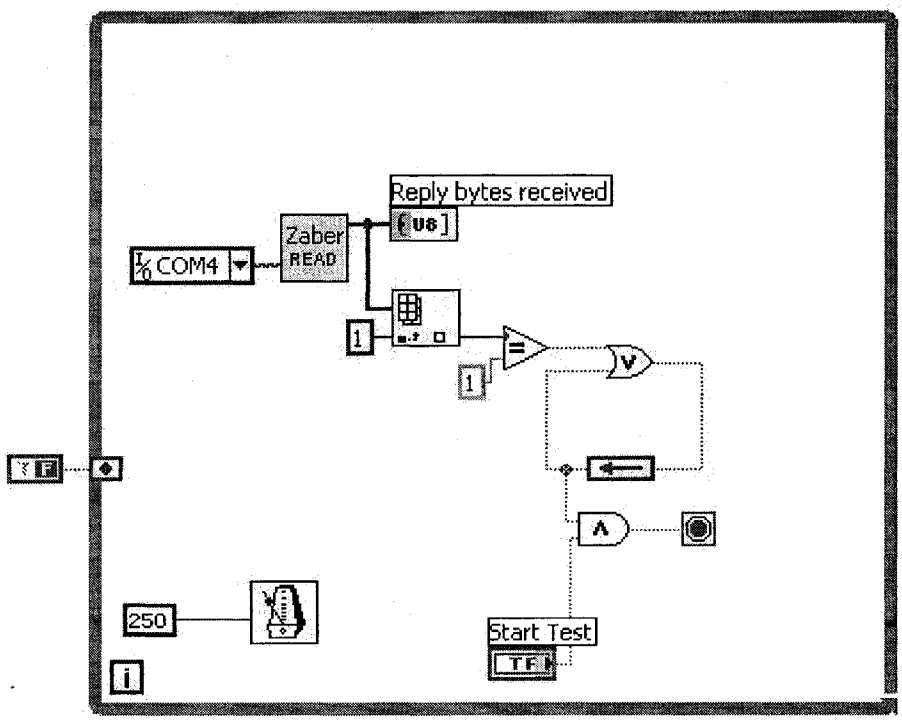

Figure A-4: Third sequence in the basic LabVIEW program

The signal is read with the loop shown in Figure A-5. The signal from the DAQ is read with the subroutine AIn.vi, which reads a specified channel (#0) from a specified board (#0). The output is converted into voltage units with the subroutine ToEng.vi. Both of

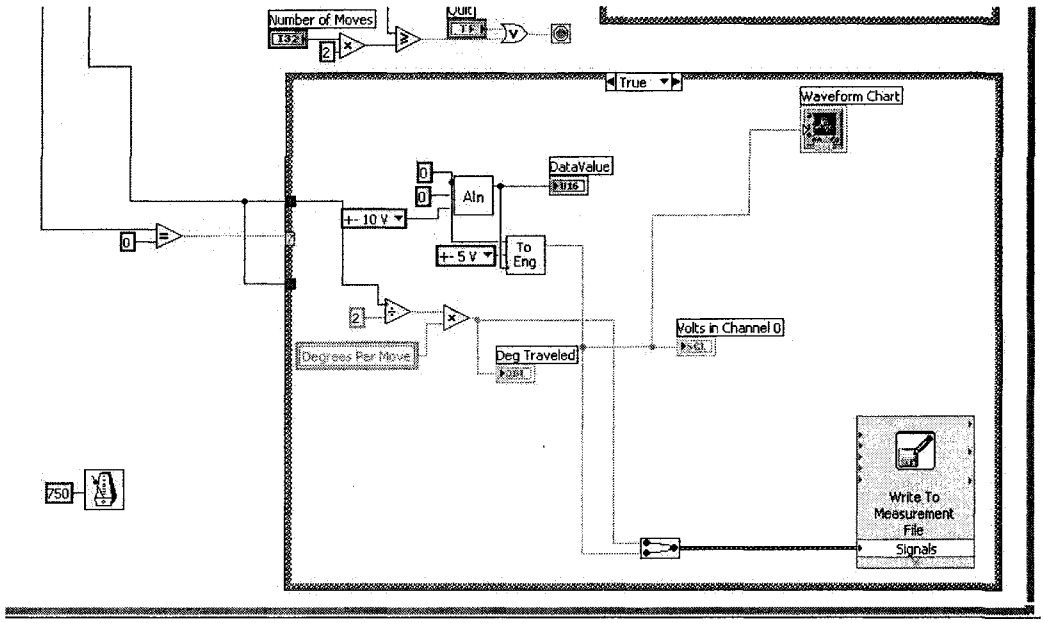

Figure A-5: Fourth sequence, even iterations read PMT signal

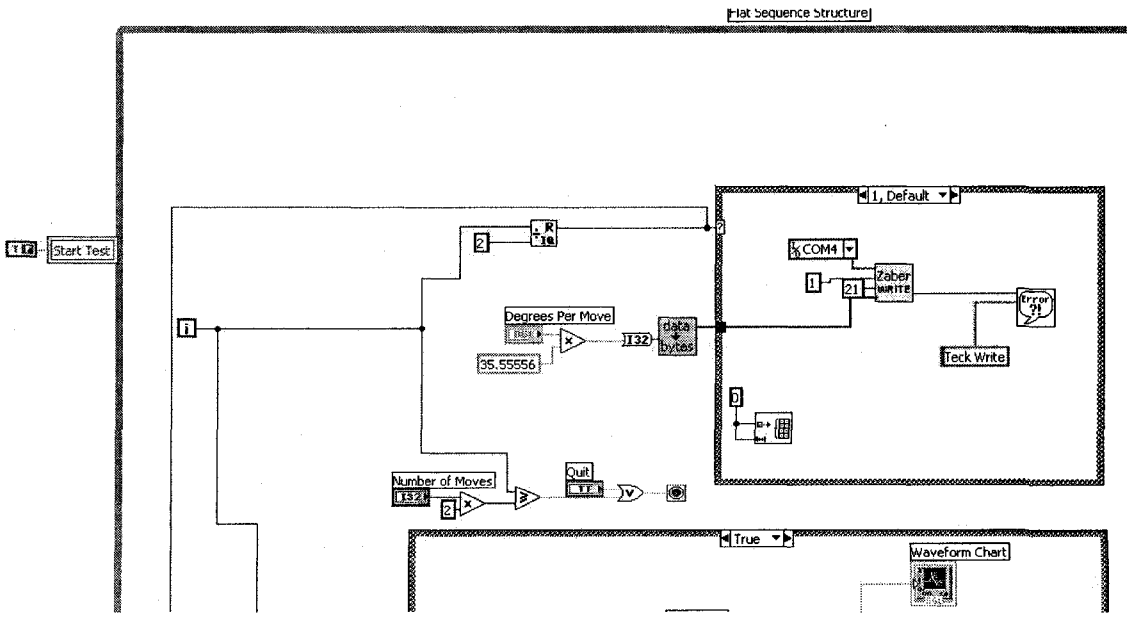

Figure A-6: Fourth sequence, odd iterations advance stepper motor

these were written and supplied by Measurement Computing. It is in this loop that the data is written to a data file (by the LabVIEW subroutine 'Write to Measurement File') and also displayed in a graph on the Front Panel (by the LabVIEW subroutine 'Waveform Chart').

The stepper motor is advanced with the loop shown in Figure A-6. The step size specified by the user is converted to a data value which is sent to the motor, using ZaberWrite.vi. The command 'move relative' is sent to the motor (command #21). This command makes the motor move a specified distance relative to its current position.

Appendix B

Summary of SPCE Angles

The data contained in this Appendix are the complete listing of all measured SPCE angles. The data generated in LabVIEW was imported to Matlab and fitted with Gaussian curves of the form,

$$G(x) = A_1 e^{-(\frac{(x-b_1)}{c_1})^2} \tag{B.1}$$

The location of the peak, b_1 is interpreted as the SPCE angle and listed as "Peak 1" or "Peak 2". The uncertainties associated with these values were generated by the curve fitting program and are listed as " Peak 1 uncer. " or "Peak 2 uncer. ".

In addition, there are value for "delta theta" which refers to the difference between θ_{SPCE} values, outlined in Chapter 6. The uncertainty in this value was found by error propagation methods.

Run Number	Time	Material Set	PMT Voltage	Peak1	Peak1 uncer.	Peak2	Peak2 uncer.	Step Size	delta (theta)	Delta Uncer
13 (5/1)	2:03 PM	AlSi/AlSi-N	0.75V	50.75	1.01	108	1.8	1	57.25	2.06
14 (5/1)	2:08 PM	AlSi/AlSi-N	0.77V	53.56	1.06	113.4	1.8	1	59.84	2.09
15 (5/1)	2:14 PM	AlSi/AlSi-N	0.79V	48.27	0.77	106.2	1.9	1	57.93	2.05
16 (5/1)	2:19 PM	AlSi/AlSi-N	0.82V	54.42	0.45	114.1	1.1	1	59.7	1.19
17 (5/1)	2:24 PM	AlSi/AlSi-N	0.84V	50.02	0.27	111.9	0.9	1	61.9	0.94
18 (5/1)	2:30 PM	AlSi/AlSi-N	0.84V	54.25	0.33	117.5	1.7	1	63.3	1.73
B1 (5/25)	11:21 AM	AlSi/AlSi-N	0.84V	67.3	0.1	135.9	0.3	1	68.6	0.32
B2 (5/25)	11:30 AM	AlSi/AlSi-N	0.84V	67.6	0.2	135.9	0.1	1	68.3	0.2236
B3 (5/25)	11:46 AM	AlSi/AlSi-N	0.84V	46.8	0.1	n/a	n/a	0.5		
B4 peak1 (5/25)	12:07 PM	AlSi/AlSi-N	0.84V	51.9	0.1	n/a	n/a	0.25		
B5 peak1 (5/25)	12:37 PM	AlSi/AlSi-N	0.84V	48.2	0.1	n/a	n/a	0.2		
B6 peak1 (5/25)	1:32 PM	AlSi/AlSi-N	0.84V	43.8	0.1	n/a	n/a	0.1		
F1 peak1 (5/25)	11:16 AM	AlSi/AlSi-N	0.84V	68.2	0.3	136	0.3	1	67.8	0.42
F2 peak1 (5/25)	11:26 AM	AlSi/AlSi-N	0.84V	68.5	0.1	135.9	0.2	1	67.4	0.22
F3 peak1 (5/25)	11:41 AM	AlSi/AlSi-N	0.84V	65.3	0.1	n/a	n/a	0.5		
F4 peak1 (5/25)	11:56 AM	AlSi/AlSi-N	0.84V	62.6	0.1	n/a	n/a	0.25		
F5 peak1 (5/25)	12:23 PM	AlSi/AlSi-N	0.84V	56.1	0.1	n/a	n/a	0.2		
F6 peak1 (5/25)	1:07 PM	AlSi/AlSi-N	0.84V	48.3	0.1	n/a	n/a	0.1		
19 peak2 (5/1)	3:12 PM	Si/SiO 10%	0.75V	109.4	1.8	n/a	n/a	1		
20 peak1 (5/1)	3:17 PM	Si/SiO 10%	0.77V	69.91	23.5	116.6	7.4	1	46.7	24.64
21 peak1 (5/1)	3:22 PM	Si/SiO 10%	0.79V	78.53	32.8	113.4	3.5	1	34.9	32.99
22 peak1 (5/1)	3:27 PM	Si/SiO 10%	0.82V	44.74	1.46	118.5	13.8	1	73.8	13.88
23 peak1 (5/1)	3:32 PM	Si/SiO 10%	0.84V	67.9	23.2	107.7	5.3	1	39.8	23.80
24 peak1 (5/1)	3:56 PM	Si/SiO 10%	0.84V	55	0.8	112.6	1	1	57.6	1.28
25 peak1 (5/1)	4:03 PM	Si/SiO 10%	0.75V	47.4	2.2	105.3	5.4	1	57.9	5.83
26 peak1 (5/1)	4:08 PM	Si/SiO 10%	0.77V	61	6.1	111.8	5.2	1	50.8	8.02
27 peak1 (5/1)	4:13 PM	Si/SiO 10%	0.79V	54.8	2.1	115.9	5	1	61.1	5.42
28 peak1 (5/1)	4:18 PM	Si/SiO 10%	0.82V	53.3	0.7	112.9	2.3	1	59.6	2.40
29 peak1 (5/1)	4:23 PM	Si/SiO 10%	0.84V	55.2	1.3	115.1	2.1	1	59.9	2.47
30 peak1 (5/1)	4:37 PM	Si/SiO 10%	0.84V	55.1	0.7	119.4	7.1	1	64.3	7.13
35 peak1 (5/1)	5:50 PM	Si/SiO 5%T	0.75V	48.5	0.5	109.4	1	1	60.9	1.12

Run Number	Time	Material Set	PMT Voltage	Peak1	Peak1 uncer.	Peak2	Peak2 uncer.	Step Size	delta (theta)	Delta Uncer
36 peak1 (5/1)	5:55 PM	Si/SiO 5%T	0.77V	52.2	0.4	116.9	4.7	1	64.7	4.72
37 peak1 (5/1)	6:00 PM	Si/SiO 5%T	0.79V	47	0.4	109.4	1	1	62.4	1.08
38 peak1 (5/1)	6:05 PM	Si/SiO 5%T	0.82V	54.2	0.9	n/a	n/a	1		
39 peak1 (5/1)	6:10 PM	Si/SiO 5%T	0.84V	51.7	1.4	110.5	3.5	1	58.8	3.77
40 peak1 (5/1)	6:16 PM	Si/SiO 5%T	0.84V	54.8	1.4	113.7	1	1	58.9	1.72
41 peak1 (5/1)	6:26 PM	Si/SiO 5%T	0.75V	49.7	0.9	114.9	7.2	0.5	65.2	7.26
42 peak1 (5/1)	6:36 PM	Si/SiO 5%T	0.77V	48.4	0.4	115.6	8	0.5	67.2	8.01
43 peak1 (5/1)	6:45 PM	Si/SiO 5%T	0.79V	52.6	0.6	113.6	0.3	0.5	61	0.67
44 peak1 (5/1)	6:57 PM	Si/SiO 5%T	0.82V	52.9	0.3	115.9	1.2	0.5	63	1.24
45 peak1 (5/1)	7:07 PM	Si/SiO 5%T	0.84V	53.3	0.2	116.3	0.7	0.5	63	0.73
46 peak1 (5/1)	7:17 PM	Si/SiO 5%T	0.84V	47.6	0.2	110.5	0.4	0.5	62.9	0.45
1 peak1 (4/30)	3:09 PM	Si/SiO 5%	0.75V	66.7	1.5	123.7	0.4	1	57	1.55
2 peak1 (4/30)	3:25 PM	Si/SiO 5%	0.82V	61.5	1.2	120.3	0.5	1	58.8	1.30
3 peak1 (4/30)	3:31 PM	Si/SiO 5%	0.84V	54.4	9.7	122.3	1.5	1	67.9	9.82
5 peak 1 (4/30)	3:43 PM	Si/SiO 5%	0.75V	68.4	0.2	127.1	0.8	1	58.7	0.82
6 peak1 (4/30)	3:49 PM	Si/SiO 5%	0.77V	70.6	0.3	130.5	1.2	1	59.9	1.24
7 peak1 (4/30)	3:55 PM	Si/SiO 5%	0.79V	69.5	0.2	129.9	0.6	1	60.4	0.63
8 peak1 (4/30)	4:01 PM	Si/SiO 5%	0.82V	65.5	0.2	126.6	0.6	1	61.1	0.63
9 peak1 (4/30)	4:07 PM	Si/SiO 5%	0.84V	64.2	0.2	124.9	0.5	1	60.7	0.54
10 peak1 (4/30)	4:12 PM	Si/SiO 5%	0.84V	66.2	0.2	126.4	0.4	1	60.2	0.45
1001 peak1 (4/3(	6:18 PM	Si/SiO 5%	0.79V	45.4	0.6	105.5	0.2	1	60.1	0.63
13 peak1 (4/30)	4:44 PM	Si/SiO 5%	0.75V	60.4	0.9	123.2	2.3	1	62.8	2.47
18 peak1 (4/30)	5:51 PM	Si/SiO 5%	0.79V	51.8	0.3	n/a	n/a	1	-51.8	
19 peak1 (4/30)	5:57 PM	Si/SiO 5%	0.79V	54.9	0.1	108.1	0.3	1	53.2	0.32
20 peak1 (4/30)	6:05 PM	Si/SiO 5%	0.79V	53.7	0.8	109.8	0.1	1	56.1	0.81
21 peak1 (4/30)	6:11 PM	Si/SiO 5%	0.79V	49	2.6	108.7	0.2	1	59.7	2.61
bkup peak1 (4/3(	3:14 PM	Si/SiO 5%	0.77V	65.1	0.9	123.9	0.5	1	58.8	1.03
bkup_1 peak1 (4	3:20 PM	Si/SiO 5%	0.79V	66.1	2	124	0.3	1	57.9	2.02
22 peak1 (5/23)	5:41 PM	Si/SiO 5%	0.82V	50.5	0.1	n/a	n/a	0.1		
21 peak1 (5/23)	5:41 PM	Si/SiO 5%	0.82V	61.5	0.1	n/a	n/a	0.15		
19 peak1 (5/23)	5:02 PM	Si/SiO 5%	0.82V	57.9	0.1	n/a	n/a	0.2		

Run Number	Time	Material Set	PMT Voltage	Peak1	Peak1 uncer.	Peak2	Peak2 uncer.	Step Size	delta (theta)	Delta Uncer
18 peak1 (5/23)	4:49 PM	Si/SiO 5%	0.82V	56.4	0.1	123.8	0.2	0.25	67.4	0.22
17 peak1 (5/23)	4:27 PM	Si/SiO 5%	0.82V	56.2	0.2	123.7	0.2	0.5	67.5	0.28
16 peak1 (5/23)	4:17 PM	Si/SiO 5%	0.82V	56.1	0.1	123.4	0.2	0.75	67.3	0.22
15 peak1 (5/23)	4:09 PM	Si/SiO 5%	0.82V	54.3	0.3	122.1	0.3	1	67.8	0.42
01 peak (5/1)	10:32 AM	Si/SiO 5%	0.79V	47.4	0.3	107.5	0.3	1	60.1	0.42
02 peak1 (5/1)	10:42 AM	Si/SiO 5%	0.75V	49.1	0.3	109.3	0.3	0.5	60.2	0.42
06 peak1 (5/1)	11:14 AM	Si/SiO 5%	0.77V	54.9	0.2	115	0.3	0.5	60.1	0.36
07 peak1 (5/1)	11:30 AM	Si/SiO 5%	0.79V	53.4	0.1	113.4	0.3	0.5	60	0.32
08 peak1 (5/1)	11:44 AM	Si/SiO 5%	0.82V	48.9	0.1	109	0.3	0.5	60.1	0.32
09 peak1 (5/1)	11:58 AM	Si/SiO 5%	0.75V	45.5	0.2	105.8	0.5	0.5	60.3	0.54
11 peak1 (5/1)	12:11 PM	Si/SiO 5%	0.77V	46.1	0.3	106.1	0.4	0.5	60	0.50
12 peak1 (5/1)	1:49 PM	Si/SiO 5%	0.75V	56.5	0.2	115.6	2	1	59.1	2.01
1 peak1 (4/16)	12:01 PM	AlSi/AlSi-N	0.84V	57.8	0.6	122.8	0.3	1	65	0.67
2 peak1 (4/16)	12:07 PM	AlSi/AlSi-N	0.84V	58.3	0.6	122.7	0.2	1	64.4	0.63
3 peak1 (4/16)	12:16 PM	AlSi/AlSi-N	0.84V	77.8	45.3	124	0.9	1	46.2	45.31
4 peak1 (4/16)	12:22 PM	AlSi/AlSi-N	0.84V	58	1.1	122.9	0.8	1	64.9	1.36
5 peak1 (4/16)	12:27 PM	AlSi/AlSi-N	0.84V	57.7	1	123.2	1.3	1	65.5	1.64
6 peak1 (4/16)	12:35 PM	AlSi/AlSi-N	0.84V	59.4	0.9	122.7	0.5	1	63.3	1.03
7 peak1 (4/16)	12:43 PM	AlSi/AlSi-N	0.84V	58.1	1.1	123.1	0.4	1	65	1.17
8 peak1 (4/16)	12:48 PM	AlSi/AlSi-N	0.84V	58	1	122.4	0.5	1	64.4	1.12
9 peak1 (4/16)	12:53 PM	AlSi/AlSi-N	0.84V	57.1	0.7	122	0.7	1	64.9	0.99
10 peak1 (4/16)	1:03 PM	AlSi/AlSi-N	0.84V	55.7	3.6	122	0.6	1	66.3	3.65
11 peak1 (4/16)	1:08 PM	AlSi/AlSi-N	0.82V	56.8	1.2	123	0.6	1	66.2	1.34
12 peak1 (4/16)	1:15 PM	AlSi/AlSi-N	0.82V	57.1	2.1	122.8	0.5	1	65.7	2.16
13 peak1 (4/16)	1:22 PM	AlSi/AlSi-N	0.82V	51.2	6	122	0.7	1	70.8	6.04
14 peak1 (4/16)	1:31 PM	AlSi/AlSi-N	0.82V	58.1	24.4	122.9	0.5	1	64.8	24.41
15 peak1 (4/16)	1:35 PM	AlSi/AlSi-N	0.82V	55.7	6	123.2	0.6	1	67.5	6.03
16 peak1 (4/16)	1:41 PM	AlSi/AlSi-N	0.79V	55.4	7.8	122.9	0.8	1	67.5	7.84
17 peak1 (4/16)	1:48 PM	AlSi/AlSi-N	0.79V	57.1	0.5	122.4	0.7	1	65.3	0.86
18 peak1 (4/16)	1:58 PM	AlSi/AlSi-N	0.79V	54.1	8.5	121.9	1.2	1	67.8	8.58

Run Number	Time	Material Set	PMT Voltage	Peak1	Peak1 uncer.	Peak2	Peak2 uncer.	Step Size	delta (theta)	Delta Uncer
19 peak1 (4/16)	2:03 PM	AlSi/AlSi-N	0.79V	67.5	23.5	123.5	8.2	1	56	24.89
20 peak1 (4/16)	2:13 PM	AlSi/AlSi-N	0.79V	56.5	11.2	122.7	1.3	1	66.2	11.28
21 peak1 (4/16)	2:25 PM	AlSi/AlSi-N	0.84V	58	0.9	122.5	0.3	0.5	64.5	0.95
22 peak1 (4/16)	3:08 PM	AlSi/AlSi-N	0.84V	57.4	11.1	121.8	4.9	0.5	64.4	12.13
24 peak1 (4/16)	3:31 PM	AlSi/AlSi-N	0.84V	70.9	19.6	122.2	1.1	0.5	51.3	19.63
25 peak1 (4/16)	3:41 PM	AlSi/AlSi-N	0.82V	63.8	6.2	123.3	0.8	0.5	59.5	6.25
26 peak1 (4/16)	3:53 PM	AlSi/AlSi-N	0.82V	55.8	2.2	123	1.6	0.5	67.2	2.72

Appendix C

Summary of Curve Fitting

This appendix lists the raw data from curve fitting of the LabVIEW data. Most curves were fitted with a single Gaussian curve (see Equation B.1). Some data sets were fitted with two Gaussian curves,

$$G(x) = A_1 e^{-(\frac{(x-b_1)}{c_1})^2} + A_2 e^{-(\frac{(x-b_2)}{c_2})^2} \tag{C.1}$$

The values for the coefficients (A_1, b_1, c_1, A_2, b_2, c_2) are listed with their associated uncertainties in parenthesis. A listing of X(y) is interpreted as $X \pm y$.

Run Number	Time	Material Set	PMT Voltage	A_1	b_1	c_1	A_2	b_2	c_2
13 peak1 (5/1)	14:03	AlSi/ AlSi-N	0.75V	0.11 (0.04)	50.75 (1.01)	3.95 (1.43)	n/a	n/a	n/a
13 peak2 (5/1)	14:03	AlSi/ AlSi-N	0.75V	0.09 (0.03)	108 (1.8)	6.25 (2.48)	n/a	n/a	n/a
14 peak1 (5/1)	14:08	AlSi/ AlSi-N	0.77V	0.13 (0.04)	53.56 (1.06)	4.06 (1.50)	n/a	n/a	n/a
14 peak2 (5/1)	14:08	AlSi/ AlSi-N	0.77V	0.09 (0.04)	113.4 (1.8)	5.59 (2.56)	n/a	n/a	n/a
15 peak1 (5/1)	14:14	AlSi/ AlSi-N	0.79V	0.18 (0.04)	48.27 (0.77)	3.97 (1.10)	n/a	n/a	n/a
15 peak2 (5/1)	14:14	AlSi/ AlSi-N	0.79V	0.09 (0.04)	106.2 (1.9)	5.18 (2.59)	n/a	n/a	n/a
16 peak1 (5/1)	14:19	AlSi/ AlSi-N	0.82V	0.30 (0.04)	54.42 (0.45)	3.98 (0.63)	n/a	n/a	n/a
16 peak2 (5/1)	14:19	AlSi/ AlSi-N	0.82V	0.15 (0.03)	114.1 (1.1)	5.94 (1.55)	n/a	n/a	n/a
17 peak1 (5/1)	14:24	AlSi/ AlSi-N	0.84V	0.54 (0.05)	50.02 (0.27)	3.92 (0.38)	n/a	n/a	n/a
17 peak2 (5/1)	14:24	AlSi/ AlSi-N	0.84V	0.20 (0.03)	111.9 (0.9)	6.97 (1.34)	n/a	n/a	n/a
18 peak1 (5/1)	14:30	AlSi/ AlSi-N	0.84V	0.62 (0.06)	54.25 (0.33)	4.36 (0.46)	n/a	n/a	n/a
18 peak2 (5/1)	14:30	AlSi/ AlSi-N	0.84V	0.13 (0.04)	117.5 (1.7)	7.36 (2.34)	n/a	n/a	n/a
B1 peak1 (5/25)	11:21	AlSi/ AlSi-N	0.84V	0.48 (0.05)	67.3 (0.1)	2.6 (0.2)	n/a	n/a	n/a
B1 peak2 (5/25)	11:21	AlSi/ AlSi-N	0.84V	0.26 (0.02)	135.9 (0.3)	3.96 (0.3)	n/a	n/a	n/a
B2 peak1 (5/25)	11:30	AlSi/ AlSi-N	0.84V	0.43 (0.02)	67.6 (0.2)	3.99 (0.24)	n/a	n/a	n/a

Run Number	Time	Material Set	PMT Voltage	A_1	b_1	c_1	A_2	b_2	c_2
B2 peak2 (5/25)	11:30	AlSi/ AlSi-N	0.84V	0.36 (0.02)	135.9 (0.1)	3.58 (0.25)	n/a	n/a	n/a
B3 peak1 (5/25)	11:46	AlSi/ AlSi-N	0.84V	0.47 (0.02)	46.8 (0.1)	3.5 (0.1)	0.03 (0.01)	29.4 (2.5)	9.8 (3.8)
B4 peak1 (5/25)	12:07	AlSi/ AlSi-N	0.84V	0.45 (0.01)	51.9 (0.1)	3.6 (0.1)	n/a	n/a	n/a
B5 peak1 (5/25)	12:37	AlSi/ AlSi-N	0.84V	0.44 (0.02)	48.2 (0.1)	3.5 (0.1)	n/a	n/a	n/a
B6 peak1 (5/25)	13:32	AlSi/ AlSi-N	0.84V	0.53 (0.02)	43.8 (0.1)	2.7 (0.1)	n/a	n/a	n/a
F1 peak1 (5/25)	11:16	AlSi/ AlSi-N	0.84V	0.22 (0.02)	68.2 (0.3)	3.4 (0.4)	n/a	n/a	n/a
F1 peak2 (5/25)	11:16	AlSi/ AlSi-N	0.84V	0.29 (0.03)	136 (0.3)	3.75 (0.4)	n/a	n/a	n/a
F2 peak1 (5/25)	11:26	AlSi/ AlSi-N	0.84V	0.52 (0.05)	68.5 (0.1)	2.95 (0.2)	n/a	n/a	n/a
F2 peak2 (5/25)	11:26	AlSi/ AlSi-N	0.84V	0.37 (0.02)	135.9 (0.2)	3.1 (0.2)	n/a	n/a	n/a
F3 peak1 (5/25)	11:41	AlSi/ AlSi-N	0.84V	0.51 (0.02)	65.3 (0.1)	2.97 (0.12)	n/a	n/a	n/a
F4 peak1 (5/25)	11:56	AlSi/ AlSi-N	0.84V	0.44 (0.02)	62.6 (0.1)	3.5 (0.1)	n/a	n/a	n/a
F5 peak1 (5/25)	12:23	AlSi/ AlSi-N	0.84V	0.43 (0.02)	56.1 (0.1)	3.5 (0.2)	n/a	n/a	n/a
F6 peak1 (5/25)	13:07	AlSi/ AlSi-N	0.84V	0.47 (0.01)	48.3 (0.1)	2.8 (0.1)	n/a	n/a	n/a
19 peak2 (5/1)	15:12	Si/SiO 10%	0.75V	0.06 (0.03)	109.4 (1.8)	6.54 (3.88)	n/a	n/a	n/a
20 peak1 (5/1)	15:17	Si/SiO 10%	0.77V	0.04 (0.01)	69.91 (23.5)	41.48 (32.17)	n/a	n/a	n/a

Run Number	Time	Material Set	PMT Voltage	A_1	b_1	c_1	A_2	b_2	c_2
20 peak2 (5/1)	15:17	Si/SiO 10%	0.77V	0.04 (0.02)	116.6 (7.4)	14.11 (10.54)	n/a	n/a	n/a
21 peak1 (5/1)	15:22	Si/SiO 10%	0.79V	0.04 (0.02)	78.53 (32.8)	40.49 (36.85)	n/a	n/a	n/a
21 peak2 (5/1)	15:22	Si/SiO 10%	0.79V	0.06 (0.03)	113.4 (3.5)	8.63 (4.92)	n/a	n/a	n/a
22 peak1 (5/1)	15:27	Si/SiO 10%	0.82V	0.1 (0.04)	44.74 (1.46)	4.29 (2.07)	0.08 (0.02)	69.77 (2.91)	11.59 (4.28)
22 peak2 (5/1)	15:27	Si/SiO 10%	0.82V	0.03 (0.02)	118.5 (13.8)	25.44 (21.47)	n/a	n/a	n/a
23 peak1 (5/1)	15:32	Si/SiO 10%	0.84V	0.04 (0.02)	67.92 (23.2)	40.6 (33.25)	n/a	n/a	n/a
23 peak2 (5/1)	15:32	Si/SiO 10%	0.84V	0.05 (0.03)	107.7 (5.3)	13.29 (8.01)	n/a	n/a	n/a
24 peak1 (5/1)	15:56	Si/SiO 10%	0.84V	0.2 (0.04)	54.98 (0.82)	4.61 (1.15)	n/a	n/a	n/a
24 peak2 (5/1)	15:56	Si/SiO 10%	0.84V	0.13 (0.04)	112.6 (1.0)	3.77 (1.49)	n/a	n/a	n/a
25 peak1 (5/1)	16:03	Si/SiO 10%	0.75V	0.08 (0.03)	47.37 (2.15)	6.52 (3.04)	n/a	n/a	n/a
25 peak2 (5/1)	16:03	Si/SiO 10%	0.75V	0.05 (0.02)	105.3 (5.36)	12.43 (8.15)	n/a	n/a	n/a
26 peak1 (5/1)	16:08	Si/SiO 10%	0.77V	0.05 (0.02)	61.03 (6.07)	19.64 (8.89)	n/a	n/a	n/a
26 peak2 (5/1)	16:08	Si/SiO 10%	0.77V	0.04 (0.4)	111.8 (5.2)	8.92 (7.31)	n/a	n/a	n/a
27 peak1 (5/1)	16:13	Si/SiO 10%	0.79V	0.08 (0.04)	54.77 (2.13)	5.76 (3.01)	n/a	n/a	n/a
27 peak2 (5/1)	16:13	Si/SiO 10%	0.79V	0.05 (0.02)	115.9 (5.0)	12.7 (7.2)	n/a	n/a	n/a

Run Number	Time	Material Set	PMT Voltage	A_1	b_1	c_1	A_2	b_2	c_2
28 peak1 (5/1)	16:18	Si/SiO 10%	0.82V	0.18 (0.07)	53.3 (0.7)	2.35 (1.0)	n/a	n/a	n/a
28 peak2 (5/1)	16:18	Si/SiO 10%	0.82V	0.09 (0.03)	112.9 (2.3)	7.64 (3.29)	n/a	n/a	n/a
29 peak1 (5/1)	16:23	Si/SiO 10%	0.84V	0.14 (0.05)	55.18 (1.32)	5.22 (1.86)	n/a	n/a	n/a
29 peak2 (5/1)	16:23	Si/SiO 10%	0.84V	0.08 (0.03)	115.1 (2.1)	7.38 (3.54)	n/a	n/a	n/a
30 peak1 (5/1)	16:37	Si/SiO 10%	0.84V	0.23 (0.05)	55.05 (0.67)	4.05 (0.95)	n/a	n/a	n/a
30 peak2 (5/1)	16:37	Si/SiO 10%	0.84V	0.05 (0.02)	119.4 (7.1)	18.74 (10.2)	n/a	n/a	n/a
35 peak1 (5/1)	17:50	Si/SiO 5%T	0.75V	0.51 (0.08)	48.49 (0.46)	3.60 (0.64)	n/a	n/a	n/a
35 peak2 (5/1)	17:50	Si/SiO 5%T	0.75V	0.09 (0.05)	109.4 (1.0)	2.54 (1.51)	n/a	n/a	n/a
36 peak1 (5/1)	17:55	Si/SiO 5%T	0.77V	0.56 (0.09)	52.2 (0.4)	3.01 (0.59)	0.23 (0.05)	61.55 (1.93)	6.97 (2.83)
36 peak2 (5/1)	17:55	Si/SiO 5%T	0.77V	0.05 (0.03)	116.9 (4.7)	8.78 (6.67)	n/a	n/a	n/a
37 peak1 (5/1)	18:00	Si/SiO 5%T	0.79V	0.51 (0.13)	46.96 (0.42)	2.77 (0.84)	0.31 (0.05)	55.01 (2.42)	9.57 (2.71)
37 peak2 (5/1)	18:00	Si/SiO 5%T	0.79V	0.13 (0.06)	109.4 (1.0)	2.76 (1.42)	n/a	n/a	n/a
38 peak1 (5/1)	18:05	Si/SiO 5%T	0.82V	0.57 (0.08)	54.17 (0.92)	7.5 (1.3)	n/a	n/a	n/a
39 peak1 (5/1)	18:10	Si/SiO 5%T	0.84V	0.59 (0.1)	51.7 (1.4)	10.23 (1.98)	n/a	n/a	n/a
39 peak2 (5/1)	18:10	Si/SiO 5%T	0.84V	0.07 (0.03)	110.5 (3.5)	8.62 (5.0)	n/a	n/a	n/a

Run Number	Time	Material Set	PMT Voltage	A_1	b_1	c_1	A_2	b_2	c_2
40 peak1 (5/1)	18:16	Si/SiO 5%T	0.84V	0.52 (0.1)	54.75 (1.35)	8.84 (1.91)	n/a	n/a	n/a
40 peak2 (5/1)	18:16	Si/SiO 5%T	0.84V	0.12 (0.05)	113.7 (1.0)	2.83 (1.43)	n/a	n/a	n/a
41 peak1 (5/1)	18:26	Si/SiO 5%T	0.75V	0.26 (0.04)	49.7 (0.9)	8.36 (1.25)	n/a	n/a	n/a
41 peak2 (5/1)	18:26	Si/SiO 5%T	0.75V	0.03 (0.02)	114.9 (7.2)	17.9 (7.6)	n/a	n/a	n/a
42 peak1 (5/1)	18:36	Si/SiO 5%T	0.77V	0.55 (0.05)	48.4 (0.4)	3.57 (0.4)	n/a	n/a	n/a
42 peak2 (5/1)	18:36	Si/SiO 5%T	0.77V	0.03 (0.01)	115.6 (8.0)	20.98 (12.15)	n/a	n/a	n/a
43 peak1 (5/1)	18:45	Si/SiO 5%T	0.79V	0.39 (0.03)	52.6 (0.6)	6.6 (0.8)	n/a	n/a	n/a
43 peak2 (5/1)	18:45	Si/SiO 5%T	0.79V	0.19 (0.05)	113.6 (0.3)	1.3 (0.4)	n/a	n/a	n/a
44 peak1 (5/1)	18:57	Si/SiO 5%T	0.82V	0.7 (0.07)	52.9 (0.3)	3.67 (0.4)	n/a	n/a	n/a
44 peak2 (5/1)	18:57	Si/SiO 5%T	0.82V	0.1 (0.03)	115.9 (1.2)	5.3 (1.7)	n/a	n/a	n/a
45 peak1 (5/1)	19:07	Si/SiO 5%T	0.84V	0.85 (0.08)	53.27 (0.16)	2.4 (0.3)	0.28 (0.05)	58.5 (1.4)	9.5 (1.4)
45 peak2 (5/1)	19:07	Si/SiO 5%T	0.84V	0.15 (0.04)	116.3 (0.7)	3.53 (1.6)	n/a	n/a	n/a
46 peak1 (5/1)	19:17	Si/SiO 5%T	0.84V	0.93 (0.08)	47.6 (0.2)	3.23 (0.31)	0.26 (0.04)	56.4 (1.4)	6.3 (2.0)
46 peak2 (5/1)	19:17	Si/SiO 5%T	0.84V	0.19 (0.04)	110.5 (0.4)	3.18 (0.7)	n/a	n/a	n/a
1 peak1 (4/30)	15:09	Si/SiO 5%	0.75V	0.08 (0.03)	66.7 (1.5)	5.62 (2.1)	n/a	n/a	n/a

Run Number	Time	Material Set	PMT Voltage	A_1	b_1	c_1	A_2	b_2	c_2
1 peak2 (4/30)	15:09	Si/SiO 5%	0.75V	0.29 (0.04)	123.7 (0.4)	3.47 (1.43)	n/a	n/a	n/a
2 peak1 (4/30)	15:25	Si/SiO 5%	0.82V	0.12 (0.05)	61.5 (1.2)	4.6 (1.8)	n/a	n/a	n/a
2 peak2 (4/30)	15:25	Si/SiO 5%	0.82V	0.27 (0.05)	120.3 (0.5)	3.4 (0.7)	n/a	n/a	n/a
3 peak1 (4/30)	15:31	Si/SiO 5%	0.84V	0.03 (0.02)	54.4 (9.7)	17.8 (13.0)	n/a	n/a	n/a
3 peak2 (4/30)	15:31	Si/SiO 5%	0.84V	0.08 (0.05)	122.3 (1.5)	2.6 (2.0)	n/a	n/a	n/a
5 peak 1 (4/30)	15:43	Si/SiO 5%	0.75V	1.02 (0.07)	68.4 (0.2)	3.16 (0.17)	n/a	n/a	n/a
5 peak 2 (4/30)	15:43	Si/SiO 5%	0.75V	0.19 (0.05)	127.1 (0.8)	4.4 (1.2)	n/a	n/a	n/a
6 peak1 (4/30)	15:49	Si/SiO 5%	0.77V	1.06 (0.1)	70.6 (0.3)	4.1 (0.4)	n/a	n/a	n/a
6 peak2 (4/30)	15:49	Si/SiO 5%	0.77V	0.15 (0.4)	130.5 (1.2)	5.6 (1.8)	n/a	n/a	n/a
7 peak1 (4/30)	15:55	Si/SiO 5%	0.79V	1.71 (0.11)	69.5 (0.2)	3.2 (0.23)	n/a	n/a	n/a
7 peak2 (4/30)	15:55	Si/SiO 5%	0.79V	0.3 (0.06)	129.9 (0.6)	4.4 (0.9)	n/a	n/a	n/a
8 peak1 (4/30)	16:01	Si/SiO 5%	0.82V	1.89 (0.11)	65.5 (0.2)	3.5 (0.2)	n/a	n/a	n/a
8 peak2 (4/30)	16:01	Si/SiO 5%	0.82V	0.32 (0.06)	126.6 (0.6)	4.2 (0.8)	n/a	n/a	n/a
9 peak1 (4/30)	16:07	Si/SiO 5%	0.84V	2.48 (0.19)	64.2 (0.2)	2.68 (0.12)	n/a	n/a	n/a
9 peak2 (4/30)	16:07	Si/SiO 5%	0.84V	0.36 (0.06)	124.9 (0.5)	4.34 (0.78)	n/a	n/a	n/a

Run Number	Time	Material Set	PMT Voltage	A_1	b_1	c_1	A_2	b_2	c_2
10 peak1 (4/30)	16:12	Si/SiO 5%	0.84V	2.4 (0.2)	66.2 (0.2)	3.1 (0.2)	n/a	n/a	n/a
10 peak2 (4/30)	16:12	Si/SiO 5%	0.84V	0.41 (0.06)	126.4 (0.4)	4.1 (0.6)	n/a	n/a	n/a
1001 peak1 (4/30)	18:18	Si/SiO 5%	0.79V	0.28 (0.05)	45.4 (0.6)	4.1 (0.9)	n/a	n/a	n/a
1001 peak2 (4/30)	18:18	Si/SiO 5%	0.79V	0.67 (0.06)	105.5 (0.2)	1.8 (0.2)	n/a	n/a	n/a
13 peak1 (4/30)	16:44	Si/SiO 5%	0.75V	0.08 (0.05)	60.4 (0.9)	4.5 (2.7)	n/a	n/a	n/a
13 peak2 (4/30)	16:44	Si/SiO 5%	0.75V	0.08 (0.04)	123.2 (2.3)	5.9 (3.2)	n/a	n/a	n/a
18 peak1 (4/30)	17:51	Si/SiO 5%	0.79V	(0.6 (0.1)	51.8 (0.3)	3.2 (0.4)	n/a	n/a	n/a
18 peak2 (4/30)	17:51	Si/SiO 5%	0.79V	?	?	?	n/a	n/a	n/a
19 peak1 (4/30)	17:57	Si/SiO 5%	0.79V	2.39 (0.26)	54.86 (0.11)	1.27 (0.16)	n/a	n/a	n/a
19 peak2 (4/30)	17:57	Si/SiO 5%	0.79V	0.4 (0.05)	108.1 (0.3)	1.9 (0.5)	n/a	n/a	n/a
20 peak1 (4/30)	18:05	Si/SiO 5%	0.79V	0.22 (0.04)	53.7 (0.8)	5.7 (1.1)	n/a	n/a	n/a
20 peak2 (4/30)	18:05	Si/SiO 5%	0.79V	1.89 (0.2)	109.8 (0.1)	2.7 (0.2)	n/a	n/a	n/a
21 peak1 (4/30)	6:11 PM	Si/SiO 5%	0.79V	0.06 (0.03)	48.98 (2.58)	6.9 (3.6)	n/a	n/a	n/a
21 peak2 (4/30)	18:11	Si/SiO 5%	0.79V	2.87 (0.15)	108.7 (0.2)	3.45 (0.2)	n/a	n/a	n/a
bkup peak1 (4/30)	15:14	Si/SiO 5%	0.77V	0.12 (0.04)	65.1 (0.9)	4.87 (1.4)	n/a	n/a	n/a

Run Number	Time	Material Set	PMT Voltage	A_1	b_1	c_1	A_2	b_2	c_2
bkup peak2 (4/30)	15:14	Si/SiO 5%	0.77V	0.34 (0.04)	123.9 (0.5)	4.7 (0.7)	n/a	n/a	n/a
bkup_1 peak1 (4/30)	15:20	Si/SiO 5%	0.79V	0.08 (0.02)	66.1 (2.0)	9.8 (2.7)	n/a	n/a	n/a
bkup_1 peak2 (4/30)	15:20	Si/SiO 5%	0.79V	0.43 (0.03)	124 (0.3)	3. (0.3)	n/a	n/a	n/a
22 peak1 (5/23)	17:41	Si/SiO 5%	0.82V	0.68 (0.02)	50.5 (0.1)	0.97 (0.07)	n/a	n/a	n/a
21 peak1 (5/23)	17:41	Si/SiO 5%	0.82V	0.68 (0.02)	61.5 (0.1)	3.53 (0.09)	n/a	n/a	n/a
19 peak1 (5/23)	17:02	Si/SiO 5%	0.82V	0.69 (0.02)	57.9 (0.1)	3.3 (0.1)	n/a	n/a	n/a
18 peak1 (5/23)	16:49	Si/SiO 5%	0.82V	0.58 (0.02)	56.4 (0.1)	34. (0.2)	0.07 (0.01)	38.5 (1.5)	8.8 (2.0)
18 peak2 (5/23)	16:49	Si/SiO 5%	0.82V	0.23 (0.01)	123.8 (0.2)	3.9 (0.2)	n/a	n/a	n/a
17 peak1 (5/23)	16:27	Si/SiO 5%	0.82V	0.34 (0.02)	56.23 (0.2)	3.7 (0.2)	0.08 (0.01)	41.4 (1.0)	8.8 (1.5)
17 peak2 (5/23)	16:27	Si/SiO 5%	0.82V	0.23 (0.02)	123.7 (0.2)	3.9 (0.4)	n/a	n/a	n/a
16 peak1 (5/23)	16:17	Si/SiO 5%	0.82V	0.83 (0.04)	56.1 (0.1)	3.7 (0.2)	n/a	n/a	n/a
16 peak2 (5/23)	16:17	Si/SiO 5%	0.82V	0.32 (0.02)	123.4 (0.2)	3.7 (0.3)	n/a	n/a	n/a
15 peak1 (5/23)	16:09	Si/SiO 5%	0.82V	0.72 (0.08)	54.3 (0.3)	3.97 (0.5)	n/a	n/a	n/a
15 peak2 (5/23)	16:09	Si/SiO 5%	0.82V	0.24 (0.02)	122.1 (0.3)	4.1 (0.4)	n/a	n/a	n/a
01 peak1 (5/1)	10:32	Si/SiO 5%	0.79V	0.47 (0.05)	47.36 (0.28)	3.04 (0.4)	N/A	N/A	N/A

Run Number	Time	Material Set	PMT Voltage	A_1	b_1	c_1	A_2	b_2	c_2
01 peak1 (5/1)	10:32	Si/SiO 5%	0.79V	0.50 (0.05)	107.5 (0.3)	3.65 (0.4)	N/A	N/A	N/A
02 peak1 (5/1)	10:42	Si/SiO 5%	0.75V	0.49 (0.06)	49.13 (0.29)	2.99 (0.43)	N/A	N/A	N/A
02 peak2 (5/1)	10:42	Si/SiO 5%	0.75V	0.29 (0.03)	109.3 (0.3)	3.75 (0.4)	N/A	N/A	N/A
06 peak1 (5/1)	11:14	Si/SiO 5%	0.77V	0.57 (0.04)	54.87 (0.19)	3.05 (0.27)	N/A	N/A	N/A
06 peak2 (5/1)	11:14	Si/SiO 5%	0.77V	0.35 (0.04)	115 (0.3)	3.68 (0.4)	N/A	N/A	N/A
07 peak1 (5/1)	11:30	Si/SiO 5%	0.79V	0.71 (0.05)	53.37 (0.13)	2.3 (0.18)	N/A	N/A	N/A
07 peak2 (5/1)	11:30	Si/SiO 5%	0.79V	0.31 (0.04)	113.4 (0.3)	3.8 (0.01)	N/A	N/A	N/A
08 peak1 (5/1)	11:44	Si/SiO 5%	0.82V	0.8 (0.05)	48.9 (0.13)	2.6 (0.18)	N/A	N/A	N/A
08 peak2 (5/1)	11:44	Si/SiO 5%	0.82V	0.31 (0.04)	109 (0.3)	3.7 (0.5)	N/A	N/A	N/A
09 peak1 (5/1)	11:58	Si/SiO 5%	0.75V	0.48 (0.04)	45.53 (0.19)	2.6 (0.28)	N/A	N/A	N/A
09 peak2 (5/1)	11:58	Si/SiO 5%	0.75V	0.18 (0.04)	105.8 (0.5)	3.4 (0.8)	N/A	N/A	N/A
11 peak1 (5/1)	12:11	Si/SiO 5%	0.77V	0.40 (0.05)	46.12 (0.32)	3.2 (0.5)	N/A	N/A	N/A
11 peak2 (5/1)	12:11	Si/SiO 5%	0.77V	0.24 (0.04)	106.1 (0.4)	2.8 (0.6)	N/A	N/A	N/A
12 peak1 (5/1)	13:49	Si/SiO 5%	0.75V	0.98 (0.04)	56.51 (0.19)	5.1 (0.3)	N/A	N/A	N/A
12 peak2 (5/1)	13:49	Si/SiO 5%	0.75V	0.08 (0.04)	115.6 (2.0)	5.3 (2.9)	N/A	N/A	N/A

Run Number	Time	Material Set	PMT Voltage	A_1	b_1	c_1	A_2	b_2	c_2
1 peak1 (4/16)	12:01	AlSi/ AlSi-N	0.84V	0.26 (0.03)	57.8 (0.6)	6.1 (0.9)	N/A	N/A	N/A
1 peak2 (4/16)	12:01	AlSi/ AlSi-N	0.84V	0.97 (0.06)	122.8 (0.3)	4.5 (0.3)	N/A	N/A	N/A
2 peak1 (4/16)	12:07	AlSi/ AlSi-N	0.84V	0.39 (0.06)	58.3 (0.6)	4.8 (0.7)	N/A	N/A	N/A
2 peak2 (4/16)	12:07	AlSi/ AlSi-N	0.84V	0.61 (0.03)	122.7 (0.2)	5.1 (0.4)	N/A	N/A	N/A
3 peak1 (4/16)	12:16	AlSi/ AlSi-N	0.84V	0.01 (0.01)	77.8 (45.3)	29.2 (57.6)	N/A	N/A	N/A
3 peak2 (4/16)	12:16	AlSi/ AlSi-N	0.84V	0.08 (0.02)	124 (0.9)	4.8 (1.3)	N/A	N/A	N/A
4 peak1 (4/16)	12:22	AlSi/ AlSi-N	0.84V	0.06 (0.02)	58.0 (1.1)	4.3 (1.6)	N/A	N/A	N/A
4 peak2 (4/16)	12:22	AlSi/ AlSi-N	0.84V	0.1 (0.02)	122.9 (0.8)	5.8 (1.2)	N/A	N/A	N/A
5 peak1 (4/16)	12:27	AlSi/ AlSi-N	0.84V	0.06 (0.01)	57.7 (1.0)	4.9 (1.4)	N/A	N/A	N/A
5 peak1 (4/16)	12:27	AlSi/ AlSi-N	0.84V	0.28 (0.02)	123.2 (1.3)	3.4 (0.4)	N/A	N/A	N/A
6 peak1 (4/16)	12:35	AlSi/ AlSi-N	0.84V	0.05 (0.01)	59.4 (0.9)	4.3 (1.4)	N/A	N/A	N/A
6 peak2 (4/16)	12:35	AlSi/ AlSi-N	0.84V	0.15 (0.02)	122.7 (0.5)	5.1 (0.7)	N/A	N/A	N/A
7 peak1 (4/16)	12:43	AlSi/ AlSi-N	0.84V	0.05 (0.01)	58.1 (1.1)	6.3 (1.5)	N/A	N/A	N/A
7 peak2 (4/16)	12:43	AlSi/ AlSi-N	0.84V	0.13 (0.02)	123.1 (0.4)	5.0 (0.6)	N/A	N/A	N/A
8 peak1 (4/16)	12:48	AlSi/ AlSi-N	0.84V	0.05 (0.01)	58.0 (1.0)	5.8 (1.5)	N/A	N/A	N/A

Run Number	Time	Material Set	PMT Voltage	A_1	b_1	c_1	A_2	b_2	c_2
8 peak2 (4/16)	12:48	AlSi/ AlSi-N	0.84V	0.09 (0.01)	122.4 (0.5)	5.5 (0.6)	N/A	N/A	N/A
9 peak1 (4/16)	12:53	AlSi/ AlSi-N	0.84V	0.05 (0.01)	57.1 (0.7)	3.9 (1.0)	N/A	N/A	N/A
9 peak2 (4/16)	12:53	AlSi/ AlSi-N	0.84V	0.05 (0.01)	122 (0.7)	5.5 (1.0)	N/A	N/A	N/A
10 peak1 (4/16)	13:03	AlSi/ AlSi-N	0.84V	0.02 (0.01)	55.7 (3.6)	19.0 (5.2)	N/A	N/A	N/A
10 peak2 (4/16)	13:03	AlSi/ AlSi-N	0.84V	0.06 (0.01)	122 (0.6)	5.4 (0.7)	N/A	N/A	N/A
11 peak1 (4/16)	13:08	AlSi/ AlSi-N	0.82V	0.04 (0.01)	56.8 (1.2)	7.7 (1.9)	N/A	N/A	N/A
11 peak2 (4/16)	13:08	AlSi/ AlSi-N	0.82V	0.06 (0.01)	123 (0.6)	5.3 (0.8)	N/A	N/A	N/A
12 peak1 (4/16)	13:15	AlSi/ AlSi-N	0.82V	0.02 (0.01)	57.1 (2.1)	17.1 (4.5)	N/A	N/A	N/A
12 peak2 (4/16)	13:15	AlSi/ AlSi-N	0.82V	0.09 (0.01)	122.8 (0.5)	3.6 (0.7)	N/A	N/A	N/A
13 peak1 (4/16)	13:22	AlSi/ AlSi-N	0.82V	0.01 (0.00)	51.2 (6.0)	33.4 (9.5)	N/A	N/A	N/A
13 peak2 (4/16)	13:22	AlSi/ AlSi-N	0.82V	0.06 (0.01)	122 (0.7)	5.6 (0.9)	N/A	N/A	N/A
14 peak1 (4/16)	13:31	AlSi/ AlSi-N	0.82V	0.01 (0.00)	58.1 (24.4)	65.4 (51.4)	N/A	N/A	N/A
14 peak2 (4/16)	13:31	AlSi/ AlSi-N	0.82V	0.06 (0.01)	122.9 (0.5)	4.1 (0.7)	N/A	N/A	N/A
15 peak1 (4/16)	13:35	AlSi/ AlSi-N	0.82V	0.01 (0.00)	55.7 (6.0)	26.3 (8.9)	N/A	N/A	N/A
15 peak2 (4/16)	13:35	AlSi/ AlSi-N	0.82V	0.05 (0.01)	123.2 (0.6)	4.5 (0.8)	N/A	N/A	N/A

Run Number	Time	Material Set	PMT Voltage	A_1	b_1	c_1	A_2	b_2	c_2
16 peak1 (4/16)	13:41	AlSi/ AlSi-N	0.79V	0.01 (0.00)	55.4 (7.8)	36.2 (12.6)	N/A	N/A	N/A
16 peak2 (4/16)	13:41	AlSi/ AlSi-N	0.79V	0.04 (0.01)	122.9 (0.8)	5.3 (1.3)	N/A	N/A	N/A
17 peak1 (4/16)	13:48	AlSi/ AlSi-N	0.79V	0.05 (0.01)	57.1 (0.5)	3.0 (0.7)	N/A	N/A	N/A
17 peak2 (4/16)	13:48	AlSi/ AlSi-N	0.79V	0.05 (0.01)	122.4 (0.7)	5.6 (1.0)	N/A	N/A	N/A
18 peak1 (4/16)	13:58	AlSi/ AlSi-N	0.79V	0.01 (0.00)	54.1 (8.5)	39.9 (14.7)	N/A	N/A	N/A
18 peak2 (4/16)	13:58	AlSi/ AlSi-N	0.79V	0.03 (0.01)	121.9 (1.2)	7.2 (1.7)	N/A	N/A	N/A
19 peak1 (4/16)	14:03	AlSi/ AlSi-N	0.79V	0.01 (0.01)	67.5 (23.5)	45.1 (33.6)	N/A	N/A	N/A
19 peak2 (4/16)	14:03	AlSi/ AlSi-N	0.79V	0.01 (0.01)	123.5 (8.2)	34.3 (13.3)	N/A	N/A	N/A
20 peak1 (4/16)	14:13	AlSi/ AlSi-N	0.79V	0.01 (0.01)	56.5 (11.2)	39.1 (18.5)	N/A	N/A	N/A
20 peak2 (4/16)	14:13	AlSi/ AlSi-N	0.79V	0.02 (0.02)	122.7 (1.3)	5.4 (1.8)	N/A	N/A	N/A
21 peak1 (4/16)	14:25	AlSi/ AlSi-N	0.84V	0.05 (0.01)	58.0 (0.9)	6.9 (1.4)	N/A	N/A	N/A
21 peak2 (4/16)	14:25	AlSi/ AlSi-N	0.84V	0.11 (0.01)	122.5 (0.3)	4.5 (0.5)	N/A	N/A	N/A
22 peak1 (4/16)	15:08	AlSi/ AlSi-N	0.84V	0.01 (0.01)	57.4 (11.1)	54.1 (21.3)	N/A	N/A	N/A
22 peak2 (4/16)	15:08	AlSi/ AlSi-N	0.84V	0.01 (0.01)	121.8 (4.9)	31.4 (7.8)	N/A	N/A	N/A
24 peak1 (4/16)	15:31	AlSi/ AlSi-N	0.84V	0.02 (0.02)	70.9 (19.6)	38.1 (28.5)	N/A	N/A	N/A

Run Number	Time	Material Set	PMT Voltage	A_1	b_1	c_1	A_2	b_2	c_2
24 peak2 (4/16)	15:31	AlSi/ AlSi-N	0.84V	0.1 (0.03)	122.2 (1.1)	5.5 (1.7)	N/A	N/A	N/A
25 peak1 (4/16)	15:41	AlSi/ AlSi-N	0.82V	0.03 (0.01)	63.8 (6.2)	17.5 (9.0)	N/A	N/A	N/A
25 peak2 (4/16)	15:41	AlSi/ AlSi-N	0.82V	0.2 (0.1)	123.3 (0.8)	5.2 (1.0)	N/A	N/A	N/A
26 peak1 (4/16)	15:53	AlSi/ AlSi-N	0.82V	0.05 (0.03)	55.8 (2.2)	4.0 (3.0)	N/A	N/A	N/A
26 peak2 (4/16)	15:53	AlSi/ AlSi-N	0.82V	0.1 (0.04)	123 (1.6)	6.8 (2.5)	N/A	N/A	N/A

Appendix D

Summary of Depositions

The studies detailed in this thesis used three material sets: AlSi/ Ag/ AlSi-N (15% Nitrogen), Si/ Ag/ SiO(x) (5% Oxygen), Si/ Ag/ SiO(x) (10% Oxygen). However, over the two year span of this research, several other material sets were studied as possible candidates for SPCE. These include a series of Si/ Ag/ Si-N (with varying percentages of Nitrogen) and Al/ Ag/ Al-N (15% Nitrogen). The results of these depositions are summarized below.

- *Results of Al/Ag/Al-N series*, Slides were not pre-cleaned with ethanol. Any cleaning of the substrate was covered under what the manufacture described as "pre-cleaned". These films aged poorly- the quality of the film quickly degraded on a scale of a few hours of being exposed to atmospheric pressure and humidity of lab atmosphere. Small air bubbles formed between the Aluminum layer and the glass substrate and impaired the adhesion of the silver film. Slides were sent to UMD for SPCE testing. Dye spun on was Flurol 7G. (Conclusive results from Gryczyski's regarding this series and SPCE was not available). SPCE was not observed at UNH with this series because Flurol 7G reacts weakly to the wavelength of light we had available (in Summer 2005 we were using 488 nm light for excitation).

- *Results of heating on adhesion*, 50 nm of AlSi was deposited on heated and unheated slides. The slides were not cleaned in any way aside from what the manufaturer defines

as "pre-cleaned". The deposition on an unheated slide was run at room temperature. The deposition on a heated slide was run at 200° C. The adhesion of the AlSi film to the glass slide seemed to improve with heating. However, a discoloration of the back of the slide was observed when the sample was heated. The back of the film took on a distinct bronze color. Heating of samples was not pursued as a means of improving adhesion. The use of the DC power source with the AlSi target did not give ideal run conditions- the runs were constantly interrupted by loss of the plasma.

- *Results of the AlSi/Ag/AlSi-N series*, Slides were not pre-cleaned with ethanol. Any cleaning of the substrate was covered under what the manufacture described as "pre-cleaned". Using the RF power source on the AlSi, AlSi-N layers gave more consistent run conditions. Prior to any AlSi deposition there was a 5 minute pre-sputter of the target. The AlSi better adhered to the glass slide, however, air corrosion still occurred as in the Al series. Slides of variant passivation layers were sent to UMD for SPCE testing. A slide from run #05-110 and #05-111 was tested at UMD and SPCE was observed. Slides were coated with Fluorol 7G dye. SPCE was not observed at UNH because the dye used weakly interacts with the wavelength of light used for excitation (in Summer 2005, 488 nm light was used).

- *Results of runs #05-120 through 05-122*, A series of runs to make several duplicate slides for initial tests of SPCE at UNH. Slides were not pre-cleaned with ethanol. Corrosion of films was still a problem. A 532 nm laser was procured for SPCE tests. Dyes chosen for testing were: Rhodamine Red because of excitation at 532 nm. Before testing for SPCE occured, tests for SPR were run. The slides showed strong increase in light intensity. The occurence of strong SPR signal indicated that these slides

should give strong SPCE signals.

- *Results of runs #05-206 through 05-208*, Initially the series of three runs was to make several slides of identical compositions for SPCE tests at UNH. This series was used to investigate the effect of ethanol cleaning on film quality. Ethanol cleaning of the slides consisted of dousing each slide with 200 proof ethanol and wiping dry with lint-free cloth. Comparisons between the ethanol cleaned and "pre-cleaned" slides showed that ethanol cleaned slides have remarkably improved in film quality and a significantly decreased in the corrosion which plagued earlier runs. Films deposited on ethanol cleaned slides appear "cleaner" with less visible imperfections and age much better when exposed to normal lab conditions.

- *First SPCE tests at UNH*, SPCE testing at UNH began on 11/10/05 using slides from runs #05-120 through 05-122 and #05-206 through 05-207. The first tests were done with 10 milimolar Rhodamine dye in a 1% PVA solution. The 532 nm laser was used to excite the dye. No SPCE was observed. However, strong SPR signal was seen. The SPCE may have been inhibited by the dye self-quenching or a decrease in fluorescence may have occured due to the pH of the solution.

- *Results of runs #05-211 through 05-216*, Intended to be a series of films with varying passivation layer thicknesses. However, the constant loss of plasma during the AlSi-N layer lead to a series of films of indeterminate film thicknesses. Run #05-213, a stationary run did not show any SPR signal.

- *Results of run #05-220*, Intended as a control, the thicker Ag layer did not show any SPR signal.

- *Second SPCE tests at UNH*, On 1/20/06, second tests of SPCE were performed at UNH. Using Alexa Fluor 532 dye and different concentrations on uncoated slides from first SPCE tests. Concentrations used were: 660 nano-molar and 900 nano-molar. Coated slides again showed increased intensity of light emission near specific angles. However no change in emission color was observed.

- *Third SPCE tests at UNH*, On 3/2/06, third tests of SPCE were performed at UNH. Using 750 nano-molar concentration of Alexa Fluor 532 dye and 660 nano-molar concentration of Rhodamine Red dye to coat two uncoated slides from the previous tests. SPCE was observed. When viewed through a filter, the slide coated with Rhodamine Red dye displayed red emission at the SPR angle.

- *Result of Run #06-067*, Si adheres very well to glass slide, even slide that hasn't been cleaned with ethanol.

- *Results of Silicon as an adhesion layer*, From run #06-067, it was seen that a 2 nm layer of Silicon provided a good adhesion to a "pre-cleaned" glass slide. Attempts to use a thinner layer on a "pre-cleaned" slide did not result in good adhesion, the silver film was easily removed by tape. By cleaning the slides with ethanol prior to deposition, the Silicon layer could be reduced to 1nm and still provide good adhesion to the glass slide.

- *Preliminary results of Si/Ag/Si-N series*, SPR tests on runs #06-079 through 06-080 showed very weak, dim signal enhancement when compared to the results of the AlSi/Ag/AlSi-N series. Run #06-082 gave a signal enhancement comprable to the AlSi series. Run #06-083 was able to reproduce the results found from 06-082. Runs #06-084 through 06-086 investigated how thinner passivation layers affected the SPR

signal. As of this time, SPCE has not been tested or attempted using this new set of films. Future tests of SPCE will be run on films which duplicate run #06-084 and run #06-086. Based on the strength of the SPR signal observed it is believed that these films should produce an observable SPCE signal.

- *SPCE Tests of the Si/Ag/Si-N series*, The strong SPR signal seen on this series indicated that a strong SPCE signal would be seen. 660 nM solutions of Rhodamine Red and 750 nM solution of Alexa Fluor 532 were prepared. The slides showed strong SPR signal enhancement, however, no SPCE was observed. Additionally, after one day the coated slides showed severe deterioration in film appearance.

- *SPCE tests of Runs 06-102– 06-107*, 660 nM solution of Rhodamine Red and 750nM solution of Alexa Fluor 532 were used to test for SPCE. No slide showed a distinct SPCE signal, though there was signal enhancement at certain angles. All slides eventually eroded and deteriorated within a few days. The slides with some Nitrogen (5%) deteriorated the slowest.

- *Adhesion tests for Al*, Poor adhesion. 2.0 nm Al provided mediocre adhesion at best. Additionally there was a problem with deterioration of films. Initial appearance seemed to indicate that ethanol cleaning of the slides accelerated this deterioration. Due to the poor adhesion and film deterioration and the desire to move onto different material sets- tests and further depositions in this set were discontinued.

- *Corrosion tests of SiO(x) series*, Slides were coated with a saline solution (100 mM KCl, 10 mM Tris ph 7.5) in order to observe how the passivation layer would protect against corrosion. Solution was deposited by pipette onto the film surface and left alone and observed over a four hour period. Slides with oxygen percentages of 10%-

20% showed a whitish discolorization, but remained somewhat transparent for at least 2 hours before deteriorating. Slide with 5% oxygen deteriorated slowest and film remained intact for 4 hours. Slide with 0% oxygen deformed and broke.

- *Corrosion tests of thicker SiO(x) series*, The previous series of SiO(x) samples was repeated, but the thicknesses of the passivation layers were increased from 10 nm to 20 nm. The saline solution used on the previous samples was deposited by pipette onto the film surface and the interation of the solution and the films was observed over a four hour period. Slides with oxygen percentages of 10-20 % still showed a whitish discolorization, but the films remained transparent. The film did not deteriorate as fast as the previous run. The slide with 5 % oxygen slowly discolored and appeared to develop fine cracks in the film surface. The slide with 0 % oxygen did not discolor, however the film was deformed and the saline solution was able to seep under the film surface. The film ultimately ruptured and fragmented quicker than the previous sample. A silver film, without any passivation layer, was coated with the saline solution. The film surface discolored, ruptured and broke.

- *Series of Si/Ag/SiO(x)*, A series of samples replicating the SiO(x) samples used in the saline tests were made for future SPCE tests. The films are made with a 50nm Ag layer which is not mixed with any silicon. These slides are currently held under vacuum awaiting testing.

- *Resistivity tests*, A series of codepsited silver and silicon films were made for testing the range of resistivities across the film. During the preparation and deposition of this run series, problems with the RF power source became evident, flaking film buildup caused several shortages and loss of RF plasma. This series may be repeated to

ensure quality of film. These films have not been tested yet and have been held under vacuum awaiting testing. Since the resistivity measurements require a large, uniform surface, these stationary depositions will not be used for resistivity measurements.

- *AlSi series*, A nine slide series was initially planned for use in testing the apparatus. Only six complete slides were completed, troubles with the RF power supply impeded the deposition of a passivation layer on the final three slides. The slides were planned to have 50 nm of Ag, however, the retilting of the Ag source changed the Ag deposition rate and the samples actually have 34.1nm of Ag. These samples have not been tested yet and are held under vacuum awaiting testing.

Date	Run # (#slides)	Composition	Objectives	Conditions
6/14/05	05-095 (2)	Al (2nm)/Ag (50nm)/Al-N (5nm);15% N / on glass slides "pre-cleaned"	adhesion test, SPCE test	DC power 100W; 36.00 sccm; 1.2mTorr
6/14/05	05-096 (2)	Al (2nm)/Ag (50nm)/Al-N (10nm);15% N / on glass slides "pre-cleaned"	adhesion test, SPCE test	DC power 100W; 36.00 sccm; 1.2mTorr
6/14/05	05-097 (3)	Al (2nm)/Ag (50nm)/Al-N (20nm);15% N / on glass slides "pre-cleaned"	adhesion test, SPCE test	DC power 100W; 36.00 sccm; 1.2mTorr
6/14/05	05-098 (3)	Al (2nm)/Ag (50nm)/Al-N (40nm);15% N / on glass slides "pre-cleaned"	adhesion test, SPCE test	DC power 100W; 36.00 sccm; 1.2mTorr

Date	Run # (#slides)	Composition	Objectives	Conditions
6/15/05	05-099 (3)	Al (2nm)/Ag (50nm)/Al-N (60nm);15% N / on glass slides "pre-cleaned"	adhesion test, SPCE test	DC power 100W; 36.00 sccm; 1.2mTorr
6/15/05	05-100 (3)	Al (2nm)/Ag (50nm)/Al-N (80nm);15% N / on glass slides "pre-cleaned"	adhesion test, SPCE test	DC power 100W; 36.00 sccm; 1.2mTorr
6/15/05	05-101 (3)	Al (2nm)/Ag (50nm)/Al-N (100nm);15% N / on glass slides "pre-cleaned"	adhesion test, SPCE test	DC power 100W; 36.00 sccm; 1.2mTorr
6/15/05	05-102 (3)	Al (2nm)/Ag (50nm)/Al-N (120nm);15% N / on glass slides "pre-cleaned"	adhesion test, SPCE test	DC power 100W; 36.00 sccm; 1.2mTorr

Date	Run # (#slides)	Composition	Objectives	Conditions
6/16/05	05-103 (3)	Al (2nm)/Ag (50nm)/Al-N (140nm);15% N / on glass slides "pre-cleaned"	adhesion test, SPCE test	DC power 100W; 36.00 sccm; 1.2mTorr
6/16/05	05-104 (3)	Al (2nm)/Ag (50nm)/Al-N (160nm);15% N / on glass slides "pre-cleaned"	adhesion test, SPCE test	DC power 100W; 36.00 sccm; 1.2mTorr
6/20/05	05-105 (1)	AlSi (50nm) on glass slide- run at room temperature	adhesion test	DC power 100W; 32.00 sccm; 1.0 mTorr
6/20/05	05-106 (1)	AlSi (50nm) on glass slide- run heated to 200 deg. C	effect of heating on adhesion	DC power 100W; 32.00 sccm; 1.0 mTorr

Date	Run # (#slides)	Composition	Objectives	Conditions
6/23/05	05-109 (3)	AlSi (2nm)/Ag (50nm)/AlSi-N (0nm);15% N / on glass slides "pre-cleaned"	SPCE slides for UMD	DC power 100W (Ag layer), RF power 100W (AlSi, AlSi-N layer); 36.00 sccm; 1.2mTorr
6/24/05	05-110 (3)	AlSi (2nm)/Ag (50nm)/AlSi-N (5nm);15% N / on glass slides "pre-cleaned"	SPCE slides for UMD	DC power 100W (Ag layer), RF power 100W (AlSi, AlSi-N layer); 36.00 sccm; 1.2mTorr
6/24/05	05-111 (3)	AlSi (2nm)/Ag (50nm)/AlSi-N (10nm);15% N / on glass slides "pre-cleaned"	SPCE slides for UMD	DC power 100W (Ag layer), RF power 100W (AlSi, AlSi-N layer); 36.00 sccm; 1.2mTorr
6/24/05	05-112 (3)	AlSi (2nm)/Ag (50nm)/AlSi-N (20nm);15% N / on glass slides "pre-cleaned"	SPCE slides for UMD	DC power 100W (Ag layer), RF power 100W (AlSi, AlSi-N layer); 36.00 sccm; 1.2mTorr

Date	Run # (#slides)	Composition	Objectives	Conditions
6/24/05	05-113 (3)	AlSi (2nm)/Ag (50nm)/AlSi-N (40nm);15% N / on glass slides "pre-cleaned"	SPCE slides for UMD	DC power 100W (Ag layer), RF power 100W (AlSi, AlSi-N layer); 36.00 sccm; 1.2mTorr
6/24/05	05-114 (3)	AlSi (2nm)/Ag (50nm)/AlSi-N (60nm);15% N / on glass slides "pre-cleaned"	SPCE slides for UMD	DC power 100W (Ag layer), RF power 100W (AlSi, AlSi-N layer); 36.00 sccm; 1.2mTorr
6/24/05	05-115 (3)	AlSi (2nm)/Ag (50nm)/AlSi-N (80nm);15% N / on glass slides "pre-cleaned"	SPCE slides for UMD	DC power 100W (Ag layer), RF power 100W (AlSi, AlSi-N layer); 36.00 sccm; 1.2mTorr
6/27/05	05-116 (3)	AlSi (2nm)/Ag (50nm)/AlSi-N (80nm);15% N / on glass slides "pre-cleaned"	SPCE slides for UMD	DC power 100W (Ag layer), RF power 100W (AlSi, AlSi-N layer); 36.00 sccm; 1.2mTorr

Date	Run # (#slides)	Composition	Objectives	Conditions
6/27/05	05-117 (3)	AlSi (2nm)/Ag (50nm)/AlSi-N (100nm);15% N / on glass slides "pre-cleaned"	SPCE slides for UMD	DC power 100W (Ag layer), RF power 100W (AlSi, AlSi-N layer); 36.00 sccm; 1.2mTorr
6/28/05	05-118 (3)	AlSi (2nm)/Ag (50nm)/AlSi-N (120nm);15% N / on glass slides "pre-cleaned"	SPCE slides for UMD	DC power 100W (Ag layer), RF power 100W (AlSi, AlSi-N layer); 36.00 sccm; 1.2mTorr
6/28/05	05-119 (3)	AlSi (2nm)/Ag (50nm)/AlSi-N (140nm);15% N / on glass slides "pre-cleaned"	SPCE slides for UMD	DC power 100W (Ag layer), RF power 100W (AlSi, AlSi-N layer); 36.00 sccm; 1.2mTorr
6/29/05	05-120 (3)	AlSi (2nm)/Ag (50nm)/AlSi-N (5nm); 15% N / on glass slides "pre-cleaned"	SPCE slides for UNH	DC power 100W (Ag layer), RF power 100W (AlSi,AlSi-N layer); 36.00 sccm; 1.2 mTorr

Date	Run # (#slides)	Composition	Objectives	Conditions
6/29/05	05-121 (3)	AlSi (2nm)/Ag (50nm)/AlSi-N (5nm); 15% N / on glass slides "pre-cleaned"	SPCE slides for UNH	DC power 100W (Ag layer), RF power 100W (AlSi,AlSi-N layer); 36.00 sccm; 1.2 mTorr
6/29/05	05-122 (3)	AlSi (2nm)/Ag (50nm)/AlSi-N (5nm); 15% N / on glass slides "pre-cleaned"	SPCE slides for UNH	DC power 100W (Ag layer), RF power 100W (AlSi,AlSi-N layer); 36.00 sccm; 1.2 mTorr
11/1/05	05-206 (3)	AlSi (2nm)/Ag (50nm)/ AlSi-N (5nm); 15% N / on glass slides "pre-cleaned"	SPCE slides for UNH	DC power 100W (Ag layer), RF power 100W (AlSi, AlSi-N layer); 36.00 sccm; 1.2 mTorr
11/2/05	05-207 (3)	AlSi (2nm)/Ag (50nm)/ AlSi-N (5nm); 15% N / on glass slides cleaned with ethanol (200 proof)	SPCE slides for UNH	DC power 100W (Ag layer), RF power 100W (AlSi, AlSi-N layer); 36.00 sccm; 1.2 mTorr

Date	Run # (#slides)	Composition	Objectives	Conditions
11/2/05	05-208 (3)	AlSi (2nm)/Ag (50nm)/ AlSi-N (5nm); 15% N / on glass slides 2 "pre-cleaned", 1 cleaned with ethanol	SPCE slides for UNH	DC power 100W (Ag layer), RF power 100W (AlSi, AlSi-N layer); 36.00 sccm; 1.2 mTorr
11/5/05	05-211 (3)	AlSi (2nm)/Ag (50nm)/ AlSi-N (0nm);15% N / on ethanol cleaned glass slides	SPCE slides for UNH	DC power 100W (Ag layer), RF power 100W (AlSi layer); 36.00 sccm; 1.2 mTorr
11/5/05	05-212 (3)	AlSi (2nm)/Ag (50nm)/ AlSi-N (10nm);15% N / on ethanol cleaned glass slides	SPCE slides for UNH	DC power 100W (Ag layer), RF power 100W (AlSi layer); 36.00 sccm; 1.2 mTorr ****Loss of plasma during AlSi-N layer****
11/5/05	05-213 (3)	AlSi (2nm)/Ag (50nm)/ AlSi-N (10nm);15% N / on ethanol cleaned glass slides	SPCE slides for UNH	DC power 100W (Ag layer), RF power 100W (AlSi layer); 36.00 sccm; 1.2 mTorr ****Run not rotated****

Date	Run # (#slides)	Composition	Objectives	Conditions
11/5/05	05-214 (3)	AlSi (2nm)/Ag (50nm)/ AlSi-N (10nm);15% N / on ethanol cleaned glass slides	SPCE slides for UNH	DC power 100W (Ag layer), RF power 100W (AlSi layer); 36.00 sccm; 1.2 mTorr
11/6/05	05-215 (3)	AlSi (2nm)/Ag (50nm)/ AlSi-N (20nm);15% N / on ethanol cleaned glass slides	SPCE slides for UNH	DC power 100W (Ag layer), RF power 100W (AlSi layer); 36.00 sccm; 1.2 mTorr ****Loss of plasma during AlSi-N layer****
11/6/05	05-216 (3)	AlSi (2nm)/Ag (50nm)/ AlSi-N (20nm);15% N / on ethanol cleaned glass slides	SPCE slides for UNH	DC power 100W (Ag layer), RF power 100W (AlSi layer); 36.00 sccm; 1.2 mTorr ****Loss of plasma during AlSi-N layer****
11/9/05	05-219 (3)	AlSi (2nm)/ Ag (50nm)/ AlSi-N (10nm); 15% N / on ethanol cleaned glass slides	SPCE slides for UNH	DC power 100W (Ag layer), RF power 100W (AlSi, AlSi-N layer); 36.00 sccm; 1.2 mTorr ****Loss of plasma during AlSi-N layer****

Date	Run # (#slides)	Composition	Objectives	Conditions
11/16/05	05-220 (1)	AlSi (2nm)/ Ag (100nm) / on ethanol cleaned glass slides	control film for SPCE	DC power 100W (Ag layer), RF power 100W (AlSi layer); 36.00 sccm; 1.2 mTorr
5/18/06	06-067 (1)	Si (2nm)/ Ag (50nm) on "pre-cleaned" slide	adhesion test	DC power 100W (Ag layer), RF power 110W (Si layer); 36.00 sccm; 1.6 mTorr
5/31/06	06-069 (1)	Si (1.5nm)/ Ag (50nm) on "pre-cleaned" slide	adhesion test	DC power 100W (Ag layer), RF power 115W (Si layer); 36.00 sccm; 1.6 mTorr
6/2/06	06-070 (1)	Si (1.0nm)/ Ag (50nm) on "pre-cleaned" slide	adhesion test	DC power 100W (Ag layer), RF power 115W (Si layer); 36.00 sccm; 1.6 mTorr

Date	Run # (#slides)	Composition	Objectives	Conditions
6/5/06	06-071 (1)	Si (2nm)/ Ag (50nm) on "pre-cleaned" slide + 10 minute presputter of Si target	adhesion test	DC power 100W (Ag layer), RF power 115W (Si layer); 36.4 sccm; 1.6 mTorr
6/5/06	06-072 (1)	Si (2.0nm)/ Ag (50nm) on ethanol cleaned slide	adhesion test	DC power 100W (Ag layer), RF power 115W (Si layer); 36.4 sccm; 1.6 mTorr
6/6/06	06-074 (1)	Si (1.0nm)/ Ag (50nm) on ethanol cleaned slide + 10 minute presputter of Si target	adhesion test	DC power 100W (Ag layer), RF power 115W (Si layer); 36.00 sccm; 1.5 mTorr
6/6/06	06-075 (1)	Si (0.5nm)/ Ag (50nm) on ethanol cleaned slide + 10 minute presputter of Si target	adhesion test	DC power 100W (Ag layer), RF power 115W (Si layer); 36.00 sccm; 1.6 mTorr

Date	Run # (#slides)	Composition	Objectives	Conditions
6/6/06	06-076 (1)	Si (0.75nm)/ Ag (50nm) on ethanol cleaned slide + 10 minute presputter of Si target	adhesion test	DC power 100W (Ag layer), RF power 115W (Si layer); 36.00 sccm; 1.5 mTorr
6/8/06	06-078 (1)	Si (1.0nm)/ Ag (50nm) on ethanol cleaned slide + 20 minute presputter of Si target	adhesion test/reproducibility of 06-070	DC power 100W (Ag layer), RF power 115W (Si layer); 36.00 sccm; 1.5 mTorr
6/8/06	06-079 (1)	Si (1.0nm)/ Ag (50nm)/ Si-N (10nm); 25% N / on ethanol cleaned slide + 5 minute presputter of Si target	SPCE film	DC power 100W (Ag layer), RF power 115W (Si, Si-N layer); 36.00 sccm; 1.5 mTorr
6/8/06	06-080 (1)	Si (1.0nm)/ Ag (50nm)/ Si-N (7.5nm); 25% N / on ethanol cleaned slide + 5 minute presputter of Si target	SPCE film	DC power 100W (Ag layer), RF power 115W (Si, Si-N layer); 36.00 sccm; 1.5 mTorr

Date	Run # (#slides)	Composition	Objectives	Conditions
6/8/06	06-081 (1)	Si (1.0nm)/ Ag (50nm)/ Si-N (5.0nm); 25% N / on ethanol cleaned slide + 5 minute presputter of Si target	SPCE film	DC power 100W (Ag layer), RF power 115W (Si, Si-N layer); 36.00 sccm; 1.5 mTorr
6/8/06	06-082 (1)	Si (1.0nm)/ Ag (50nm)/ Si-N (2.5nm); 25% N / on ethanol cleaned slide + 5 minute presputter of Si target	SPCE film	DC power 100W (Ag layer), RF power 115W (Si, Si-N layer); 36.00 sccm; 1.5 mTorr
6/13/06	06-083 (1)	Si (1.0nm)/ Ag (50nm)/ Si-N (2.5nm); 25% N / on ethanol cleaned slide + 5 minute presputter of Si target	SPCE film	DC power 100W (Ag layer), RF power 115W (Si, Si-N layer); 36.00 sccm; 1.5 mTorr
6/13/06	06-084 (1)	Si (1.0nm)/ Ag (50nm)/ Si-N (2.0nm); 25% N / on ethanol cleaned slide + 5 minute presputter of Si target	SPCE film	DC power 100W (Ag layer), RF power 115W (Si, Si-N layer); 36.00 sccm; 1.5 mTorr

Date	Run # (#slides)	Composition	Objectives	Conditions
6/13/06	06-085 (1)	Si (1.0nm)/ Ag (50nm)/ Si-N (1.5nm); 25% N / on ethanol cleaned slide + 5 minute presputter of Si target	SPCE film	DC power 100W (Ag layer), RF power 115W (Si, Si-N layer); 36.00 sccm; 1.5 mTorr
6/13/06	06-086 (1)	Si (1.0nm)/ Ag (50nm)/ Si-N (1.0nm); 25% N / on ethanol cleaned slide + 5 minute presputter of Si target	SPCE film	DC power 100W (Ag layer), RF power 115W (Si, Si-N layer); 36.00 sccm; 1.5 mTorr
6/26/06	06-091 (3)	Si(1.0nm)/ Ag(50nm)/ Si-N (1.0nm); 25% N / on ethanol cleaned slides + 5 minute presputter of Si target	SPCE film	DC power 100W (Ag layer), RF power 115W (Si, Si-N layer); 36.00 sccm; 1.5 mTorr
6/26/06	06-092 (3)	Si(1.0nm)/ Ag(50nm)/ Si-N (2.0nm); 25% N / on ethanol cleaned slides + 5 minute presputter of Si target	SPCE film	DC power 100W (Ag layer), RF power 115W (Si, Si-N layer); 36.00 sccm; 1.5 mTorr

Date	Run # (#slides)	Composition	Objectives	Conditions
6/26/06	06-093 (3)	Si(1.0nm)/ Ag(50nm)/ Si-N (3.0nm); 25% N / on ethanol cleaned slides + 5 minute presputter of Si target	SPCE film	DC power 100W (Ag layer), RF power 115W (Si, Si-N layer); 36.00 sccm; 1.5 mTorr
7/6/06	06-102 (3)	Si(1.0nm)/ Ag(50nm)/ Si (2nm) / on ethanol cleaned slides + 5 minute presputter of Si target	SPCE films	DC power 100W (Ag layer), RF power 115W (Si, Si-N layer); 36.00 sccm; 1.5 mTorr
7/6/06	06-103 (3)	Si(1.0nm)/ Ag(50nm)/ Si-N (2nm); 5% N / on ethanol cleaned slides + 5 minute presputter of Si target	SPCE films	DC power 100W (Ag layer), RF power 115W (Si, Si-N layer); 36.00 sccm; 1.5 mTorr
7/6/06	06-104 (3)	Si(1.0nm)/ Ag(50nm)/ Si-N (2nm); 10% N / on ethanol cleaned slides + 5 minute presputter of Si target	SPCE films	DC power 100W (Ag layer), RF power 115W (Si, Si-N layer); 36.00 sccm; 1.5 mTorr

Date	Run # (#slides)	Composition	Objectives	Conditions
7/6/06	06-105 (3)	Si(1.0nm)/ Ag(50nm)/ Si-N (2nm); 15% N / on ethanol cleaned slides + 5 minute presputter of Si target	SPCE films	DC power 100W (Ag layer), RF power 115W (Si, Si-N layer); 36.00 sccm; 1.5 mTorr
7/6/06	06-106 (3)	Si(1.0nm)/ Ag(50nm)/ Si-N (2nm); 20% N / on ethanol cleaned slides + 5 minute presputter of Si target	SPCE films	DC power 100W (Ag layer), RF power 115W (Si, Si-N layer); 36.00 sccm; 1.5 mTorr
7/6/06	06-107 (3)	Si(1.0nm)/ Ag(50nm)/ Si-N (2nm); 25% N / on ethanol cleaned slides + 5 minute presputter of Si target	SPCE films	DC power 100W (Ag layer), RF power 115W (Si, Si-N layer); 36.00 sccm; 1.5 mTorr
8/2/06	06-134 (1)	Al(0.5nm)/ Ag(50nm) / on ethanol cleaned slides	adhesion test	DC power 100W; 36.00 sccm; 1.5 mTorr

Date	Run # (#slides)	Composition	Objectives	Conditions
8/2/06	06-135 (1)	Al(0.5nm)/ Ag(50nm) / on ethanol cleaned slides	adhesion test	DC power 100W; 36.00 sccm; 1.5 mTorr
8/2/00	06-136 (1)	Al(1.0nm)/ Ag(50nm) / on ethanol cleaned slides	adhesion test	DC power 100W; 36.00 sccm; 1.5 mTorr
8/2/06	06-137 (1)	Al(2.0nm)/ Ag(50nm) / on ethanol cleaned slides	adhesion test	DC power 100W; 36.00 sccm; 1.5 mTorr
9/18/06	06-159 (1)	Si(1.0nm)/ Ag(50nm)/ SiO(x)(10nm); 20% Oxygen/ on ethanol cleaned slides	SPCE film	DC 100W (Ag layer), RF power 125W (Si, SiO(x) layer; 36.00 sccm; 1.4mTorr

Date	Run # (#slides)	Composition	Objectives	Conditions
9/19/06	06-160 (1)	Si(1.0nm)/ Ag(50nm)/ SiO(x)(10nm); 10% Oxygen/ on ethanol cleaned slides	SPCE film	DC 100W (Ag layer), RF power 125W (Si, SiO(x) layer; 36.00 sccm; 1.4mTorr
9/26/06	06-162 (1)	Si(1nm)/ Ag(50nm)/ SiO(x)(10nm); 15% Oxygen/ on ethanol cleaned slides	SPCE film	DC 100W (Ag layer), RF power 125W (Si, SiO(x) layer; 36.00 sccm; 1.4mTorr
9/26/06	06-163 (1)	Si(1.0nm)/ Ag(50nm)/ SiO(x)(10nm); 5% Oxygen/ on ethanol cleaned slides	SPCE film	DC 100W (Ag layer), RF power 125W Si, SiO(x) layer; 36.00 sccm; 1.4mTorr
9/26/06	06-164 (1)	Si(1.0nm)/ Ag(50nm)/ SiO(x)(10nm); 0% Oxygen/ on ethanol cleaned slides	SPCE film	DC 100W (Ag layer), RF power 125W (Si, SiO(x) layer; 36.00 sccm; 1.4mTorr

Date	Run # (#slides)	Composition	Objectives	Conditions
9/28/06	06-165 (1)	Si(1nm)/ Ag(50nm)/ SiO(x)(20nm); 20% Oxygen/ ethanol cleaned slides	SPCE film	DC 100W (Ag layer), RF power 125W Si, SiO(x) layer; 36.00 sccm; 1.4mTorr
9/28/06	06-166 (1)	Si(1nm)/ Ag(50nm)/ SiO(x)(20nm); 15% Oxygen/ ethanol cleaned slides	SPCE film	DC 100W (Ag layer), RF power 125W Si, SiO(x) layer; 36.00 sccm; 1.4mTorr
9/28/06	06-167 (1)	Si(1nm)/ Ag(50nm)/ SiO(x)(20nm); 10% Oxygen/ ethanol cleaned slides	SPCE film	DC 100W (Ag layer), RF power 125W Si, SiO(x) layer; 36.00 sccm; 1.4mTorr
9/28/06	06-168 (1)	Si(1nm)/ Ag(50nm)/ SiO(x)(20nm); 5% Oxygen/ ethanol cleaned slides	SPCE film	DC 100W (Ag layer), RF power 125W Si, SiO(x) layer; 36.00 sccm; 1.4mTorr

Date	Run # (#slides)	Composition	Objectives	Conditions
9/28/06	06-169 (1)	Si(1nm)/ Ag(50nm)/ SiO(x)(20nm); 0% Oxygen/ ethanol cleaned slides	SPCE film	DC 100W (Ag layer), RF power 125W Si, SiO(x) layer; 36.00 sccm; 1.4mTorr
9/28/06	06-170 (1)	Si(1nm)/Ag(50nm); ethanol cleaned slide	control for saline tests	DC 100W (Ag layer), RF power 125W Si; 36.00 sccm; 1.4mTorr
9/29/06	06-171 (3)	Si(1nm)/ Ag(50nm)/ SiO(x)(10nm); 5% Oxygen/ ethanol cleaned slides	SPCE film	DC 100W (Ag layer), RF power 125W Si, SiO(x) layer; 36.00 sccm; 1.4mTorr
9/29/06	06-172(3)	Si(1nm)/ Ag(50nm)/ SiO(x)(20nm); 5% Oxygen/ ethanol cleaned slides	SPCE film	DC 100W (Ag layer), RF power 125W Si, SiO(x) layer; 36.00 sccm; 1.4mTorr

Date	Run # (#slides)	Composition	Objectives	Conditions
9/29/06	06-173 (2)	Si(1nm)/ Ag(50nm)/ SiO(x)(20nm); 15% Oxygen/ ethanol cleaned slides	SPCE film	DC 100W (Ag layer), RF power 125W Si, SiO(x) layer; 36.00 sccm; 1.4mTorr
9/29/06	06-174 (2)	Si(1nm)/ Ag(50nm)/ SiO(x)(20nm); 10% Oxygen/ ethanol cleaned slides	SPCE film	DC 100W (Ag layer), RF power 125W Si, SiO(x) layer; 36.00 sccm; 1.3mTorr
11/16/06	06-193 (1)	90% Ag-10% Si stationary codeposition (50nm)/ ethanol cleaned slides	resistivity tests	DC 52W (Ag) RF power 150W Si; 36.00 sccm; 1.5mTorr
11/16/06	06-194 (1)	80% Ag-20% Si stationary codeposition (50nm)/ ethanol cleaned slides	resistivity tests	DC 12W (Ag) RF power 150W Si; 36.00 sccm; 1.5mTorr

Date	Run # (#slides)	Composition	Objectives	Conditions
11/16/06	06-195 (1)	80% Ag-20% Si stationary codeposition (50nm)/ ethanol cleaned slides	resistivity tests	DC 21W (Ag) RF power 150W Si; 36.00 sccm; 1.5mTorr
11/16/06	06-196 (1)	70% Ag-30% Si stationary codeposition (50nm)/ ethanol cleaned slides	resistivity tests	DC 12W (Ag) RF power 150W Si; 36.00 sccm; 1.5mTorr
12/2/06	06-204 (3)	AlSi(2nm)/ Ag(50nm)/ AlSi-N(5nm); 15%N; on ethanol cleaned slides; +5 min. presputter of AlSi target	SPCE films to test apparatus	DC 100W (Ag layer); RF 100W (AlSi, AlSi-N layer); 36.00 sccm; 1.5mTorr
12/2/06	06-205 (3)	AlSi(2nm)/ Ag(50nm)/ AlSi-N(5nm); 15%N; on ethanol cleaned slides; +5 min. presputter of AlSi target	SPCE films to test apparatus	DC 100W (Ag layer); RF 100W (AlSi, AlSi-N layer); 36.00 sccm; 1.5mTorr

Date	Run # (#slides)	Composition	Objectives	Conditions
12/2/06	06-206 (3)	AlSi(2nm)/Ag(50nm); on ethanol cleaned slides	SPCE films to test apparatus	DC 100W (Ag layer); RF 100W (AlSi layer); 36.00 sccm; 1.5mTorr